

POLITECNICO DI TORINO

Corso di Laurea Magistrale
in Ingegneria per l'Ambiente e il Territorio

Tesi di Laurea Magistrale

*A photogrammetry application to rockfall monitoring: the Belca, Slovenia
case study*



Relatore

Andrea M. Lingua (*Politecnico di Torino*)

Co-relatore

Grigillo Dejan (*University of Ljubljana*)

Candidato

Alessandro La Rocca, s244424

Anno Accademico 2019/2020

Abstract

UAV photogrammetry offers a powerful and cheap methodology to reconstruct the terrain geomorphology. The purpose of this study is the application of a generic Structure-from-Motion workflow to properly elaborate different set of images from multitemporal surveys in order to perform a surface and volume change detection by meaning of a cloud-to-cloud comparison. The complex geomorphology of the site of interest, characterized by niches, asperities, flat rock walls with different orientation, debris deposits and isolated rock blocks, challenges the accurate reprojection of the image points into a 3D space. The chronological comparison of the point cloud offers a qualitative and quantitative estimation of distances and volume change between sequential models. For the cloud-to-cloud distance computation, a level of accuracy accounting for different sources of uncertainty was estimated.

Seven data sets were available for this study and they were acquired by two different faculties of the University of Ljubljana, Biotechnical Faculty and Faculty of Civil and Geodetic Engineering. Many surveys were performed with different approaches, leading to different accuracy in the final reconstruction of the terrain. The data post-processing has been performed with the latest versions of Agisoft Metashape and CloudCompare software.

Contents

Abstract	a
Figures Index.....	c
Tables Index	d
1. Introduction	1
1.1. Disciplines of remote sensing	1
1.2. Photogrammetry	2
1.2.1. History	2
1.2.2. Applications	3
1.2.3. Principles and fundamentals.....	5
1.2.4. Structure from Motion.....	9
2. Site description.....	12
3. Data Acquisition.....	14
4. Data processing	18
4.1. Import and alignment of the images.....	19
4.2. Input of GCP coordinates.....	21
4.3. Cleaning the sparse point cloud by gradual selection	23
4.4. Optimization of the georeferencing.....	29
4.5. Building of dense point cloud	34
4.6. Classification.....	36
5. Point Cloud Comparison	40
5.1. Noise filtering.....	40
5.2. Registration	41
5.3. Estimation of cloud-to-cloud distance.....	42
5.3.1. Description of M3C2 algorithm	44
5.3.2. Definition of confidence interval	45
5.3.3. Definition of the normal orientation and the optimal normal scale.....	46
5.3.4. Definition of the optimal projection scale	48
5.3.5. Results of M3C2 distance estimation	50
5.4. Calculation of volume changes	59
6. Results and discussion.....	62
7. Conclusion.....	66
Reference List	68
APPENDIX A	71
APPENDIX B	72
APPENDIX C	76

Figures Index

Figure 1-1-1 - First picture in history (1826); the exposure of the plate lasted 8 hours. (Figure from Boccardo [7])	1
Figure 1-2 - Analogue stereo-plotter. (Figure from Gis Resources [13]).....	2
Figure 1-3 - Evolution of photogrammetry thanks to the inventions of 20th century. (Figure from Shenk [28])	3
Figure 1-4 – Schematic illustration of a geocentric coordinate system (red) and a topocentric coordinate system (blue). (Figure from http://help.digi21.net/SistemasDeReferenciaDeCoordenadasTopocentricos.html)	6
Figure 2-1 – Geolocation of the site of interest.	12
Figure 3-1 – Targets used in the surveys	15
Figure 3-2 – Instruments for the topographic survey of October 24 th (D7): (a) prism target on a tripod, (b) detail of the prism target, (c) total station on a tripod.	16
Figure 4-1 Example of image-matching of feature points: the blue lines stand for a valid matching, the purple one stand for an invalid matching.....	19
Figure 4-2 - Camera location and overlap of the images	21
Figure 4-3 – Spatial distribution of the GCP adopted in the the georeferencing process and the error in meters along the easting (x), northing (y) and altitude (z) direction is shown for every marker; in case of the data from FGG (D2, D3, D4, D5, D7) the shown errors refer to a level of accuracy set by the user.	31
Figure 4-4 – Distribution of the difference between the reprojection error of each marker considered as GCP and then as CP.	33
Figure 4-5 - Spatial distribution of the GCPs and CPs adopted for checking the accuracy of the generated model; the error in meters along the easting (x), northing (y) and altitude (z) direction is shown for every marker.	36
Figure 4-6 – Schematic difference between the Digital Surface Model (DSM) and the Digital Terrain Model (DTM). (Figure from Meza et al. [21])	36
Figure 4-7 – Difference between the DSM and the DTM in an urban area. (Figure from https://3dmetrica.it/dtm-dsm-dem/).....	37
Figure 4-8 – Main steps of the Cloth Simulation filter. (Figure from Zhang et al. [36]).....	38
Figure 5-1 – Comparison of the result before (a) and after (b) using the SOR filter;	41
Figure 5-2 – Scheme of the principle of how C2C works. (Figure from CloudCompare user manual [6])	43
Figure 5-3 – Scheme of the main steps of the M3C2 algorithm. (Figure from Lague et al. [17])	44
Figure 5-4 – Scheme of a complex topography and consequences of different normal scales in distance computation. (Figure from Lague et al. [17]).....	46
Figure 5-5 – Explanatory comparison between the normals computation with different scales: (a) D=0,5 m, (b) D=1 m, (c) D=5 m; the point cloud comes from D7 data set.....	47
Figure 5-6 - Explanatory comparison between the normals computed by the M3C2 algorithm, according to the preferred orientation +Z (a), and the ones computed by the CloudCompare tool and oriented with the Minimum Spanning method (b), given a normal scale D=1 m.	47

Figure 5-7 – Relationship between LOD95% and d in different kind of terrain. (Figure from Lague et al [17])	48
Figure 5-8 – Explanatory visual comparison between significant change detection according different values of projection scale: (a) d=0,5 m, (b) d=1 m, (c) d=2 m.	49
Figure 5-9 – LiDAR data from Slovenian geodatabase acquired in 2004; spatial resolution of 1 m.	50
Figure 5-10 – Comparison of D1 with LiDAR data: (a) significant change, (b) distance uncertainty and (c) estimated distance.....	51
Figure 5-11 - Comparison of D2 with D1 data: (a) significant change, (b) distance uncertainty and (c) estimated distance.....	52
Figure 5-12 - Comparison of D2 with LiDAR data: (a) significant change, (b) distance uncertainty and (c) estimated distance.....	53
Figure 5-13 - Comparison of D3 with D2 data: (a) significant change, (b) distance uncertainty and (c) estimated distance.....	54
Figure 5-14 - Comparison of D4 with D3 data: (a) significant change, (b) distance uncertainty and (c) estimated distance.....	55
Figure 5-15 - Comparison of D5 with D4 data: (a) significant change, (b) distance uncertainty and (c) estimated distance.....	56
Figure 5-16 - Comparison of D6 with D5 data: (a) significant change, (b) distance uncertainty and (c) estimated distance.....	57
Figure 5-17 - Comparison of D7 with D6 data: (a) significant change, (b) distance uncertainty and (c) estimated distance.....	58
Figure 5-18 – Scheme of the principle behind the methodology adopted to estimate volume changes starting from M3C2 distances. (Figure from Griffith et al. [14])	60
Figure 6-1 – Horizontal, vertical and total RMS reprojection error averaged over all the GCPs.	63

Tables Index

Table 3-1 – Short description of the data	15
Table 4-1 – System configuration.	18
Table 4-2 – Parameters adopted to clean the sparse point cloud for each data set.....	25
Table 4-3 – Values of reprojection error, RMS and maximum values, both in terms of tie point scale and pixel and values of mean key point size in pixels.....	28
Table 5-1 – Cumulative results for volume change estimation from each comparison.	61

1. Introduction

1.1. Disciplines of remote sensing

The knowledge of the territory and the environment, as discussed by Boccardo [6], has always been a matter of interest for many reasons: food, water, natural resources, weather, defense, safety and more.



Figure 1-1-1 - First picture in history (1826); the exposure of the plate lasted 8 hours. (Figure from Boccardo [7])

Thanks to the technical improvements in the past centuries, our ability to capture the information that we need from what surrounds us has got better and better. More specifically, a turning point has been the invention of photography in the first decades of XIX century that allowed us to capture light and for the first time to collect the information about what reality looks like. Since then the progresses made in aerospace technologies, electronics and optics led to the possibility to get images of the Earth from high above and to observe difference frequencies of the light, in order to reveal many hidden information that were absent in the visible spectrum.

These discoveries allowed us to experience a new way to observe the world: finally, we were able to investigate those phenomena that were inapproachable before and now they can be used to establish the symptoms of those events that we weren't able to comprehend.

In the years many different but strictly correlated to each other disciplines were born:

- **Geodesy** that studies the shape of the Earth considering the spatial distribution of the gravity field; its accuracy increased when Global Positioning System (GPS) technologies were adopted thanks to the presence of satellites around the globe.
- **Topography** that studies the methods and the instruments that allow the precise metric measurements of points of a surface (ground, urban areas, historical monuments, etc.) and its graphic representation. It allows an accurate estimation of distances, areas and volume in many application fields.
- **Cartography** that studies the difficult task to represent a 3D surface into a 2D plane thanks the application of mathematics and projective geometry, since it must be

considered the shape of the Earth according to geodesy. For this reason, informatics brought a huge development introducing Geographic Information Systems (GIS) that allows an easier way to produce metric and thematic charts. Today it's possible to visualize many information about the territory with a good accuracy: population density, geology, hydrology, slope inclination and many more.

- **Remote sensing** that studies the acquisition, elaboration and interpretation of spatial data from satellites and airplane in order to produce a thematic map of the territory. The main characteristics of this discipline is the ability to acquire multispectral and multitemporal images: the possibility to capture a different range of wavelength of the electro-magnetic field allows us to automatically emphasize one or more features of interest, and the possibility to observe the same area in different times give us the chance to observe the chronological evolution of that particular feature.
- **Photogrammetry** that studies the technology of obtaining of reliable information about the environment or even objects, as building and monuments, through the process of recording, measuring and interpreting photographic images. Its largest application is to extract both topographic and planimetric information from aerial images in order to obtain an accurate Digital Surface Model (DSM) or Digital Terrain Model (DTM).

1.2. Photogrammetry

1.2.1. History

Cannarozzo et al. [8], together with Shenk [28], offer an historical background. The invention of photogrammetry can be the first procedure that was suggested to be performed on photograms: in 1851 Aimè Lussedat proposed a method to obtain a measurement from two images, but ignoring the camera's distortion effect on the images led to great errors. Later, in order to resolve such a problem, the Italian Ignazio Porro invented the photogoniometer that was able to measure the direction angles of the projection lines going from the perspective center to the points of the captured object.

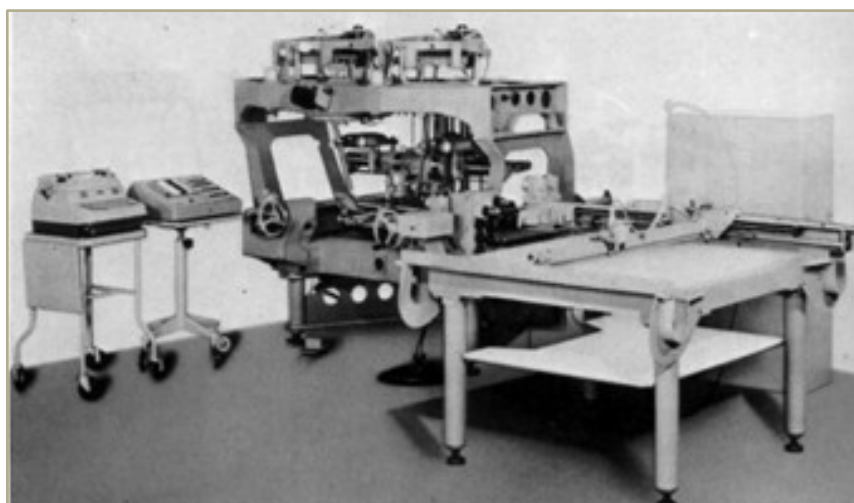


Figure 1-2 - Analogue stereo-plotter. (Figure from Gis Resources [13])

In the early years of the 20th century, C. Pulfrich introduced the concept of stereoscopy and E. Von Orel applied this by inventing the first stereo-autograph in 1909: two photographs were overlapped through this analogue plotter in order to get a three-dimensional geometry of the terrain and obtain a topographic map of an area.

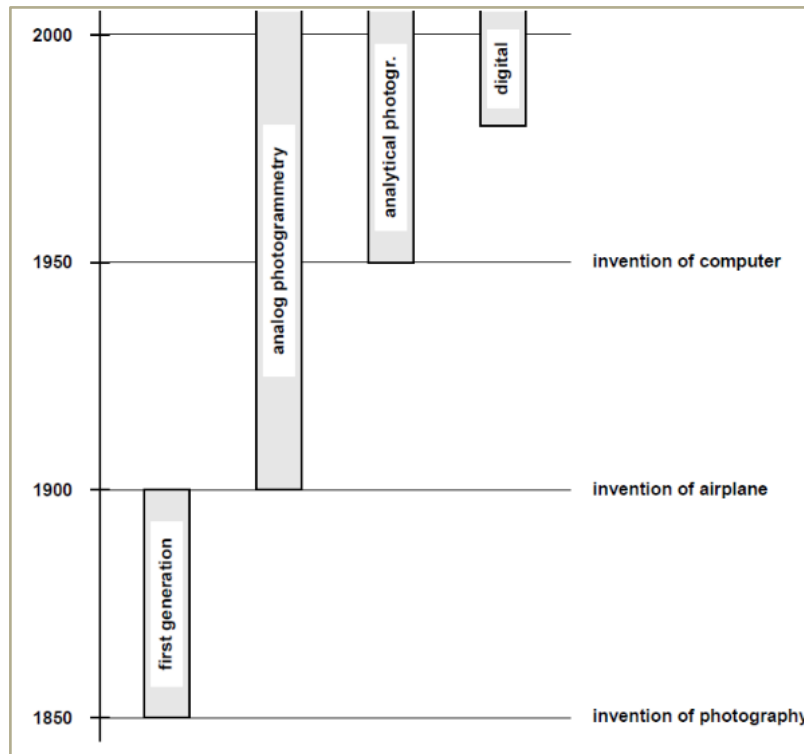


Figure 1-3 - Evolution of photogrammetry thanks to the inventions of 20th century. (Figure from Shenk [28])

Thanks to the computer sciences in the 60s the big and expansive optical and mechanical plotters were replaced by analytical triangulation, analytical plotters and orthophoto projectors, introducing the possibility to generate digital models as the DEM (Digital Elevation Model). This only happened in the 80s due to a temporal gap from the research and the practical use in photogrammetry, going through development of the first model and their diffusion.

Analytical photogrammetry has been later replaced by digital photogrammetry. Digital images, obtained by scanning photographs or by digital cameras, were analyzed by sophisticated software and most of the process has been automated so to minimize the manual photogrammetric operations of the operator. The final products of this procedure were digital maps, DEMs and digital orthoimages that were easily saved in computer media storage and ready to be integrated with a GIS software.

1.2.2. Applications

Photogrammetry is a discipline that finds its application in many fields of study, accordingly to the object observed by meaning of several photographs taken from different points of view. We can find:

- **Industrial photogrammetry:** the object is usually an artificial element, which scale can differ from the little component of a vehicle to a long pipeline. It offers a rapid and

automated procedure to perform accurate 3D measurements in order to obtain a quality control on the final product, monitor real-time changes and observe the deterioration of many materials; in fact, it has been applied as a useful substitute of traditional Coordinates Measuring Machines, as articulated arms or laser trackers.

- **Architectural photogrammetry:** the object can be one or more buildings and they are investigated by close-range photogrammetry with the purpose to monitor the cultural and historical heritage. In the investigation of vast and urbanized areas by meaning of photogrammetry it is possible to easily guarantee a 3D model useful for consideration as: emergency plans, energy request, infrastructure design and land register. A large use is adopted in survey archeological areas to monitor surface deterioration or historical reconstruction.
- **Biostereometric:** a model of the human body, especially a part of it, is reconstructed in order to detect any geometric changes as a consequence of its natural growth or after surgery. Despite its medical application, such models can be used as biodynamic models for vehicle crash victims in computer simulation or dummy design.
- **Space photogrammetry:** the object can be an extraterrestrial element, as a planet or a satellite, or can be a terrestrial element, as the clouds.
- **Aerial photogrammetry:** the object is the earth's surface and the reconstructed scene may contain both natural and urbanized areas. Its application goes from the natural hazard estimation to photomaps creation.

The application of photogrammetry, given the same object and same methodology, can also depends on the purpose of the investigation. The 3D virtual reconstruction of any object or surface can be used also in the production of Computed Generated Images (CGI) adopted in movies and games realization or eventually it can be used in police investigation in order to reconstruct a crime scene starting from the available footage or several photographs of the scene.

In this thesis, the main focus is on the application of aerial photogrammetry in the study of natural geomorphology. Thanks to significant developments in the last years, photogrammetry (together with laser scanning) revealed to be a valid tool in building digital terrain models (DTMs) without any contact with the object and an accuracy close to traditional survey methods; this led to its application in detecting, classifying and monitoring different kind of ground instability: erosion, landslide, rockfall, debris flow, etc. Both terrestrial and aerial photogrammetry allow to easily produce 3D models of the same portion of terrain in different times, guaranteeing by the meaning of DTMs comparison to realize multi temporal studies. Thanks also to research studies concerning classification algorithms, it's becoming easier and easier to automatically perform the classification of vegetation, building, cars, etc. from point clouds, obtained by Structure from Motion (SfM) photogrammetry.

By meaning to UAV photogrammetry, today is possible monitoring fluvial morphodynamics, observing landslide and glacier evolution, detecting erosion and deposit areas, characterizing the discontinuities in a rock mass, realizing geology maps and estimating vegetation extension with advantages if compared to other methods, as LiDAR or Aerial

Laser Scanner (ALS), in terms of portability, cost, power consumption and time of execution.

1.2.3. Principles and fundamentals

The main purpose of photogrammetry is to rebuild the geometry of an object. In order to do so, it's necessary to establish a geometric relationship between the image space and the object/ground space: for each of one, a coordinate system must be defined.

The image coordinate system is defined by three perpendicular axes (x, y, z) with the center as the intersection between the lines that join the fiducial marks on the sensor. The x -axis and y -axis are collinear to those lines, as shown in *Figure 1-4a*. The z -axis is the optical axis, the line perpendicular to the sensor and going through both the perspective center O of the lens and the principal point P of the sensor. In analytical photogrammetry the coordinate system is usually rigidly translated so that the origin is equal the perspective center O (*Figure 1-4b*). Theoretically, the center of the image should be equal to P but, due to errors in the construction of the camera, there is an offset of hundredth of millimeters. The ground coordinate system is as three axes reference system (X, Y, Z) that utilizes a known geographic map projection. It could be a geocentric or a topocentric coordinate system (Gis Resources [13]): in the first case the origin is set at the center of the Earth ellipsoide, the X -axis passes through the Greenwich meridian, the Z -axis is equal to the rotation axis of the

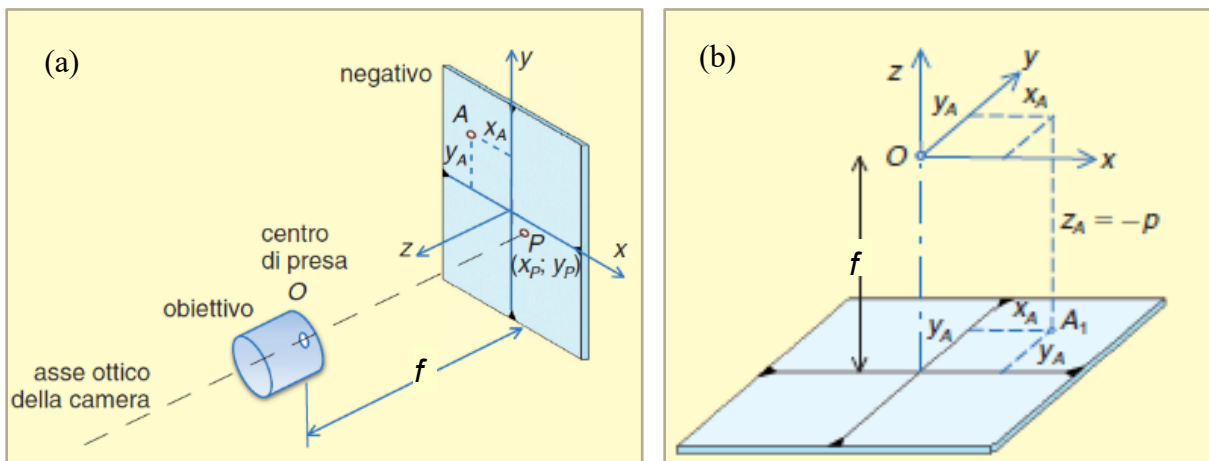


Figure 1-4– (a) Image coordinate system of the negative; in case of the positive, the direction of the z -axis should be the opposite. (b) Image coordinates system used in analytical photogrammetry. (Figures from Cannarozzo et al. [8])

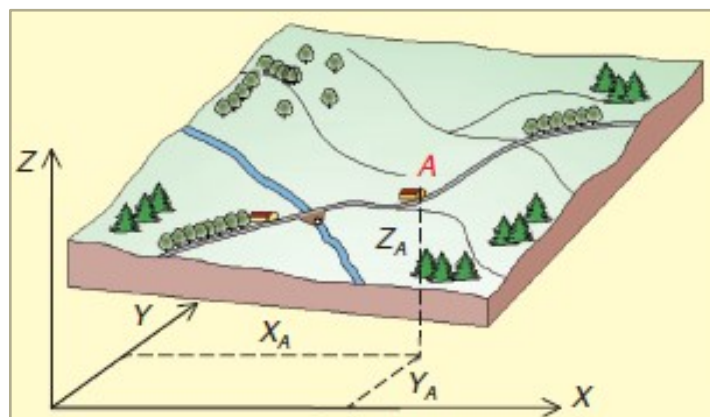


Figure 1-5 – Ground coordinate system. (Figure from Cannarozzo et al. [8])

planet, and the Y-axis is perpendicular to both the X-axis and the Z-axis; instead, in the second case the origin is set on the surface of Earth ellipsoide, both X-axis and Y-axis belong to the tangential plane that goes through the origin, respectively oriented eastward and northward, while the Z-axis is vertical to the reference plane.

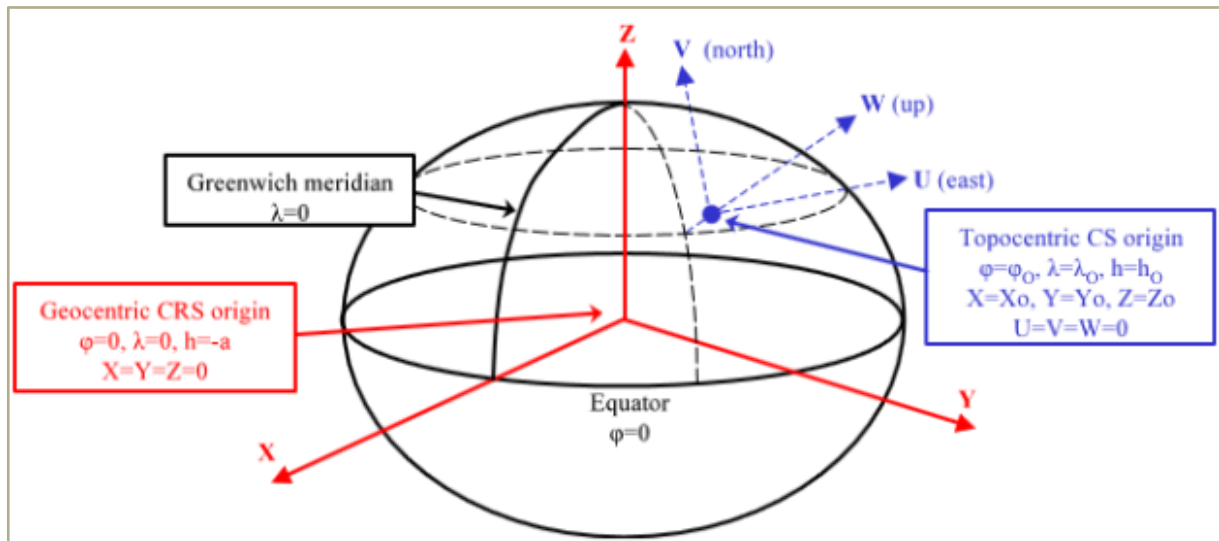


Figure 1-4 – Schematic illustration of a geocentric coordinate system (red) and a topocentric coordinate system (blue). (Figure from <http://help.digi21.net/SistemasDeReferenciaDeCoordenadasTopocentricos.html>)

The main steps of a photogrammetric survey are:

- I. **Data acquisition**
- II. **Orientation**
- III. **Restitution**

The proper reconstruction of a scene or an object requires multiple images taken from different points of view; these pictures also need to overlap in order to allow the detection of a series of homologous points.

The first condition is necessary since the object space is three dimensional, thus there isn't a unique correspondence between a point in the image space A' and a point in the object space A : many other points are aligned to the projection line $A-A'$. In order to establish the right position of the point A it is necessary at least another picture that represents the object: by

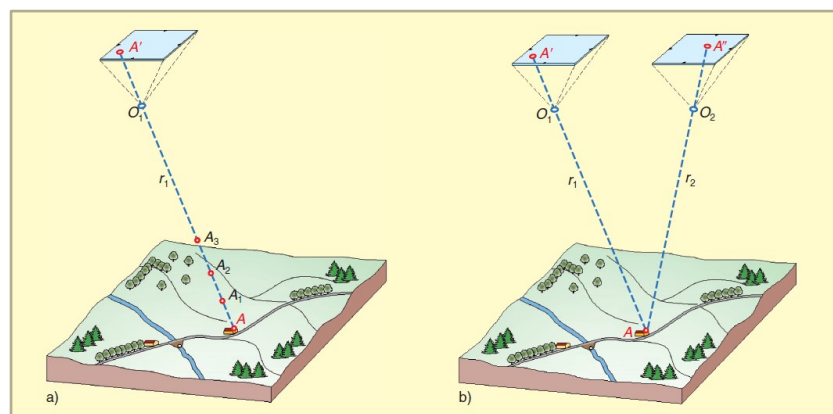


Figure 1-6 – Scheme of aerial image acquisition: two images are necessary to define the exact position of one point in the object space. (Figure from Cannarozzo et al. [8])

this way it is possible to obtain the position of A thanks to the intersection of the two projection lines A-A' and A-A''.

This is possible when the second condition is verified: two sequent photographs must contain the same portion of the scene. Especially in aerial photogrammetric surveys, this happens when the flight path and altitude (*Figure 1-7*) and the time interval between two photographs are properly studied accordingly to the investigation area extension. As a generic rule, the longitudinal overlapping of two images taken flying in the same direction is about 60%, but it can reach 75% in case of complex terrains; the lateral overlapping instead is about 10-20%.

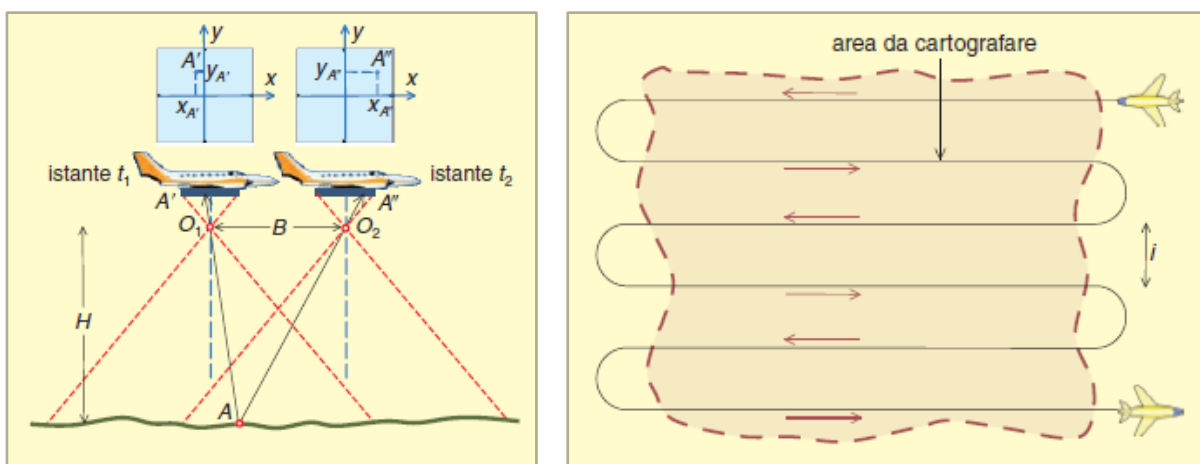


Figure 1-7 – Scheme of aerial data acquisition: the flight path and altitude must guarantee an overlap between the images accordingly with the terrain complexity and extension. (Figures from Cannarozzo et al. [8])

After taking all the required photographs, the internal geometry of the camera and its position and orientation in the space at the moment of data acquisition must be defined. This process is called respectively interior and exterior orientation. In the first case, the principal point P and principal distance p or focal length f are defined. Since the camera optical system made of lens is not perfect, the image on the sensor is actually different from the scene: the incoming projection line is not exactly parallel to the outgoing one, so in some portion of the image a distortion occurs. Such deformation is not homogenous all over the sensor but it spreads along some directions accordingly with the distance from the optical system of lens.

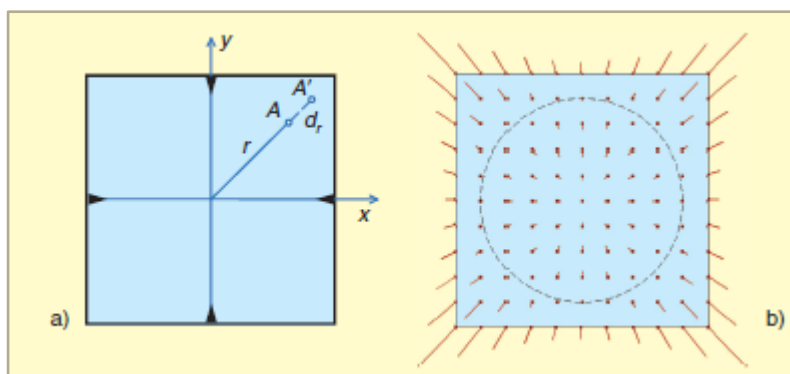


Figure 1-8 – (a) Radial and tangential components of the distortion; (b) distribution of the radial distortion on the sensor. (Figure from Cannarozzo et al. [8])

The deformation can be also divided into two components, radial and tangential (*Figure 1-8a*); since the first one is usually the 95% of the total deformation, in some cases is the only one displayed on the sensor during the calibration process (*Figure 1-8b*).

The exterior orientation, instead, consists of estimating the position of the perspective center in the ground space coordinate system for each photograph (X_{O_i} , Y_{O_i} , Z_{O_i}) and the rotation between the image and space coordinate system (ω along the x-axis, φ along the y-axis and κ along the z-axis). A schematic illustration is shown in *Figure 1-9a*.

All these parameters are used to solve the collinearity equation, that defines the relationship between the sensor, the image coordinates and the ground coordinates and it's necessary to obtain the final restitution.

The formula suggested by Gis Resources [13] is

$$\mathbf{a} = k \cdot \mathbf{MA} \quad (1.1)$$

where:

- \mathbf{a} is the vector going from the perspective point O to an image point A_i (*Figure 1-9b*) and defined accordingly the principle point coordinates and the focal length:

$$\mathbf{a} = \begin{bmatrix} x_p - x_o \\ y_p - y_o \\ -f \end{bmatrix} \quad (1.2)$$

- \mathbf{A} is the vector going from the perspective center O to a ground point A (*Figure 1-9b*), formulated as follows:

$$\mathbf{A} = \begin{bmatrix} X_p - X_o \\ Y_p - Y_o \\ Z_p - Z_o \end{bmatrix} \quad (1.3)$$

- M is the rotation matrix that allows to express both vectors in the same coordinate system;
- k is a scalar multiple.

The meaning of this equation is that the image point, the perspective center and the ground point are collinear; they belong to the same projection line that goes through the perspective point.

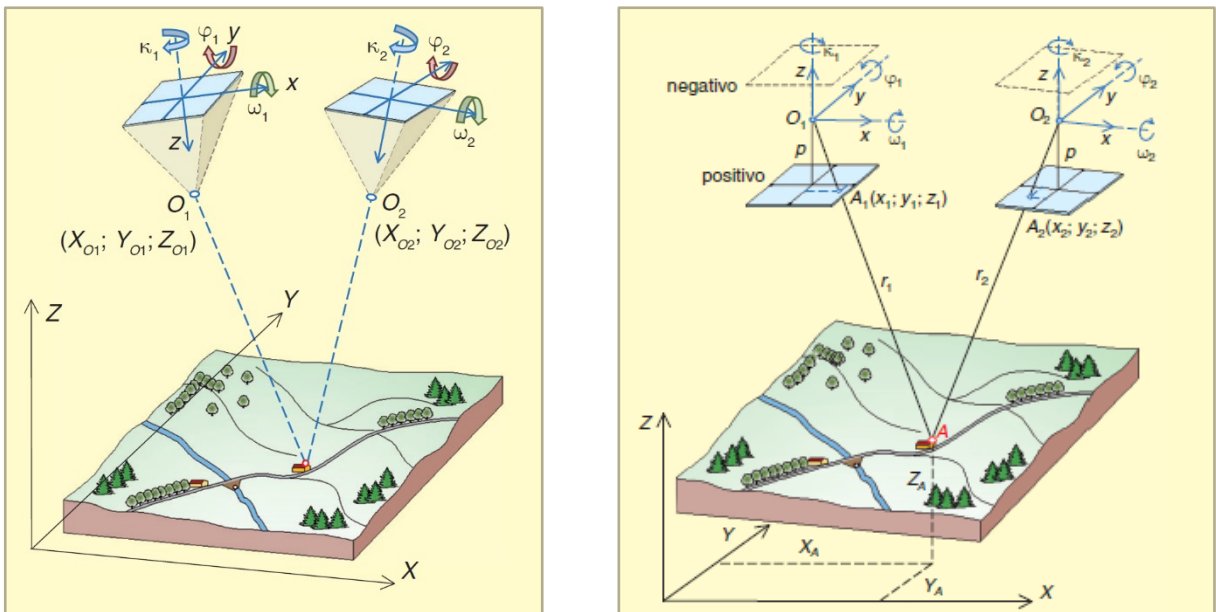


Figure 1-9 – (a) Schematic illustration of the parameters estimated during orientation; (b) schematic illustration of the parameters involved into the collinearity equation. (Figures from Cannarozzo et al. [8])

1.2.4. Structure from Motion

Structure from Motion (SfM), first used in 1990s in computer vision community and in the development of automatic feature-matching algorithm, is a photogrammetric method which allows a topography reconstruction with a high level of detail (Westoby et al [33]).

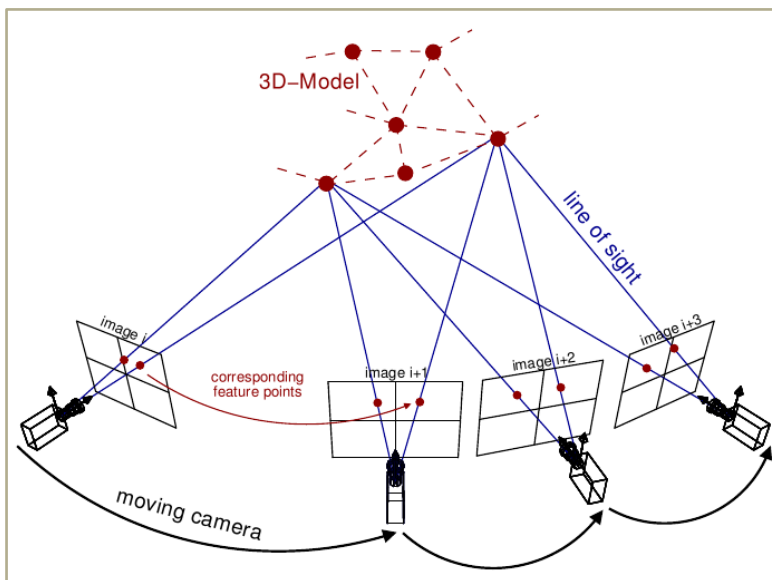


Figure 1-10 – Schematic illustration of the main concept behind Structure from Motion methodology. (Figure from Nissen [24])

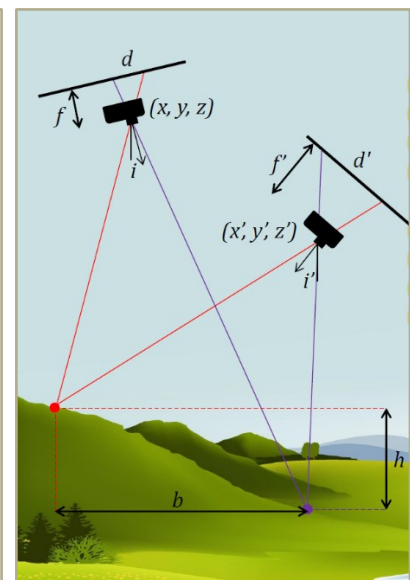


Figure 1-11 – Scheme of the parameters computed by performing the bundle adjustment. (Figure from Nissen [24])

Differently from traditional photogrammetric processes, SfM reconstructs a scene starting from a set of multiple overlapping images of the same scene or object, taken from different angles, without requiring the 3D location of a series of multiple control points to be known. This approach uses algorithm such as SIFT (Scale Invariant Feature Transform) that identifies automatically the common features between a subset of images: this, especially, allows to support large changes in camera perspective and large variations in image scale. The detected points are then projected into a 3D space and the relative position of images is defined thanks to a bundle block adjustment: this is an iterative and highly redundant process that establish the position of two feature points by meaning of an automatic calculation of internal camera geometry (f) and external camera position (x, y, z) and rotation (i). The final result is a sparse point cloud which represents the structure of the scene/object obtain by the motion of a camera. Control points and check points can also be used, but they are not necessary to reconstruct the model. They allow to adjust the scale and the orientation of the point cloud in a defined geographic coordinate system and to verify the final quality of the reconstruction.

Figure 1-12 shows the main difference between aerial and terrestrial LiDAR methodology and the aerial SfM photogrammetry approach. LiDAR involves more expensive instruments and it requires a more accurate planning of the survey. The 3D location of a series of control points inside the scene must be known (this is also required in SfM photogrammetry when used for geodetic purposes) and the sensor position and orientation must be accurately defined by the operator. Thus, rapid and repeated investigations are difficult to perform. However, LiDAR allows to filter the vegetation into the scene and to acquire a good ground model of the investigated area. SfM photogrammetry, even if it is able to register the color of each point together with the geometry of the scene, giving a texture to the final model, is not able to automatically ignore the vegetation, so non-ground points must be classified and removed in order to eventually obtain a DTM.

At the end, the advantage – mainly in technical application rather than in scientific work- of Structure from Motion is that it gives a black-box tool to perform a high resolution topographic reconstruction where expert supervision is strictly limited, if not unnecessary (Micheletti et al. [22]). However, this may lead to a series of errors not easy to identify since the operator has less involvement in the quality control of data acquisition.

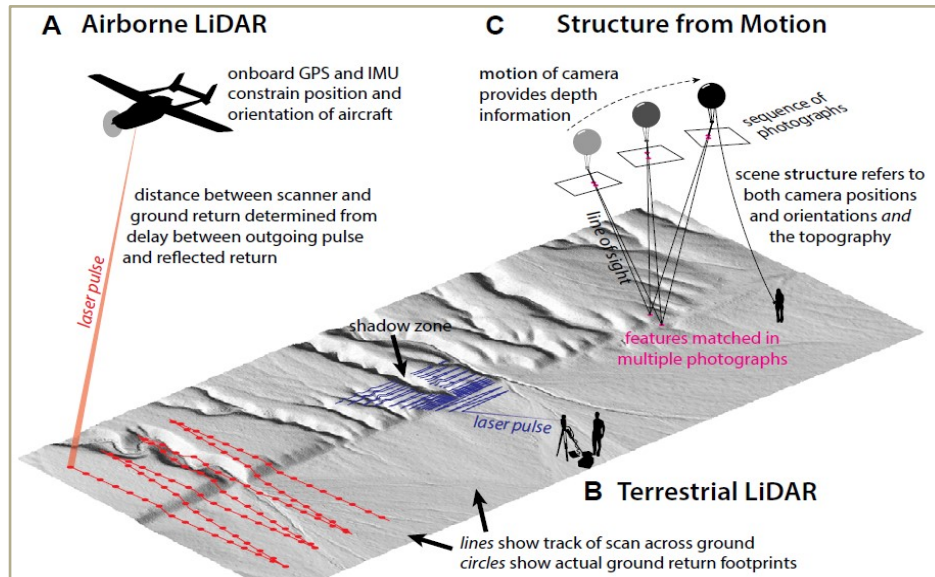


Figure 1-12 – Schematic illustration of the SfM procedure to obtain high resolution topographic models, together with other two methods, Airborne LiDAR and terrestrial LiDAR. (Figure from Johnson et al. [16])

2. Site description

The area of this study is in the North-West region of Slovenia, in Central Europe. It is located near the village of Belca in the municipality of Kranjska Gora, close to the Austrian border, about 60 km from Ljubljana, the capital city.

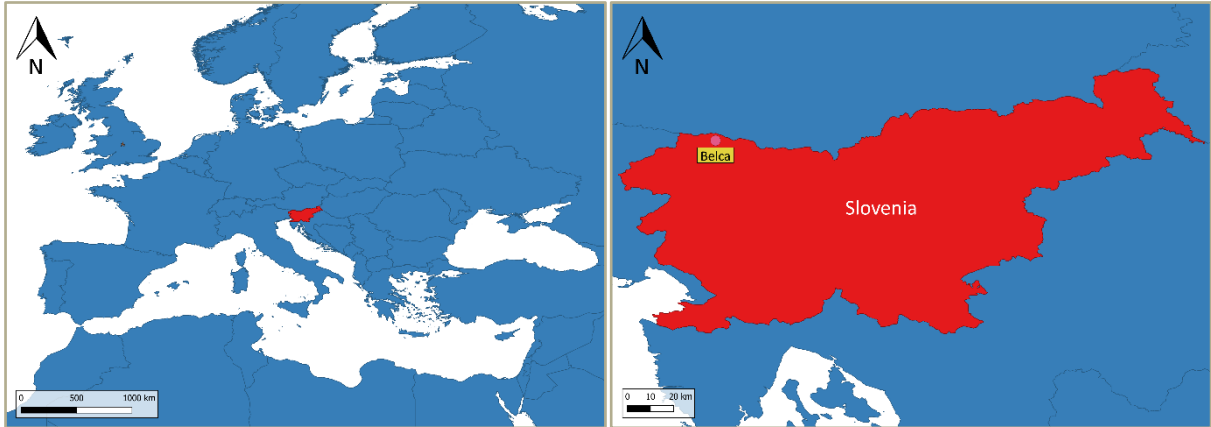


Figure 2-1 – Geolocation of the site of interest.

The site is mainly characterized by a fractured rock mass on the slope of a mountain, at the bottom of which the fallen debris has deposited (*Figure 2-2a*). The valley is short and narrow and it is crossed by a small torrent (*Figure 2-2b*) which flows into the Sava main river. Most of the bigger blocks accumulated in the years are on the upper portion of the torrent (*Figure 2-2c*).

From a geological point of view, the slope is made of Upper Triassic rocks, mainly light grey massive dolomite and layers of limestone, strongly tectonized.

The slope has been monitored because a rock fall with a volume of 5000-10000 m³ occurred in September 2014. In the period from 2014 to 2017, both geotechnical and geological data were acquired by Lazar et al. [18]: in particular wire extensometers, tachometry, TLS and ALS were adopted.



Figure 2-2 – Photographs of the site, taken during the last survey (October 24th 2019): (a) the slope characterized by the fractured rock mass and debris deposit, (b) the torrent along the valley and (c) the blocks accumulated over the upper portion of the torrent.

3. Data Acquisition

The data for this study comes from seven different surveys, five of which were performed by members of University Ljubljana, Faculty of Civil and Geodetic Engineering (*Fakulteta za gradbeništvo in geodezijo, FGG*) and the remaining two were performed by the Department of Forestry and Renewable Forest Resources of the Biotechnical Faculty (*Biotehniška Fakulteta, BF*). They go from July 2018 to October 2019.

The observed area changed in the first surveys: at first only the upper part was captured, then the entire riverbed has been once observed in order to detect the eventual transportation of the detached material and progressively only the portion of the river closer to the slope was sometimes considered in the survey.



Figure 3-1 – DJI Mavic Air. (Figure from <https://www.drone-store.it/prodotto/dji-mavic-air-bianco/>)



Figure 3-2 – DJI Phantom 4. (Figure from <https://www.amazon.it/DJI-PHANTOM-PRO-OBSIDIAN-Risoluzione/dp/B075FVB86M>)

The data from BF were acquired with a DJI Mavic Air drone with a FC2103 camera model, having a focal length of 4.5 mm and returning images with a resolution of 4056x3040 pixels. No description of the surveys is given. Apparently, the flights weren't performed systematically but by manual piloting of the drone.

The data from FGG were acquired with a DJI Phantom 4 with a FC6310 camera model, having a focal length of 8.8 mm and images with a resolution of 5472x3648 pixels.

The flight plans changed from a survey to another, learning from previous experiences (look at *Table 3-1*). At first only one flight for both the slope and the river was planned. Due to the complex geomorphology of the slope, 3 flights were planned with an oblique orientation of the camera (45°): the first two (*fake* and *flat1*) were performed at the same height, one having as reference a previous DTM of the area and the other one having as reference a plane with an inclination close to the overall slope; the third flight (*flat 2*) was performed as the second one but with a greater flying altitude in order to guarantee a greater overlap of the images. Then, the presence of isolated blocks and niches led to consider a different point view, so a flight with the camera orientated to the vertical direction was introduced. The portion of the river not close to the slope was no more considered and only one flight with an oblique camera was necessary to reduce the number of holes in the final model.

	Date	Performed by	Flight's Tag	Number of images	Orientation	Flying altitude (m)	Ground resolution (cm/pix)	Coverage area (km ²)	Number of targets
D1	08-11-18	BF		110	/	122	3,69		10
D2	03-07-18	FGG	Slope	212	Oblique	63,6	1,6	0,0694	7
			Riverbed	133	Vertical	76,1	1,91	0,132	11
D3	04-12-18	FGG	Fake	159	Oblique	61,6	1,53	0,0524	15
			Flat 1	159	Oblique	62,9	1,6	0,0564	
			Flat 2	159	Oblique	67,6	1,84	0,0186	
			Riverbed	60	Vertical	81,2	2,24	0,00794	3
D4	11-12-18	FGG	Vertical	218	Vertical	92,6	2,53	0,0383	18
			Flat	246	Oblique	70,5	1,93	0,0305	
			Fake	194	Oblique	68	1,86	0,0296	
D5	12-04-19	FGG	Vertical	219	Vertical	90,2	2,46	0,0398	9
			Fake	166	Oblique	67,4	1,84	0,0258	
D6	18-10-19	BF		694	/	86,6	2,93	0,107	20
D7	24-10-19	FGG	Vertical	186	Vertical	96,2	2,62	0,04	8
			Fake	149	Oblique	90	2,46	0,0268	

Table 3-1 – Short description of the data

In order to perform the georeferencing of the final model, the actual position of some control points was measured.

Different kinds of targets for signaling the ground control points have been used in the surveys. The BF adopted mainly chess-like black and white aerial targets (a), the only exception was for a marker in their second survey (D6) for which a cross was painted (d) on a rock. The FGG instead adopted two kinds of target: black circle on white frame (b) for those points on a horizontal plane and a yellow circle (c) for those points on a vertical plane (usually a rock wall or a tree). Also in this case, a green cross was painted on a block as a target.

The actual measurements of the position of the targets were performed according to different geodetic methods.

The methodology adopted by BF is unknown, but the coordinates available come with a level of accuracy between 1,5 and 4 cm both in horizontal and vertical direction.

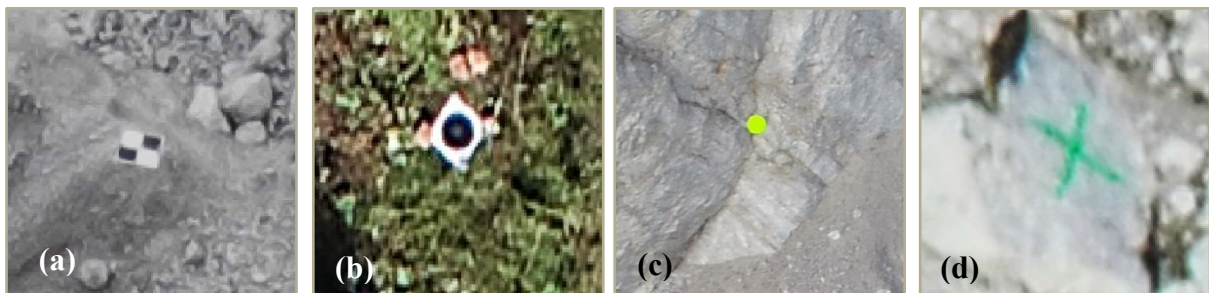


Figure 3-1 – Targets used in the surveys

The FGG adopted at first the methodology of RTK (Real-Time Kinematics) GNSS (Global navigation Satellite System) with an achieved accuracy of 0.04/0.08: due to problems with the GNSS signal some measurements came with a great error, so this method revealed to be not the optimum one. Later a combination of tacheometry and GNSS, with an accuracy in a rank of 2-3 cm, was adopted. Some of the instruments adopted in the survey of October 24th (D7) can be seen in *Figures 3-4 (a)-(c)*.

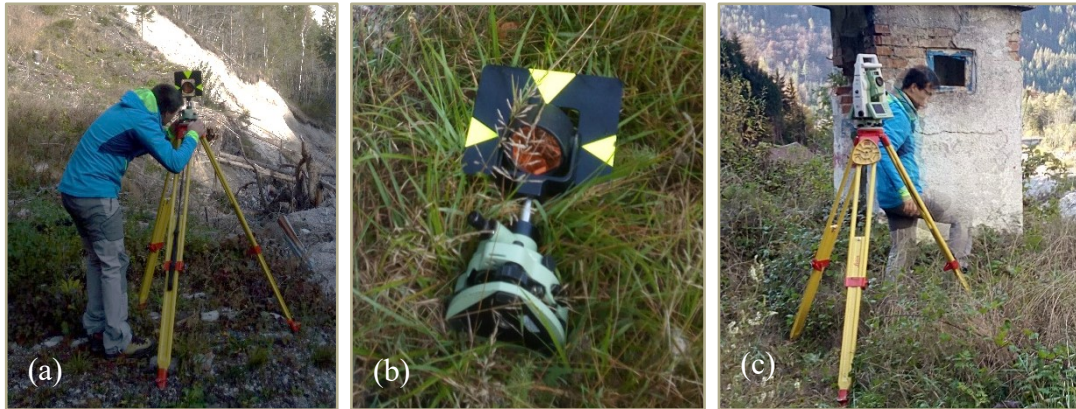
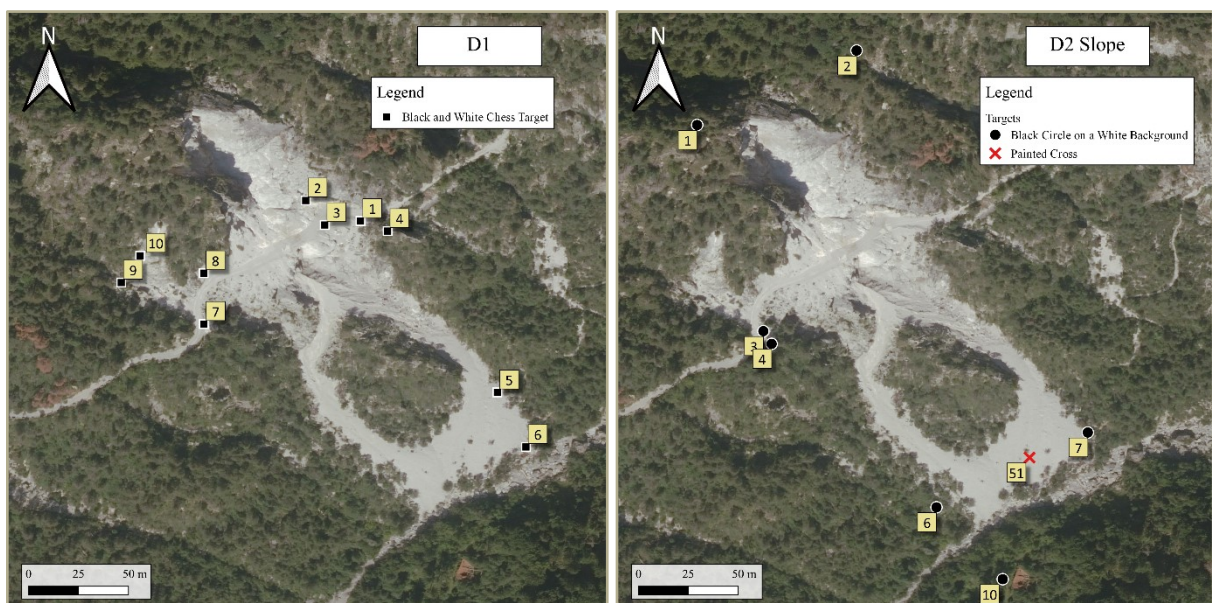


Figure 3-2 – Instruments for the topographic survey of October 24th (D7): (a) prism target on a tripod, (b) detail of the prism target, (c) total station on a tripod.

The number and the distribution of the target changed between the surveys. The main limit is instability of the slope and its accessibility. Some targets were placed out of the body of the rockslide: at the top, at the bottom, and some on the sides of the main body, thanks to the presence of a road that used to go through the slope before being covered by the debris flow.

Every target used for each survey is shown in the following figures (*Figures 3-6*). Not all of them were used as GCP (Ground Control Points) or CP (Check Point) because sometimes the difference between the estimated position and the input coordinates was too big (probably due to some errors in the acquisition of the spatial datum) or the number of projections (how many times the target appears into the images) were lower than 2.



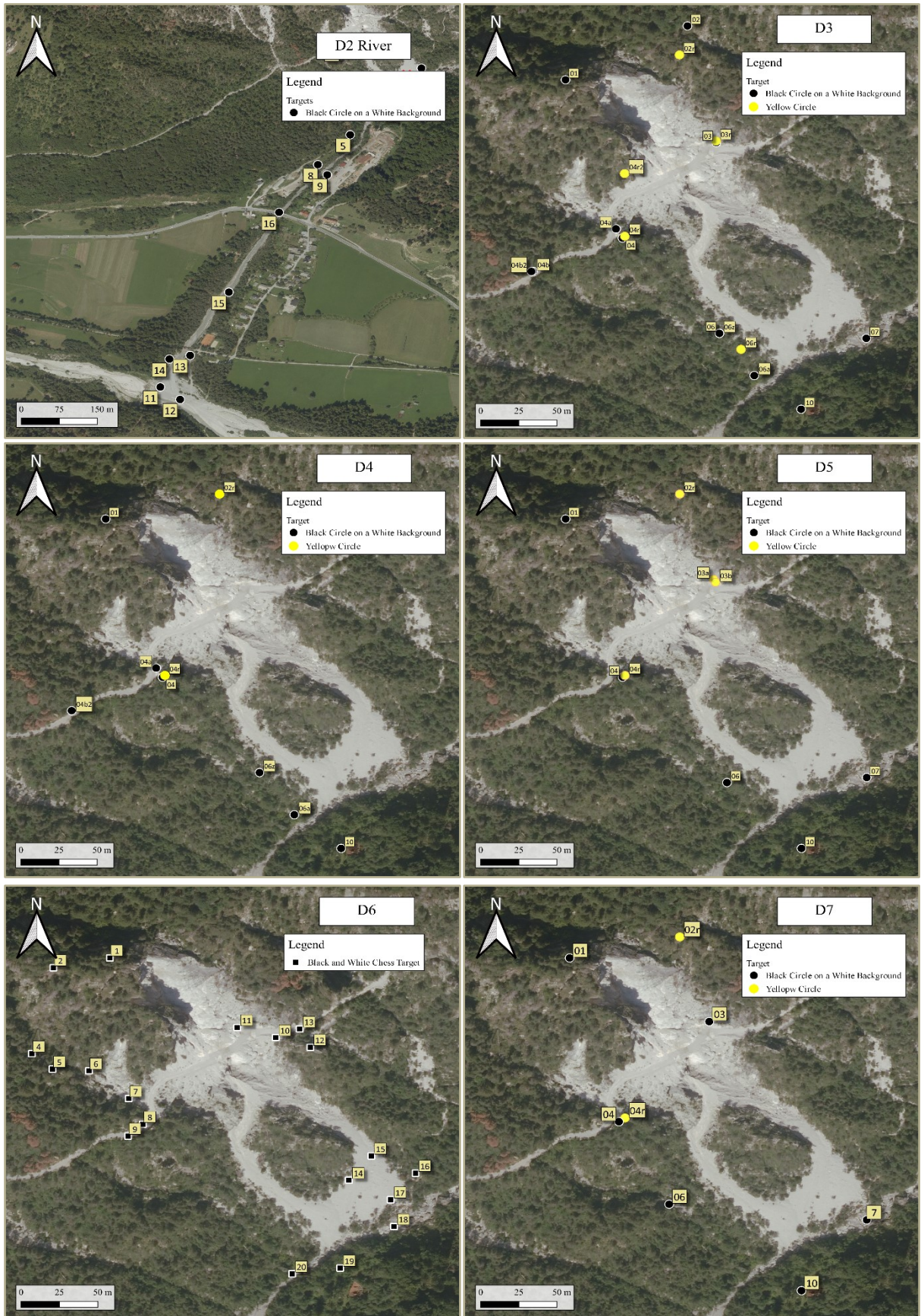


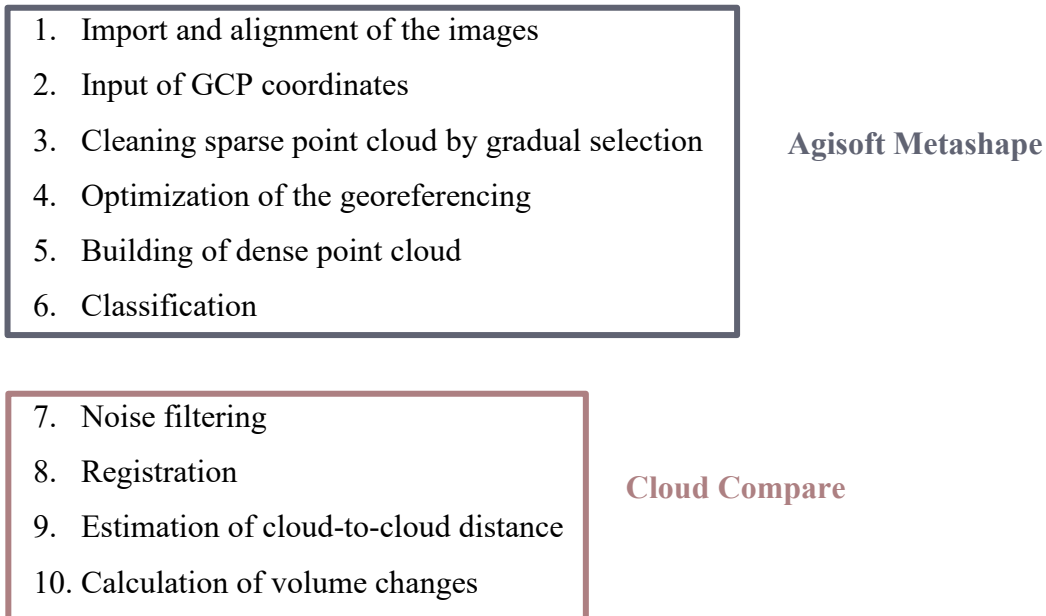
Figure 3-5 – Targets adopted during the photogrammetric surveys.

4. Data processing

Photogrammetry is a discipline that allow to build a 3D model of an object or the terrain starting from the acquisition of many images from different points of view. A valid reconstruction of a geometry, in terms of dimension and shape, depends on the accurate estimation of the interior and exterior orientation of the cameras: they define the actual inside geometry of the camera and its position and rotation for every photo taken.

In order to perform such procedure, the software Agisoft Metashape Pro (version 1.5) has been used. It uses a Structure from Motion (SfM) that allows the matching of the features of many images in order to reconstruct the camera motion and the geometry of a 3D scene. This process, after some elaborations, lead to a georeferenced dense point cloud that can later be imported into the software CloudCompare (version 2.6.1) for multi-temporal change detection by meaning of point cloud comparison.

The general workflow adopted follows these steps:



These procedures were carried out with the following system configuration (*Table 4-1*).

Processor	Intel® Core™ i7-9700 CPU @ 3.00GHz 3.00GHz
RAM	64 GB
System type	64-bit Operating System, x64-based processor
Graphic Card	NVIDIA GeForce GTX 1660

Table 4-1 – System configuration.

4.1. Import and alignment of the images

The first step was to load the photos into the software. In case of multiple flights in a single survey, multiple sets of photos were available: these were loaded in different chunks in order to have one single project for every flight.

In order to obtain a first three-dimensional reconstruction of the area, the photos must be aligned. The software looks for characteristic points in every image, the so-called Key Points, and tries to match them in order to define the Tie Points. A limit for both key points and ties points, can be defined by the operator according to his necessities: in this case the default parameters was adopted (respectively 4'000 and 30'000).

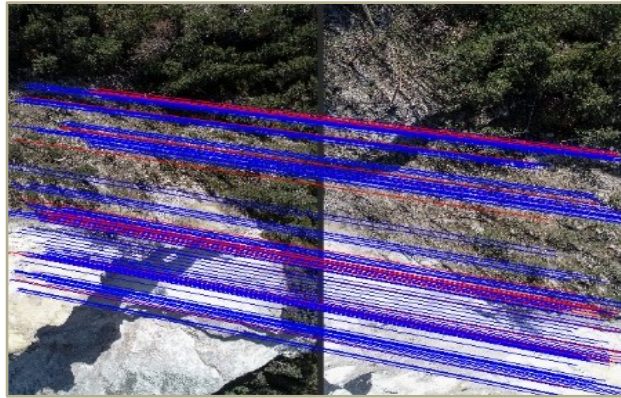
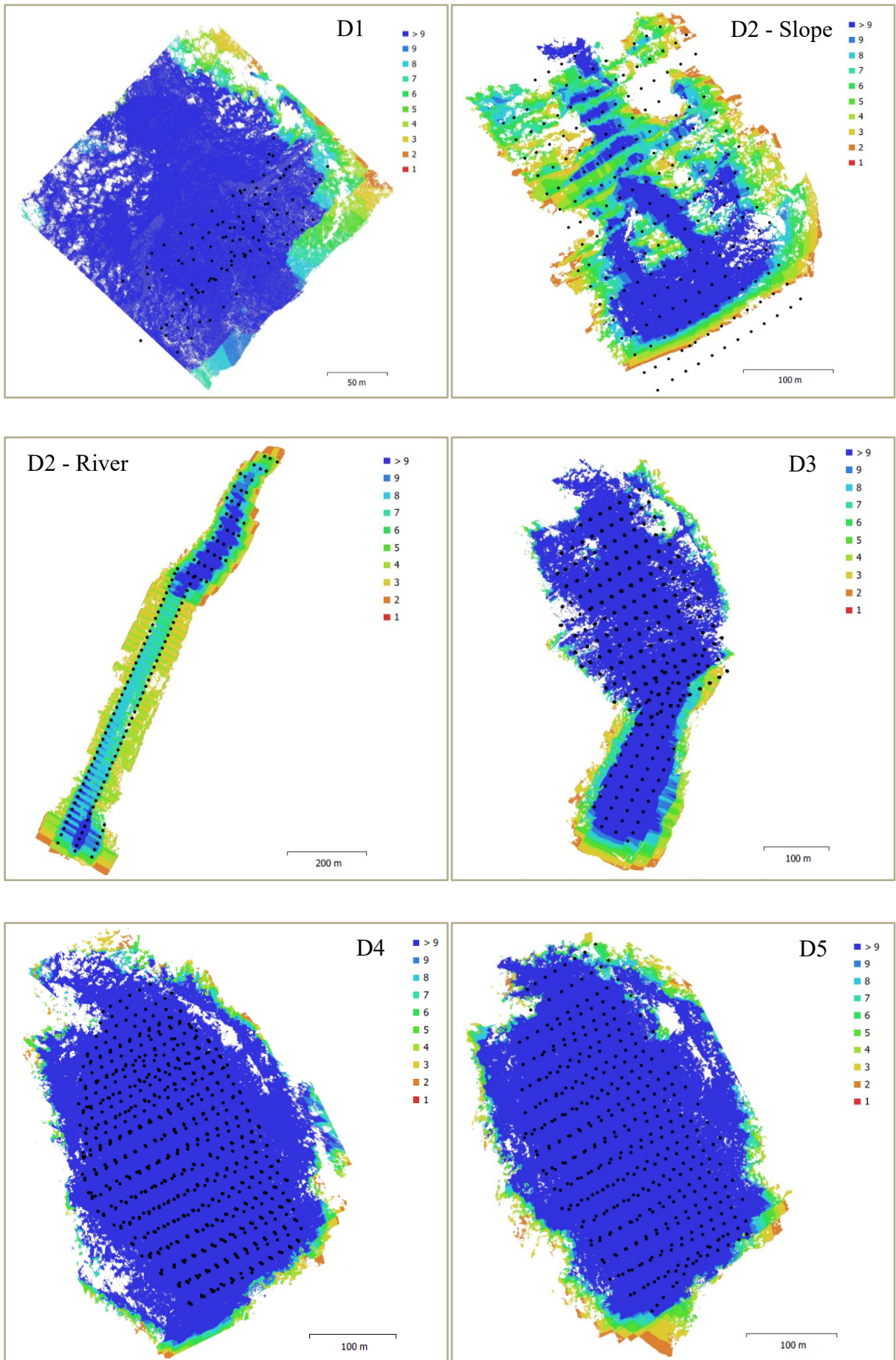


Figure 4-1 Example of image-matching of feature points: the blue lines stand for a valid matching, the purple one stand for an invalid matching.

During this process, the collinearity equations are solved and the camera motion is reconstructed by the estimation the camera locations. The accuracy of this process can be defined by the operator: medium, low and lowest setting cause image downscaling respectively by a factor of 4, 16 and 64; the highest accuracy setting, instead, upscales the images by a factor of 4 allowing a better estimation of the tie points location. Since this choice strongly affects the time of the processing, the default high accuracy setting was adopted and the software worked with the original size of the images (Agisoft Metashape user manual [2]).

The images come along with the camera position and rotation measured by the drone itself in a WGS84 (EPSG 4326) coordinate system, so they were used to perform a preliminary pair selection of the photos. It is also possible to perform a generic preselection of the overlapping photos by matching them using lower accuracy setting first. In order to reduce the time of processing, both reference and generic preselection were performed.

At this point, a sparse cloud of points is generated. The results of the alignment can be seen *Figure 4-2 (a)-(g)*. (Must be noted that the shown result come from merging the different chunks for every survey and this step is based on the markers that will be introduced only in the following steps). Most of the points, excluding the model D2, occur on more than 9 photos.



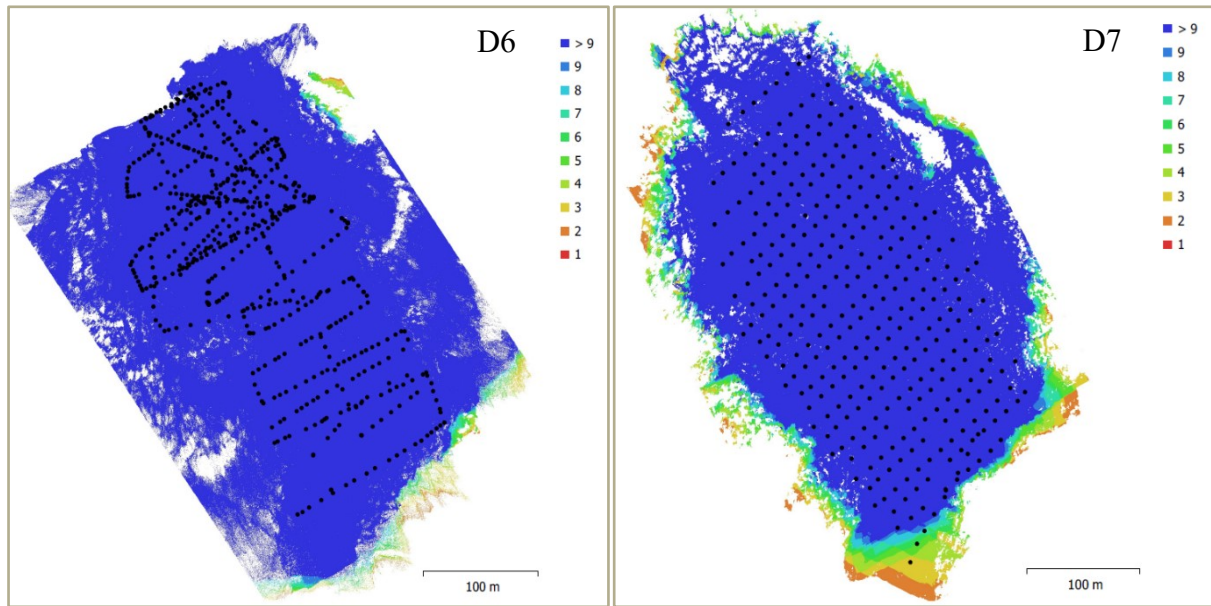


Figure 4-2 - Camera location and overlap of the images

4.2. Input of GCP coordinates

A three-dimensional model generated by aerial images by using an Unmanned Aerial Vehicles (UAV) can be used to perform accurate measurements only if it is properly registered in a specific coordinate system. In this way, the model can be easily loaded in geoviewers and geographic informative systems (GIS). There are two basic approaches to perform the georeferencing of the model: direct and indirect. The direct method is based on the presence of sensors that measures position (easting, northing and altitude) and orientation (yaw, pitch and roll) of the camera for every image (Reese et al. []). In this case, both the drones have a GPS (Global Positioning System) and GLONASS (GLObal NAVigation Satellite System) sensor installed. The indirect method is based on the access to the absolute position of some points in the interested area, with a level of accuracy accordingly to methodology adopted for the topographic survey. These points are called Ground Control Points (GCP), usually signalized with targets, and they can be introduced by inserting markers over the set of images: each marker is associated with one target visible and recognizable in a subset of images. The first solution is the cheaper and the less time-consuming, but it is very sensible to interference and it can be affected by vehicle malfunction or construction errors, so the estimated parameters may come with great uncertainties (Zhu et al. []). More accurate results can be achieved by meaning of the indirect georeferencing, even if it's an expensive and time-consuming method. In addition to the time required for the geodetic survey, the right positioning of each marker is not immediate and it may require a critical judgment from the operator. After adding a marker in a single photo where the target is visible, Agisoft Metashape is able to automatically recognize its projection in the other photos but this process isn't always precise, leading to different problem that requires the manual intervention:

- the projected marker can be far away from the actual target;
- even if the target is present, it can be not visible: it could be covered by the vegetation, abundant on the perimeter of the area of study where the target were placed, or it could

be overexposed due to the sunlight accordingly to weather condition, time of the day and spatial orientation of the target itself;

- low resolution of the target due to the distance of the camera: photographs taken over the middle portion of the area could contain the targets place at the bottom because of the steep inclination of the slope;
- perspective deformation of the target: this makes difficult recognizing the center of the target and this happen in most cases with the yellow circle targets that were placed on a sub-vertical or vertical surface (rock-wall or a tree).

If at first a number of projected markers in a range of 20-200 was found, after checking every singular photo it has been reduced to a number in the range of 5-30. The remaining markers were correctly placed in order to reduce the reprojection error in term of pixels, defined by the user manual [2] as “*the distance between the point on the image where a reconstructed 3D point can be projected and the original projection of that 3D point detected on the photo and used as a basis for the 3D point reconstruction procedure.*” In particular, for each marker the error (pix) is equal to the root mean square reprojection error calculated over all the valid tie points recognized in the images. The goal was to obtain a reprojection error lower than 0.5-0.6 pixels.

The points coordinates in terms of northing, easting and altitude in coordinate system of Slovenia 1996/Slovene National Grid (EPSG::3794) were then imported after correctly naming the label of each target: differently from a direct method of georeferencing, using GCPs requires a proper labeling of the measurements and an accurate scheme of the spatial distribution of the targets. The data from BF came with a value of accuracy for each GCP; the data from FGG didn't have any accuracy value and at this stage the default value of 0.005 m was applied. The later definition of this parameter is discussed in the chapter 4.4 *Optimizing georeferencing.*

By this process, the model is transformed by estimating 7 parameters (3 for translation, 3 for rotation and 1 for scaling) in order to obtain a valid reconstruction of the terrain, every point of which is associated to three spatial coordinates in a known reference system. This can also help to compensate the eventual linear errors in the first alignment of the cameras. Since the overlapping of the images and the shape of the terrain could lead also to non-linear deformation of the model, the camera alignment must be optimized. This is performed by the software thanks to an algorithm that minimizes the sum of reference coordinate misalignment error and reprojection error while adjusting the estimated point coordinates and the camera parameters. The operator can choose which camera parameter change in the optimization between:

- **f**: focal length;
- **cx, cy**: coordinates of the principal point;
- **b1, b2**: affinity and skew transformation coefficients;
- **k1, k2, k3, k4**: radial distortion coefficients;
- **p1, p2, p3, p4**: tangential distortion coefficients.

At this stage, the default options (f , c_x , c_y , k_1 , k_2 , k_3 , p_1 , p_2) were good enough to appreciate a strong correction of camera alignment.

Some markers showed greater value of error, indicating a possible outlier in the measurements. Before eventually remove these markers, the cleaning of the point cloud was performed in order to obtain better result from optimizing the cameras parameters in the following steps since this process is affected by the presence of mislocated points.

4.3. Cleaning the sparse point cloud by gradual selection

A Structure from Motion software allows to build a 3D model from a series of images by finding feature points in every image and simultaneously estimating the internal and external camera parameters. This process can lead to both linear and non-linear errors in the reprojection of the terrain into the virtual environment. Georeferencing the model by introducing the measured spatial coordinates of GCPs could compensate the linear error, but in order to correct the non-linear errors the optimization of camera parameters must be performed. This is a useful and powerful tool since it strongly affects the final result of the georeferencing. It is used every time after changing the GCPs in order to look for a possible outlier or selecting the proper set of CPs to verify the quality of the georeferencing. This is the reason why the sparse point cloud must be edited: the estimation of camera parameters and the quality of the reprojection depends on the presence of mislocated points.

The selection of the points to remove is performed by setting a threshold for each of these parameters:

- **Reprojection error:** it indicates a poor localization accuracy of corresponding point projections in the phase of point matching;
- **Reconstruction uncertainty:** it indicates a strong deviation from the object surface, so it's correlated to the noise in the point cloud (should not affect the accuracy of the optimization, but useful for a better visual appearance of the cloud);
- **Image count:** it indicates the number of photos in which every point is visible, it's directly proportional to location accuracy;
- **Projection accuracy:** it indicates the accuracy in localizing the projections of the points due to their size.

In order to find the best way to perform such selection, different approaches were considered in order to obtain a good reconstruction of the 3D model without losing too many points.

The approaches adopted and compared are:

- **CLEAN 0:** this method is the simplest and it has based on an application in archeological and cultural heritage studies by Dr. Heinrich Mallison [20]. A value of 80-90% of the maximum reprojection error was set as a threshold: points with greater error were removed. In case of reconstruction uncertainty and projection error, a threshold of 10 was set. After the removal of the points ended, the optimization of the cameras has been run with the default parameters selected. Due to the different kind of field of application, new approaches were tested.
- **CLEAN 1A:** this method introduced the principle of setting the threshold value in order to obtain the selection of 5-10% of the points of the sparse cloud, since the previous approached sometimes led to a very small or very large selection of points. The sequence of the parameters adopted in the gradual selection and the default options in optimizing the cameras were kept unchanged.
- **CLEAN 1B:** this approach mixes the methods CLEAN 1A and CLEAN 2. The order of the parameters used in the gradual selection and the 5-10% threshold principle were kept unchanged. After removing the selected points, the camera parameters were optimized each time: in case of reconstruction uncertainty and projection accuracy, all the parameters of the camera were considered.
- **CLEAN 2:** this method is based on the introductory training class in Unmanned Aircraft Systems Data Post-Processing proposed by United States Geological Survey (USGS) [32], the sole science agency for the Department of the Interior of the United States of America. This is the most complex method adopted, but it finds its application in the reconstruction of a terrain model from aerial surveys so it closer to this study. The sequence of the parameters used in the gradual selection changed and after removing the selected points the optimization of cameras was perform selecting all the camera parameters for the selections based on the projection accuracy and reprojection error. The selections based on the reconstruction uncertainty and projection accuracy were run twice. Also in this case the 5-10% threshold principle was adopted.

The image count wasn't considered in any of the methods and for any of the data sets, since setting a threshold number immediately lower then given value (3) would have selected a very large number of points, close to 50%. This process would have removed those points that are present only in 2 images but in these cases it would have strongly affected the characterization of the slope and the quality of the final model.

The parameters adopted for each data set is shown in *Table 4-2*.

In order to reduce the time of the cleaning process, for every survey the sparse point cloud generated from the different flights were merged into one single point cloud. This step was performed based on the position of the markers. A previous alignment of the models wasn't performed since the presence of the vegetation and holes in the model due to the complex geomorphology of the site would have led to bad results. Merging the point clouds wasn't accurate in one particular case, as it can be seen in the 5th chapter about the comparison of the models.

	D1	D2	D3	D4	D5	D6	D7
CLEAN 0							
Reprojection Error	1.2	0.4	0.4	0.4	0.4	5	0.5
Reconstruction Uncertainty	10	10	10	10	10	10	10
Projection Accuracy	10	10	10	10	10	10	10
<i>Optimize Cameras</i>	<i>default</i>						
CLEAN 1A							
Reprojection Error	1	0.25	0.25	0.255	0.325	0.8	0.32
Reconstruction Uncertainty	40	11	10.3	18	18.5	70	21.5
Projection Accuracy	7	10	9	9	4.5	6	5
<i>Optimize Cameras</i>	<i>default</i>						
CLEAN 1B							
Reprojection Error	1	0.25	0.25	0.255	0.325	0.8	0.345
<i>Optimize Cameras</i>	<i>all</i>						
Reconstruction Uncertainty	40	11	10.3	18	18.5	70	21.5
<i>Optimize Cameras</i>	<i>default</i>						
Projection Accuracy	7	10	9	9	4.5	6	5
<i>Optimize Cameras</i>	<i>all</i>						
CLEAN 2							
Reconstruction Uncertainty	40	11	10.2	17.5	18	70	21
<i>Optimize Cameras</i>	<i>default</i>						
Reconstruction Uncertainty	25	9.5	9.1	13.7	14.5	40	17
<i>Optimize Cameras</i>	<i>default</i>						
Projection Accuracy	6	10	8.7	9	4.5	5.5	5
<i>Optimize Cameras</i>	<i>all</i>						
Projection Accuracy	4.5	7	6.3	6.7	3.25	4	3.6
<i>Optimize Cameras</i>	<i>all</i>						
Reprojection Error	0.95	0.3	0.265	0.27	0.31	3.3	0.33
<i>Optimize Cameras</i>	<i>all</i>						

Table 4-2 – Parameters adopted to clean the sparse point cloud for each data set

The comparison of the results obtained from the several approaches took into account the reprojection error, RMS and maximum values, both in terms of tie point scale and pixel. Also the mean key point size, defined as the mean tie point scale averaged across all projections (Agisoft Metashape user manual [2]), was considered. This data is shown and compared in the following table (Table 4-3).

Since low values of both reprojection error and mean key point size stand for a better quality of the model, the approach that led to a greater reduction of this parameters was considered to be better choice in terms of cleaning method of the sparse point cloud. For the data from BF (D1, D6) the CLEAN 1A was considered valid; for the data coming from FGG (D2, D3, D4, D5, D7) the best results were given by the CLEAN 2 method.

D1		clean0		clean1a		clean1b		clean2		
	(tie point scale)	(pix)	(tie point scale)	(pix)	(tie point scale)	(pix)	(tie point scale)	(pix)	(tie point scale)	(pix)
RMS reprojection error	0.44859	1.49203	0.450383	1.44628	0.394557	1.28254	0.316235	1.04709	0.345499	0.967063
Max reprojection error	1.50529	50.9722	1.80856	14.7282	1.26058	8.2594	4.83173	16.2439	1.92515	9.76729
Mean key point size		4.02243		3.65893		3.45326		3.45319		2.8431
RMS reprojection error			0%	-3%	-12%	-14%	-30%	-30%	-23%	-35%
Max reprojection error			20%	-71%	-16%	-84%	221%	-68%	28%	-81%
Mean key point size				-9%		-14%		-14%		-29%
D2		clean0		clean1a		clean1b		clean2		
	(tie point scale)	(pix)	(tie point scale)	(pix)	(tie point scale)	(pix)	(tie point scale)	(pix)	(tie point scale)	(pix)
RMS reprojection error	0.121534	0.76145	0.125446	0.557289	0.102436	0.477515	0.100674	0.472023	0.104084	0.429249
Max reprojection error	0.474765	33.3762	0.436036	5.37238	0.335167	3.17903	0.41585	3.22726	0.30577	2.54935
Mean key point size		5.62266		4.42394		4.51222		4.5122		4.01009
RMS reprojection error			3%	-27%	-16%	-37%	-17%	-38%	-14%	-44%
Max reprojection error			-8%	-84%	-29%	-90%	-12%	-90%	-36%	-92%
Mean key point size				-21%		-20%		-20%		-29%
D3		clean0		clean1a		clean1b		clean2		
	(tie point scale)	(pix)	(tie point scale)	(pix)	(tie point scale)	(pix)	(tie point scale)	(pix)	(tie point scale)	(pix)
RMS reprojection error	0.123945	0.65461	0.12503	0.508526	0.101787	0.425389	0.0996336	0.41884	0.107111	0.396414
Max reprojection error	0.537403	26.0588	0.479366	4.7877	0.328713	3.27419	0.592368	3.3158	0.354254	2.54416
Mean key point size		4.95319		4.16512		4.15259		4.15266		3.70377
RMS reprojection error			1%	-22%	-18%	-35%	-20%	-36%	-14%	-39%
Max reprojection error			-11%	-82%	-39%	-87%	10%	-87%	-34%	-90%
Mean key point size				-16%		-16%		-16%		-25%

D4			clean0		clean1a		clean1b		clean2	
	(tie point scale)	(pix)	(tie point scale)	(pix)	(tie point scale)	(pix)	(tie point scale)	(pix)	(tie point scale)	(pix)
RMS reprojection error	0.124162	0.808838	0.13174	0.633322	0.102442	0.473464	0.1006	0.467098	0.106869	0.447122
Max reprojection error	0.539106	32.3113	0.588701	8.29625	0.346144	4.33882	0.483638	4.34716	0.353523	3.04953
Mean key point size		5.69145		4.75683		4.56778		4.56777		4.16676
RMS reprojection error			6%	-22%	-17%	-41%	-19%	-42%	-14%	-45%
Max reprojection error			9%	-74%	-36%	-87%	-10%	-87%	-34%	-91%
Mean key point size				-16%		-20%		-20%		-27%
D5			clean0		clean1a		clean1b		clean2	
	(tie point scale)	(pix)	(tie point scale)	(pix)	(tie point scale)	(pix)	(tie point scale)	(pix)	(tie point scale)	(pix)
RMS reprojection error	0.146435	0.532743	0.151065	0.435068	0.132294	0.329517	0.127905	0.318857	0.128908	0.300076
Max reprojection error	0.519732	35.5832	0.479438	6.96117	0.401905	2.70325	0.768145	2.68248	0.403576	1.87511
Mean key point size		3.12561		2.87559		2.47334		2.47332		2.30816
RMS reprojection error			3%	-18%	-10%	-38%	-13%	-40%	-12%	-44%
Max reprojection error			-8%	-80%	-23%	-92%	48%	-92%	-22%	-95%
Mean key point size				-8%		-21%		-21%		-26%
D6			clean0		clean1a		clean1b		clean2	
	(tie point scale)	(pix)	(tie point scale)	(pix)	(tie point scale)	(pix)	(tie point scale)	(pix)	(tie point scale)	(pix)
RMS reprojection error	0.364538	1.36823	0.405166	1.33715	0.308828	0.951532	0.259039	0.79793	0.368258	0.903112
Max reprojection error	5.35579	67.7545	1.72737	23.425	1.47643	11.1005	2.66074	11.2926	3.78682	8.77023
Mean key point size		3.98072		3.65581		3.05137		3.05127		2.47855
RMS reprojection error			11%	-2%	-15%	-30%	-29%	-42%	1%	-34%
Max reprojection error			-68%	-65%	-72%	-84%	-50%	-83%	-29%	-87%
Mean key point size				-8%		-23%		-23%		-38%

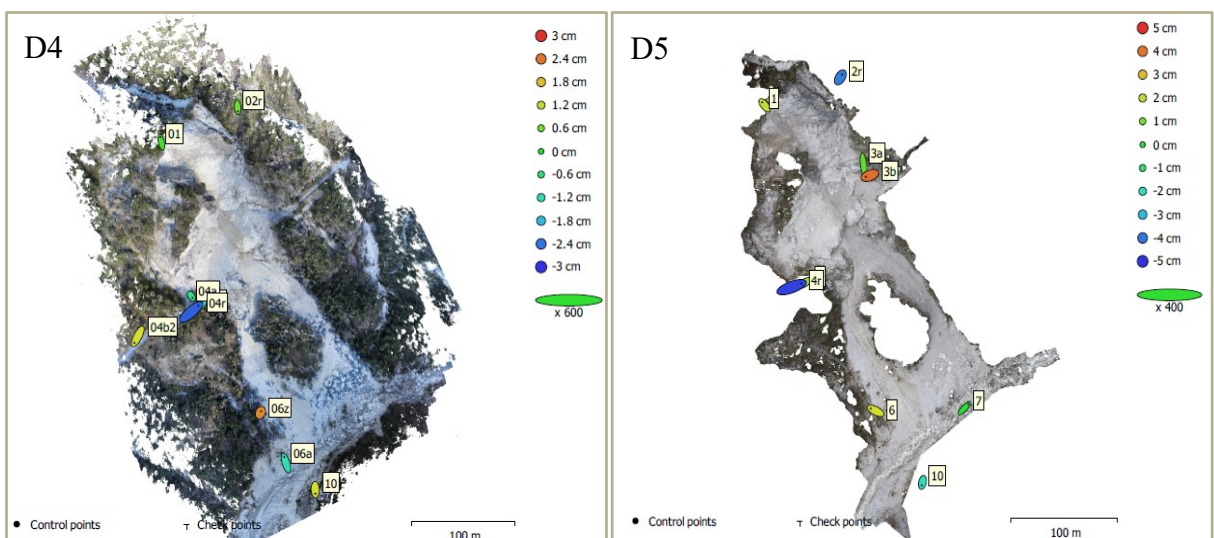
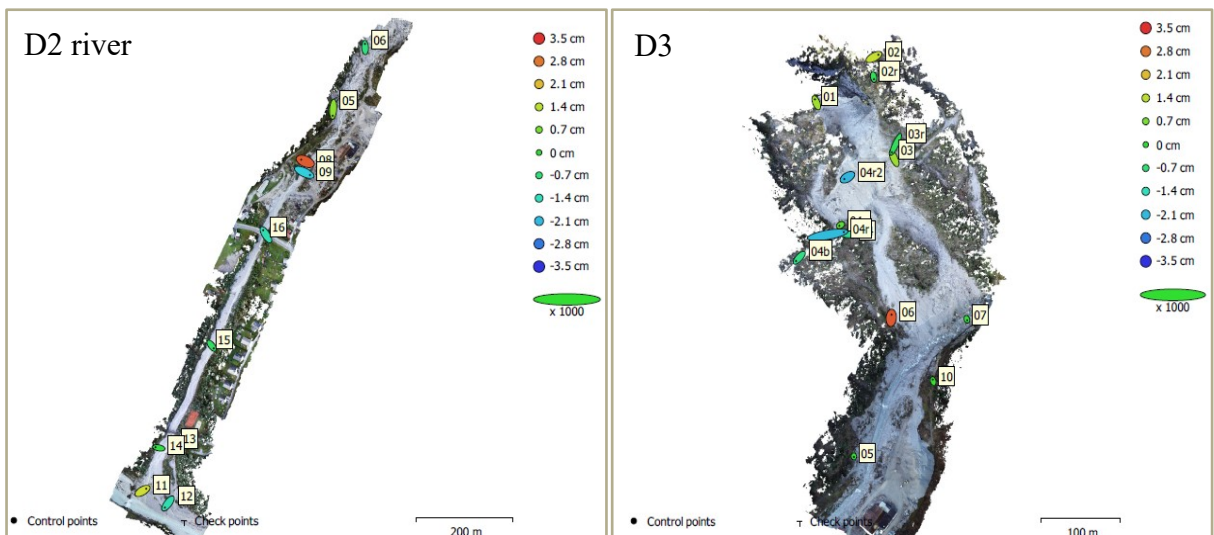
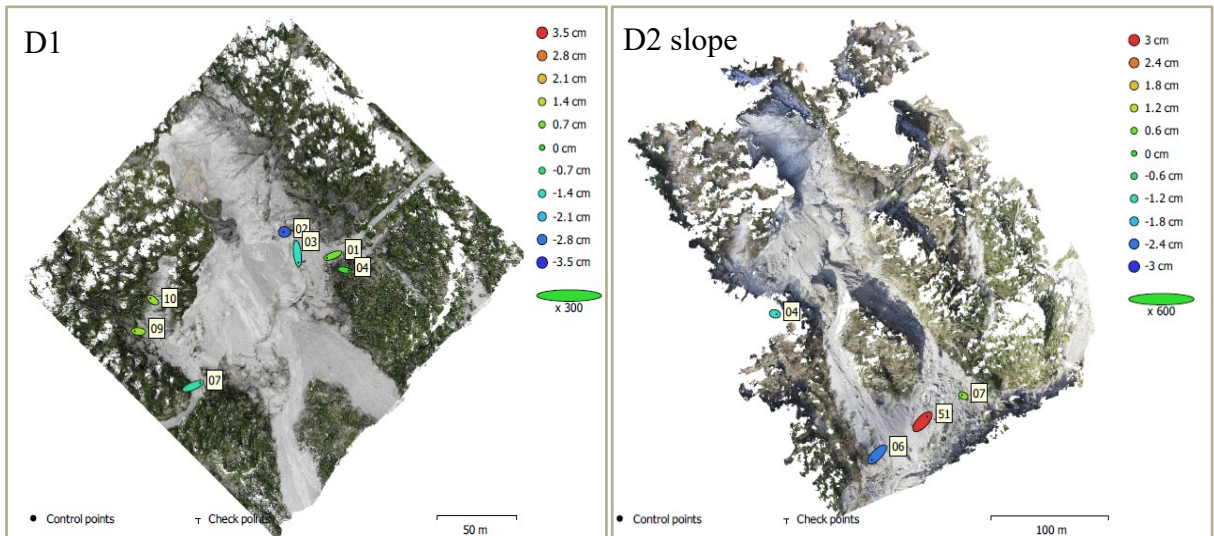
D7		clean0		clean1a		clean1b		clean2		
	(tie point scale)	(pix)	(tie point scale)	(pix)	(tie point scale)	(pix)	(tie point scale)	(pix)	(tie point scale)	(pix)
RMS reprojection error	0.155897	0.589161	0.170187	0.519024	0.13264	0.346078	0.134819	0.352004	0.135894	0.324231
Max reprojection error	0.699571	33.6914	0.638383	7.55654	0.67629	3.29102	0.973598	3.10915	0.7975	2.87678
Mean key point size		3.29504		2.96231		2.5762		2.5748		2.35985
	RMS reprojection error		9%	-12%	-15%	-41%	-14%	-40%	-23%	-45%
	Max reprojection error		-9%	-78%	-3%	-90%	39%	-91%	28%	-91%
	Mean key point size			-10%		-22%		-22%		-28%

Table 4-3 – Values of reprojection error, RMS and maximum values, both in terms of tie point scale and pixel and values of mean key point size in pixels

4.4. Optimization of the georeferencing

The construction of a 3D model by means of SfM photogrammetry representing the actual shape and size of an object, in this case a slope characterized by a rock mass and some debris deposits, requires the definition of both interior and exterior parameters of the cameras. A SfM software allows a preliminary definition of those features starting from the information that comes with the images. A better definition of the position and rotation of the camera at the time when every image was taken can be defined by introducing several Ground Control Points (GCPs) in order to perform an indirect georeferencing of the model. This process performs a transformation of the point cloud in terms of translation, rotation and scaling with the purpose to better fit the input coordinates of the GCPs with the estimated position of the associated targets present in the model. However, in Metashape introducing some GCPs allow also to constrain the bundle block adjustment, as suggested by Benassi et al. [4] The amount and the spatial distribution of GCPs affect the quality of the final registration: the minimum request is having at least three non-collinear points. A good distribution over the entire area of study allows to prevent a rotation of the point cloud around the GCP and an incorrect size definition of the model. A great amount of GCPs grants a more rigid registration of the model but they require also a greater number of resources, in terms of cost and time. Both these conditions are then affected by the accessibility of the site: the area could be so impervious to not to guarantee a safe path to all the regions of the site; the presence of obstacles such as the vegetation could also affect the visibility of the targets.

Taking into account all these considerations, even in the best scenario the quality of the georeferencing and so the validity of the 3D terrain reconstruction is dependent to the accuracy of the position measurement of the target on site. This is performed by a geotopographic survey that could be carried out by different methods, involving different technologies, different instruments and different operations. Such procedure isn't perfect: it is affected by gross errors that can be avoided by performing redundant measurements, systematic errors that follow a certain pattern and random errors that may cause small unavoidable fluctuations in the registration of the data. This could lead to the presence of some outliers or measurements so inaccurate to significantly reduce the quality of the registration. So, at this stage, thanks to a preliminary georeferencing of the models an estimation of the error in the reprojection was possible. In order to minimize the total error averaged over all the GCP or at least having a value lower than 10 cm, the projection of some markers was removed and their coordinates weren't considered in the georeferencing process. The final GCPs adopted for each model are listed in the *Appendix B (Figure B-1)* and shown in *Figure 4-3*: the shown values of error, in case of the data from FGG, refer to a value of accuracy set by the user and defined as it will be discussed in the following paragraphs.



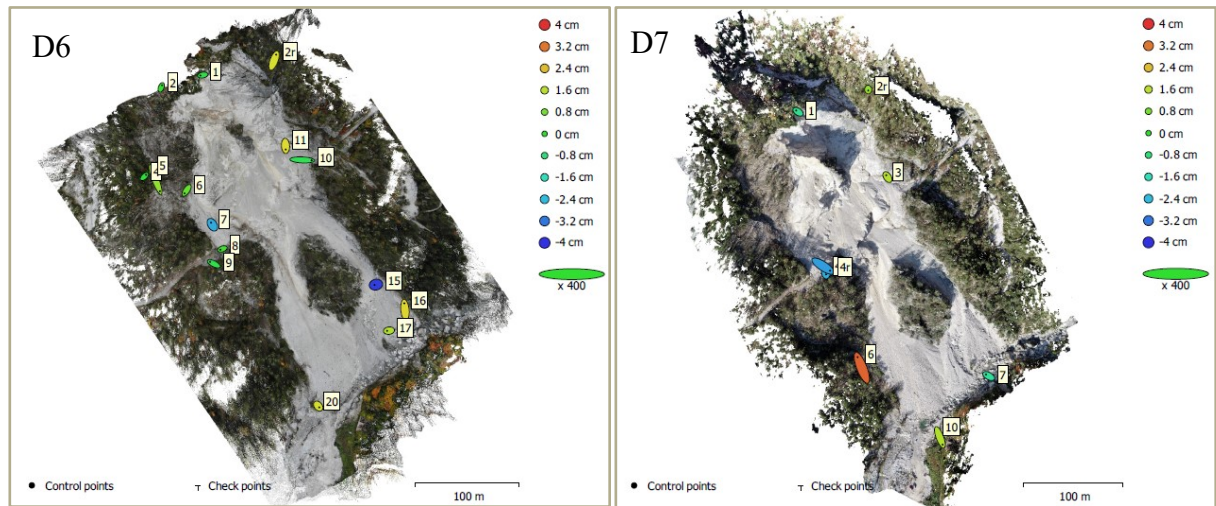


Figure 4-3 – Spatial distribution of the GCP adopted in the the georeferencing process and the error in meters along the easting (x), northing (y) and altitude (z) direction is shown for every marker; in case of the data from FGG (D2, D3, D4, D5, D7) the shown errors refer to a level of accuracy set by the user.

The values of northing, easting and altitude for each remaining GCP are not precise but they come with a level of uncertainty.

For the data from BF, the level of accuracy for each GCP is given: it goes from 0.018 to 0.038 m, with a mean value of 0.024 m, for the first survey (D1) if one GCP with an accuracy of 5 m is not considered; it goes from 0.011 m to 0.032 m, with a mean value of 0.02 m, for the second survey (D6). Although the surveying method has not been shared.

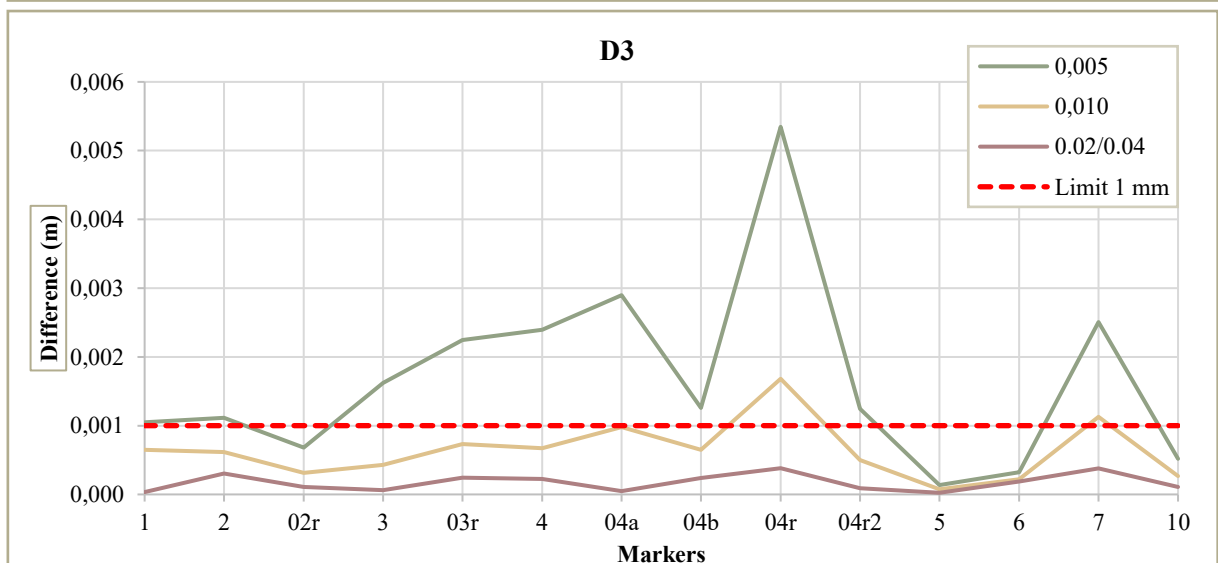
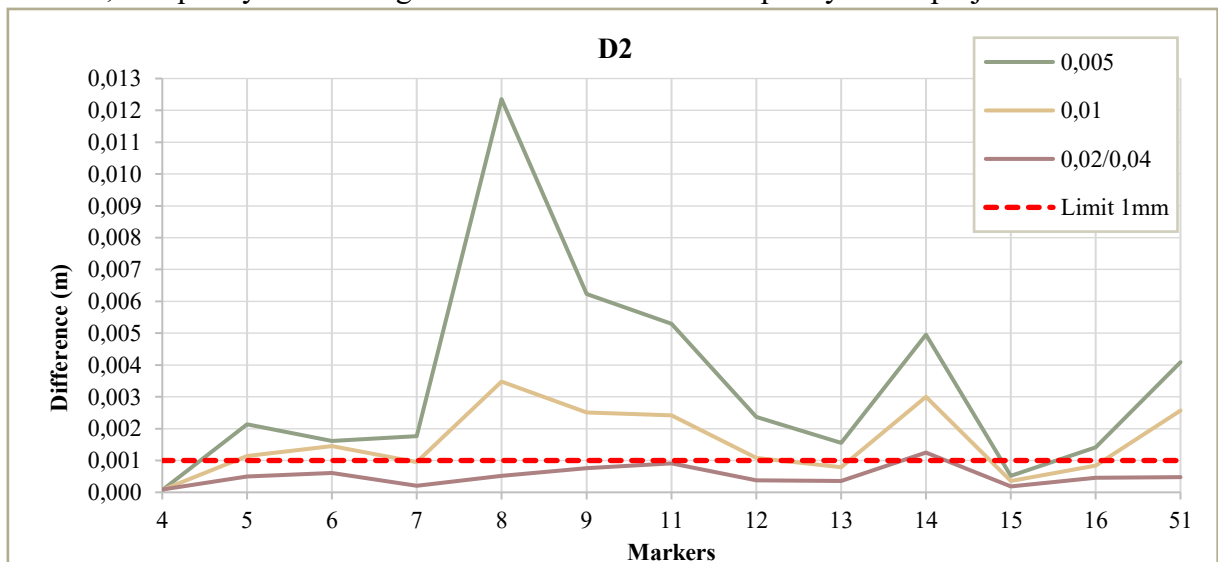
For the data from FGG, instead, a value of accuracy is not defined. For this reason, a simple method which reliability is yet to be demonstrated has been adopted to find a reasonable value. The first survey (D2) was carried out by RTK GNSS and its expected accuracy was around 0.04 m in the horizontal direction and 0.08 m in the vertical direction; due to a low intensity of the signal that led to unprecise measurements in some portion of the site, the methodology changed for the following surveys and a combination of GNSS and tachometry was adopted, achieving an accuracy in the rank of 0.02 in the horizontal direction and 0.04 m in the vertical direction.

This estimated values of accuracy were tested in order to verify if they were low enough to guarantee a short difference in the reprojection error of the same marker used as GCP and and then as CP: a big difference would have highlighted a non-homogeneous distribution of the error in the registration of the model, due to an over-estimated level of accuracy that would have forced the fitting of the model in some portion of the point cloud. In order to observe such behavior, the following method has been adopted. Three different values of accuracy were considered: 0.005 m (the default parameter), 0.01 m and 0.02/0.04 m (0.04/0.08 m for D2). For each marker, for a given accuracy, the reprojection error as GCP was compared to the value as CP, both before and after optimizing the cameras in order to check any significant change. The optimization of the camera led to very different values and no useful pattern was recognized while changing the accuracy: the results are shown in *Appendix A*. The comparison between the error as GCP and as CP is shown in the following graphs (*Figure 4-4*): the results show how high level of accuracy lead to a greater difference

between the estimated position of the few marker and their actual coordinates, as highlighted by the pikes; lower accuracy, so a wider level of confidence, instead reduced such differences and guaranteed a more flat distribution indicating an homogenous distribution over all the markers of the uncertainty of the terrain reconstruction.

At the end, the proposed accuracies of the measurements satisfied the expectations since all the differences were lower than 1 mm. Even if in one case (D4) this condition was verified with a value of 0.01 m, it is considered to be more conservative not to over-estimate the accuracy.

The same test was adopted to check the accuracy given by BF: a flat distribution was recognized for high levels of confidence, around 0.10 m, that would have increased the reprojection error and reduce the quality of the reconstruction. Not knowing the surveying method adopted it's difficult to judge the reliability of the data, so in order to not underestimated too much the accuracy the given values were considered in the elaboration. It must be noticed that in these cases, (D1, D6) the distribution and amount of GCPs, if related to the scale of the model, are good enough to compensate the tilt and distortion of the model. Also, the quality of the images could have affected the quality of the projection.



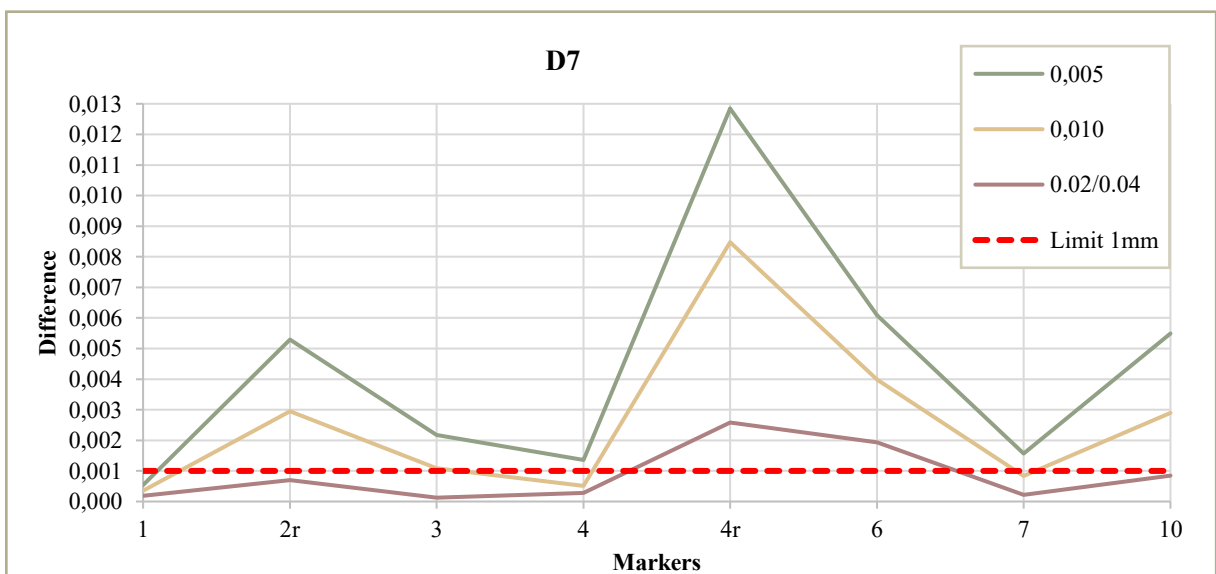
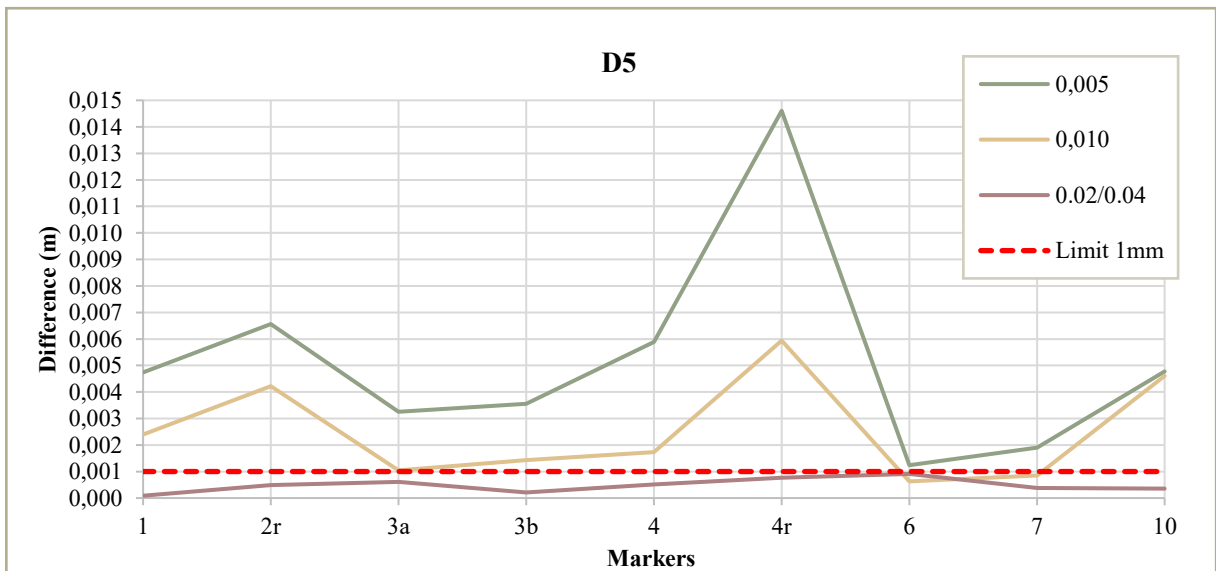
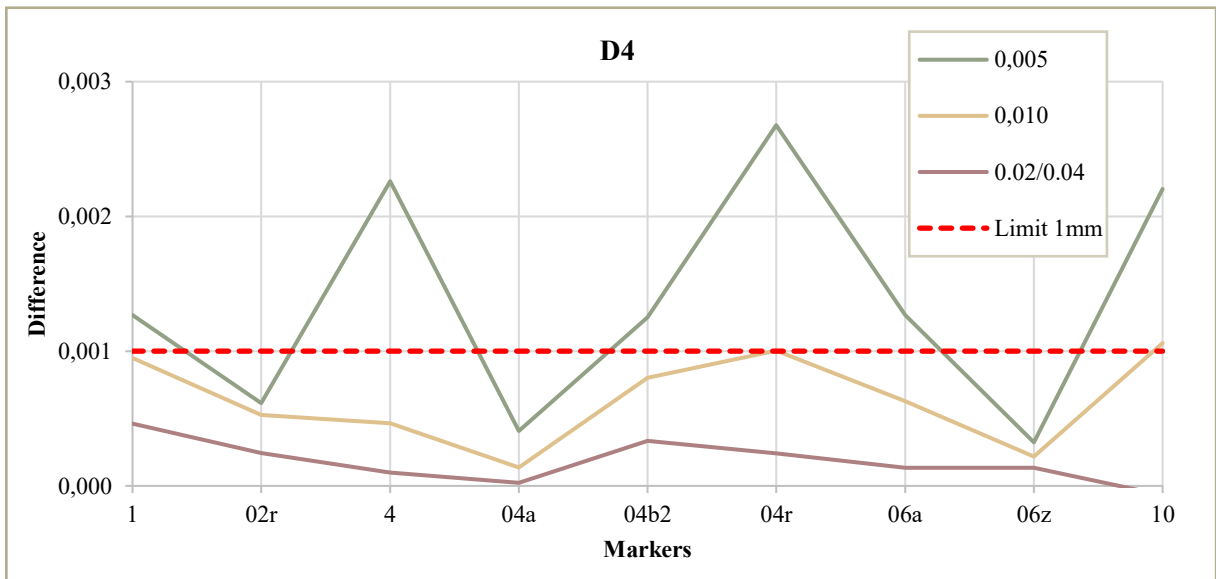


Figure 4-4 – Distribution of the difference between the reprojection error of each marker considered as GCP and then as CP.

4.5. Building of dense point cloud

Now, the point clouds are ready to be used for building a dense point cloud with far more information. Bemis Metashape elaborates a depth map for every image starting from the estimated camera locations. This means that after this process no camera optimization can be run without losing the dense cloud, so the reference system must be defined and properly optimized. The camera positions were estimated considering all the valid markers as GCP, for several reason:

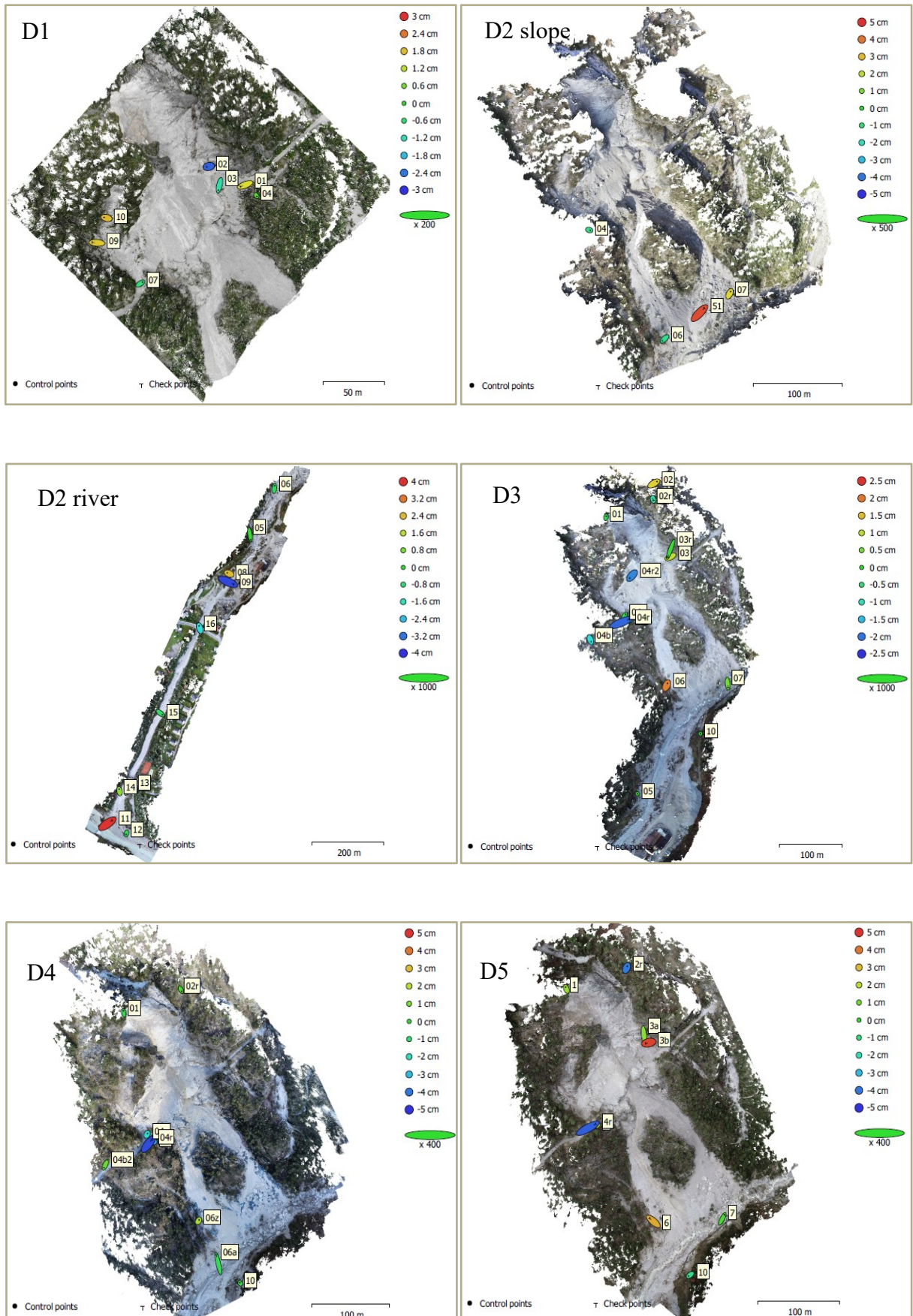
- low number of markers available if compared to the scale of the site of interest;
- poor distribution of the markers due to the reduced accessibility of the slope;
- complexity of the geomorphology (niches, isolated blocks, rock-walls oriented in different directions) that could easily lead to a poor reconstruction and a distortion of the model.

This process is carried out after the selection of some reconstruction parameters set by the user:

- **Quality:** it goes from lowest to ultrahigh, accordingly to the same principle adopted in the accuracy of the photo alignment previously discussed; since these parameter strongly affect the time of processing and the amount of point of the cloud, the quality was set as medium in order to reduce the time of elaboration and guarantee an easier manipulation of the point cloud the Cloud Compare environment. The processing time for each project was around 30-40 minutes.
- **Depth filtering modes:** it allows the user to set which algorithm use in order to avoid outliers in the point cloud due to noisy or badly focused images and the decision is between mild, aggressive and disabled. Even if aggressive filtering algorithm is suggested for aerial photographs, applied to our models it led to the removal of some spots over the slope and its contribution in removing the noise due to the vegetation wasn't significant. So the mild algorithm was adopted to better reconstruct the geometry of the terrain and the noisy areas would have been later removed manually.
- **Calculate point colors:** it allows the user to decide whether obtain a colored or a grey dense point cloud. This option was abled since the color of the point would have helped in the following process of points classification.
- **Reuse depth maps:** it gives the opportunity to reuse depth maps available in the chunk.

Before building the dense point cloud, a verification of the accuracy of the model reconstruction was carried out by selecting few CPs among the valid markers. Due to a low number of GCPs available and a limited distribution of those, very few markers were used as CP. This means that the reprojection error of CPs, listed in the *Appendix B (Figure B-2)*

and shown in *Figure 4-5*, are not very representative of the overall quality of the model but they give a local information of the obtained results.



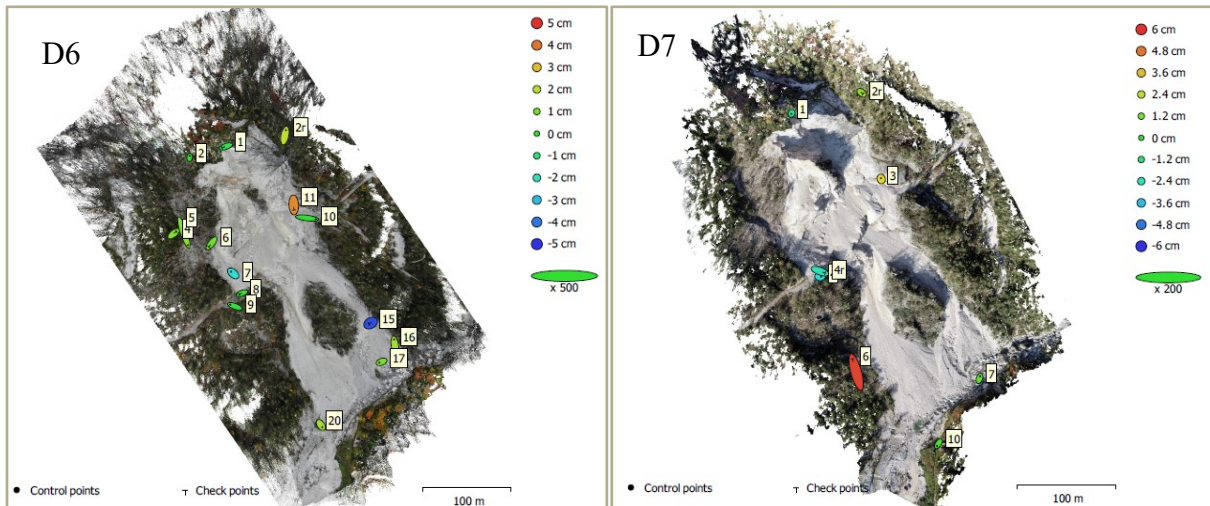


Figure 4-5 - Spatial distribution of the GCPs and CPs adopted for checking the accuracy of the generated model; the error in meters along the easting (x), northing (y) and altitude (z) direction is shown for every marker.

4.6. Classification

The Digital Surface Model (DSM) is the representation of the surface of the earth considering the presence of all the natural and artificial objects, such as vegetation, buildings, roads, etc. The Digital Terrain Model (DTM), instead, is the representation of surface of the ground without any artificial object and without any vegetation; this mean that DTM comes after the elaboration of a DSM from which non-ground point are identified and assigned to a class that regroupes the point of a particular category of objects (cars, buildings, high vegetation, roads, etc.). A simplified scheme is shown in *Figure 4-6*.

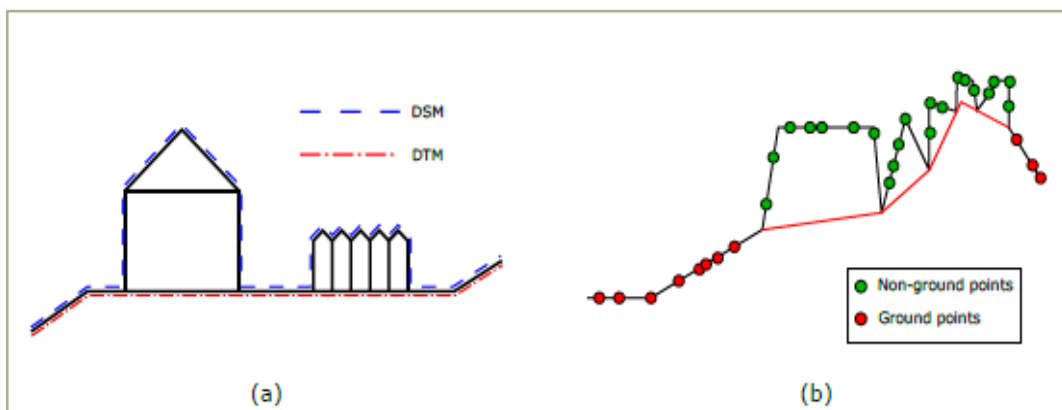


Figure 4-6 – Schematic difference between the Digital Surface Model (DSM) and the Digital Terrain Model (DTM). (Figure from Meza et al. [21])

Figure 4-7 shows how DSM and DTM can be very different especially in urban areas.

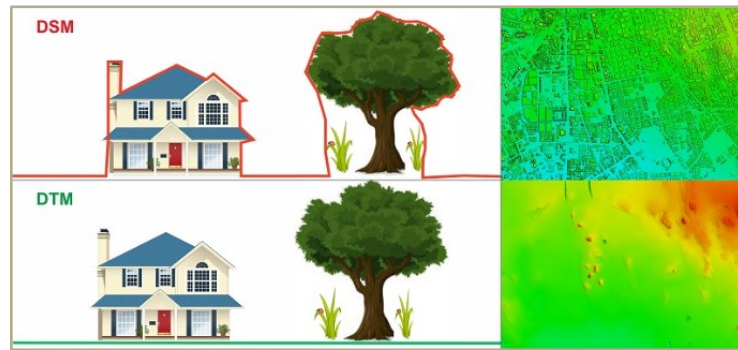


Figure 4-7 – Difference between the DSM and the DTM in an urban area. (Figure from <https://3dmetrica.it/dtm-dsm-dem/>)

The classification of point cloud with the purpose of obtaining a DTM can be often a critical operation, especially in natural and complex landscape where we can find a dense forest of high vegetation and a diversified geomorphology. The manual selection of the points for every class can be the most reliable method but certainly the most time-consuming accordingly to the scale of the model. In the last 20 years, many algorithms were studied to automatize this process and literature is rich of studies that compare their results and highlight their limits. There are four main categories of approach in order to perform such a classification and they differ for the assumed structure of the ground points:

1. progressive densification filters starting from seeds (for example the detection of the lowest point);
2. surface-based filters that progressively remove the points that don't fit the surface model;
3. morphological filters;
4. segmentation and clustering-based filters that work in homogenous portions of the model rather than on every single point.

Studies carried out by Sithole et al. [29] on the application of different filtering algorithms on rural landscapes, urban areas and rough terrain with vegetation revealed that filters that estimate local surfaces are found to perform best. For this reason, it was worth it to try different solutions applying the algorithms that come with Agisoft Metashape and CloudCompare.

In the first case, the Classify Ground Points algorithm was used. The software was able to perform an automatic classification of ground points following these steps:

- I. the dense point cloud is divided into cells of a certain size, which is defined by the user accordingly to the size of the largest area that doesn't contain any ground point;
- II. in each cell, the lowest point is detected;
- III. a first approximation of the surface model is carried out by the triangulation of the lowest points;
- IV. each point of the cloud is tested to satisfy two conditions:
 - a) it must lie within a certain maximum distance from the terrain model defined by the user accordingly to the maximum variation of the ground elevation;

- b) the angle between the terrain model and the line that connect the point and with a ground point must be lower than a maximum angle defined by the user accordingly to the presence of steep slopes.

Difference tests were performed changing the cell size, the max distance and the max angle but none of those led to good results: in every case many portions of the slope were not classified as ground and in some cases portion of the vegetation were misclassified, causing a necessary intervention of the user to perform a long and precise manual classification.

Given such results, some tests were carried out by using Cloth Simulation (CS) filter, thanks to the plug-in integrated in the last version of CloudCompare. The details of the algorithm and the definition of the parameters that the user can manipulate are better described by Zhang et al. [36]. The main steps, illustrated in *Figure 4-8*, are:

- I. the point cloud is inverted and a cloth is place above it;
- II. each particle of the cloth moves accordingly the influence of gravity;
- III. the particles now under the ground are moved close to the ground and set as unmovable;
- IV. the other particles move under the influence of the internal forces produced by neighbor particles accordingly to their distance and the stiffness of the cloth set by the user.

The parameters that would set the simulation process were changed in order to find out the best result. The main problem was to let the cloth adapt to the asperities and niches of the rock mass: every test left out some portion of the terrain and none of the parameters configuration led to a good representation of the entire slope.

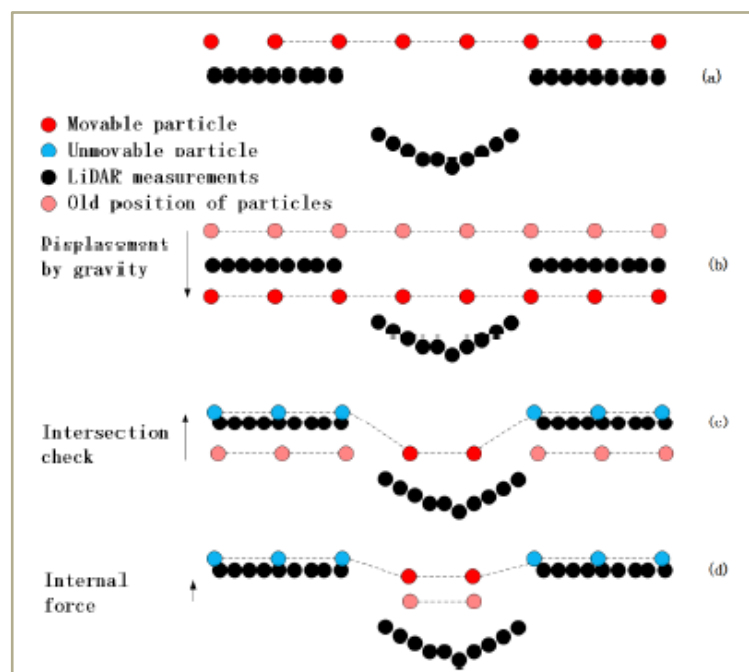


Figure 4-8 – Main steps of the Cloth Simulation filter. (Figure from Zhang et al. [36])

The many difficulties in finding the best automatic classification of the ground point by using both the presented methods made inevitable the manual intervention of the operator. In order

to facilitate this task, a first preliminary classification was performed by using a simplified method. A multi-class classification has been run in Agisoft Metashape and thanks to the machine learning techniques an automatic classification of the point cloud in different classes (ground, high vegetation, building, car and man-made) was possible. The absence of artificial elements on site allowed to select only two output classes (ground and high vegetation), allowing to speed up the process. Since only the ground points were the matter of interest, the same classes were adopted in classifying the riverbanks and the artificial objects from the data D2. The other parameter that the user can change is the level of confidence: it goes from 0 to 1 and high values mean that the point which class cannot be reliably assigned would remain unclassified. For simplicity, it was set equal to 0. The obtained results were not precise, but good enough to make easier and faster the manual classification. This one was performed roughly in the vegetated areas, where an accurate selection of the ground points would have led to a terrain full of holes. For this reason the forests on the sides of the area of interest and the portion in the middle of the bottom area were classified as high vegetation: the future comparison of the models will not show any possible change detection in these areas. Isolated trees and bushes have been individually selected and classified: avoiding the presence of some holes was not possible.

5. Point Cloud Comparison

CloudCompare is an open source software originally designed to process and compare both 3D point clouds and triangular meshes. Its development began in 2003 and in the last years it evolved into a more generic 3D data processing software, including different kind of algorithms allowing to perform registration, noise filtering, point classification, normal computation and many other functions.

After importing the dense point cloud into the software, the general workflow would be:

- I. noise filtering;
- II. alignment of the point clouds;
- III. distance computation between the models;
- IV. volume change computation.

5.1. Noise filtering

The first step consists in removing no-useful and noisy points from every single point cloud. Differently from the Gradual Selection in Agisoft Metashape already discussed, CloudCompare allow to automatically remove some points considering the geometry of the point cloud and the relative position and distance of each point. The following tools have been used in order to obtain a clean point cloud with a homogeneous surface density:

- **Remove duplicate points:** the software will remove those points that are closer than the minimum distance set by the user; in this case, in order to reduce the number of points and facilitate the manipulation of the cloud, was set a threshold of 1 cm.
- **Subsample:** this tool allows to reduce the number of points accordingly to three different methods, which are random, spatial and octree based. The spatial method was adopted and the minimum space was set equal to 5 cm; this allowed the generation of a second point cloud, that is a subset of the input one and which original points were not displaced. The subsampled point cloud keeps all the features of its source cloud as scalar fields, colors, normal, etc.
- **S.O.R filter/Noise filter:** these tools are very similar, since for every point they both remove points that exceed a certain distance from the plane fitting a certain number of neighbors (kNN). The difference is that S.O.R. (Statistical Outlier Removal) filter uses a constant number of neighbors defined by the user and removes the points according to a relative error: the maximum distance is equal to the average distance plus the standard deviation multiplied by a factor (nSigma) chosen by the user. Noise filter, instead, allows the user to choose a constant radius that will define the number of neighbors and the constant maximum distance from the fitting plane. At first, SOR filter results were tested: a constant number of kNN of 100 and a nSigma of 1 were able to remove most of the noisy points from the perimeter and the holes of the point cloud. The only exception was the point cloud from data D1: the filtering process

would affect the density of the overall model, so it wasn't performed. A comparison from the D2 data set is shown in *Figure 5-1* as a significant example.

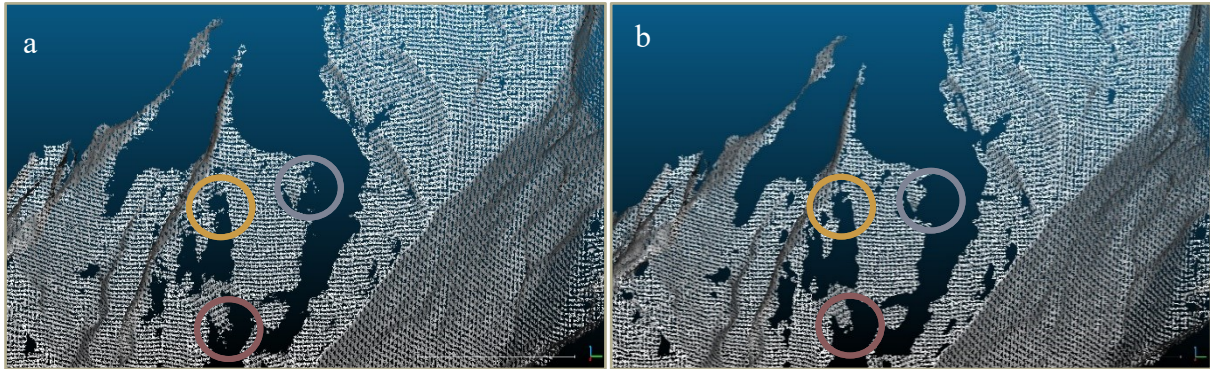


Figure 5-1 – Comparison of the result before (a) and after (b) using the SOR filter;

5.2. Registration

The second step of the workflow consists in the alignment of the point clouds that are supposed to be compared. A visual inspection of the point clouds is performed to verify the quality of the automatic projection of the points into the software environment: the only unmovable artificial objects in the scene were the portions of two roads crossing the sides of the middle section of the slope. In some cases, there was a good correspondence, in others a vertical offset was visually clear. This distance was measured by using the tool Point Picking, which allows to establish the distance and its projection in the three directions (x, y, z) between two points. After detecting the Δz for multiple points of the roads, one of the two point clouds was rigidly translated in the vertical direction of an average value of Δz . Since the references for the registration of the point clouds were two areas along one direction, this approach was adopted to perform a preliminary registration but it was not considered good enough to judge the overall alignment of the models since it wasn't possible to verify an incorrect rotation of the model that would have affected a bad alignment at the top and at the bottom of the slope.

In order to avoid a misestimation of the changes between two point clouds, an automatic fine registration was performed. The software uses an Iterative Closest Point (ICP) algorithm that allows to align two entities if the following assumptions are granted: both point clouds must be already roughly registered and both point clouds must represent the same object or at least have the same shape on the overlapping parts. Given these conditions, the user can set different parameters:

- Number of iterations/RMS difference
- Final overlap
- Adjust scale
- Random sampling limit
- rotation/Translation
- Enable farthest point removal
- Used displayed model/data scalar field as weights

Some tests were performed changing the parameters but most of the results led to a worse registration of the point clouds: the one selected as Data (movable) translated and rotated in different direction far away from the one set as Model (unmovable). No optimum setting of parameters was found to perform a finely registration. The main cause could be the presence of great differences on large scales between the two point clouds.

As an alternative, in CloudCompare is possible to perform an alignment of two entities by point pairs picking. The principle behind this procedure is selecting at least three equivalent point pairs in both clouds. This requires a well distributed presence of recognizable points all over the model. Ideally this function could be covered by the targets used during the surveys but most of them are not in the DTM since they were placed close to vegetated (or poorly reconstructed) areas or they are not recognizable in the scene.

Given the limits of the available algorithms to register the two point clouds that must be compared, the preliminary registration was considered the best result.

5.3. Estimation of cloud-to-cloud distance

CloudCompare is an independent open source project and its most common application is the comparison of two entities, that could be two point clouds or one point cloud and a mesh. Surface changes measurements usually are purchased by two different approaches:

- a) computation of a displacement field by tracking of homologous parts of the surface, usually applied to monitor landslides;
- b) calculation of the distance between two model, usually applied when there aren't homologous parts in the scene.

The rock fall and the debris flow are instability phenomena usually not characterized by the slow mobilization of a deformable mass. In the first case, one or more blocks detach from a niche and they reach the valley or an obstacle in different ways, by rolling or jumping or a combination of both; in the second case we have different blocks, already detached, with similar or different sizes, and even if in some occasions a soil-like behavior can occur, singular blocks can flow by their own. For this reason and accounting the total absence of recognizable movable homologous parts, the distance computation approach was adopted.

In order to perform such procedure, the software uses different tools:

- **Cloud-to-Cloud comparison (C2C):** it is a method based on the detection of the closest point by a kind of Hausdorff algorithm that finds the nearest neighbor distance or by computing the distance from a local model of the reference point cloud, defined by the least-square best fitting plane going through the nearest point and its neighbor. This procedure doesn't allow to distinguish between negative and positive changes, but it's the simplest and fastest solution to observe the difference between two point clouds. The final accuracy of the distance estimation is affected by the density of the point clouds and the overlapping of the models: the reference point cloud extents

should be wider than the compared ones in order to avoid virtually high distances on the boundaries.

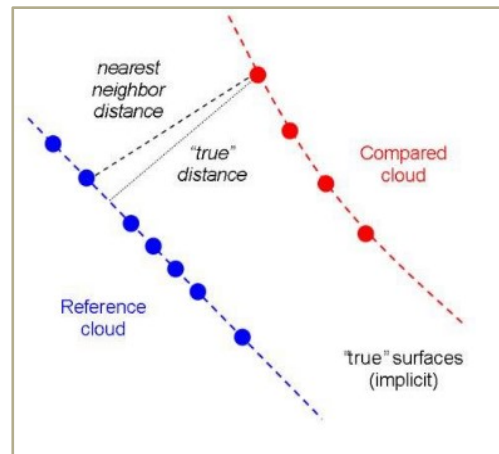


Figure 5-2 – Scheme of the principle of how C2C works. (Figure from CloudCompare user manual [6])

- **Cloud-to-Mesh comparison (C2M):** the principle behind this method is close to the previous one, but it involves a triangular mesh as a reference model. A mesh-to-mesh comparison can also be performed and in this case the compared model would be treated as a point cloud considering the vertices of the triangles. The accuracy of the distance estimation, in the case, is strongly affected by the quality of the mesh, which is not easy to build for point clouds with significant roughness or missing data due to occlusion, as in this study.
- **Multiscale Model to Model Cloud Comparison (M3C2):** this method was proposed by Lague et al. [17] and the algorithm has been implemented in CloudCompare. The procedure is performed by two main steps:
 - I. surface normal estimation and orientation in a 3D environment accordingly to a scale set by the user and consistent with the local surface roughness;
 - II. mean distance computation between the point clouds along the normal direction with explicit calculation of local confidence interval; it is possible to detect both positive and negative values.

The authors of this method demonstrated its ability to handle complex 3D geometries (flat and vertical faces on the same scene) and to reduce the uncertainty caused by the local roughness of the model.

Since the evaluation of the accuracy of the described cloud-to-cloud comparison methods is not the purpose of this study, the decision was made considering previous comparative studies applied in geoscience fields. The same Lague et al. 2013 [17] showed that M3C2 algorithm is more robust to changes in point density and point cloud noise, differently from and C2C, and even if it could be accurate as C2M, it's the only one to allow a local confidence interval estimation; Nourbakhshbeidokhti et al. 2019 [25] tested these methods applied to topographic changes estimation in channel sedimentation and M3C2 revealed to be the most reliable to highlight the erosion and deposition rates from point cloud comparisons, considering also the fact that this method doesn't use interpolation which could lead to some errors, especially in complex terrain.

5.3.1. Description of M3C2 algorithm

The present methodology works directly on two point cloud: assuming that they correspond to consecutive surveys, the first one is called *reference point cloud* and the second one *compared point cloud*.

The first step is the calculation of surfaces normal in 3D using the reference point cloud, the compared point cloud or averaging the normal direction of both. Geomorphic processes, as rock instability, tend to depend on surface geometry so using the normals of the reference point cloud, when this is obtained by the first survey, is recommended. But, since the comparison results are more likely understandable when projected on the compared point cloud (coming from the following survey) and the projection of the results don't work properly in some portion of the point cloud, reference and compared point cloud were inverted and the normal were computed on the reference cloud. Must be notice that this process will lead at first to distances of opposite sign that would require a proper editing.

Normal vectors are computed for each point by fitting a plane to the neighbors that are within a radius of $D/2$ (Figure 5-3) and oriented accordingly to a preferred direction set by the user. The parameter D is the normal scale and it is defined by the user accordingly to the local roughness of the point cloud. In order to speed up the process without losing accuracy, the normal estimation can be computed on the core points, a sub-sampled version of the original point cloud: in this study the core points were subsampled with a minimum distance of 50 cm.

The second step is defining a cylinder of radius $d/2$, where d is the projection scale set by the user, along the normal direction for each core point. A maximum length of the cylinder is defined to speed up the process and a default value is given: in this particular case it was considered valid. The intercept of each point cloud with the cylinder defines two subsets of points, $n1$ and $n2$, which are then projected on the axis of the cylinder. Along this direction, considering the core point as the origin, a distribution of the distances is given and the its mean value for each point cloud, $i1$ and $i2$, represent an average position of the point clouds

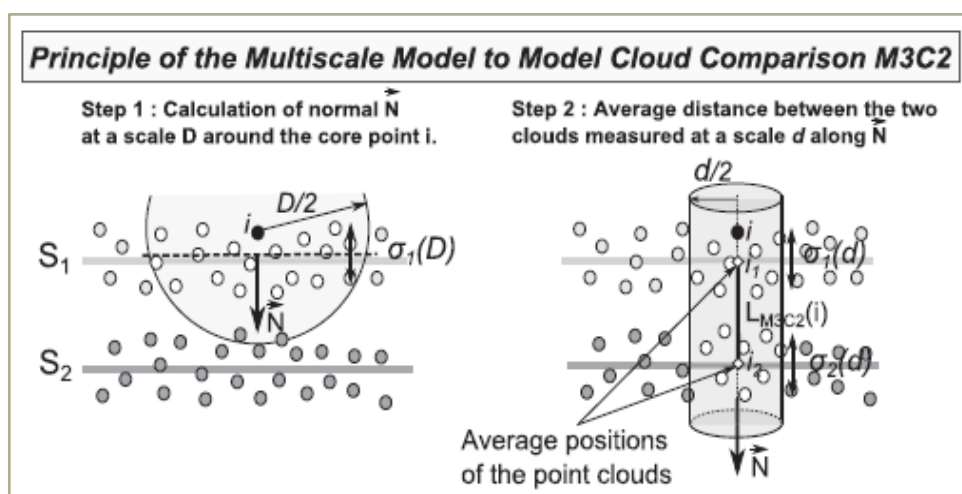


Figure 5-3 – Scheme of the main steps of the M3C2 algorithm. (Figure from Lague et al. [17])

along the normal direction. The standard deviation of those distances distribution gives a local estimation of the point cloud roughness, σ_1 and σ_2 , useful parameters to define the

local accuracy of the distance measurement. The computed distance, finally, is the difference between i_1 and i_2 (*Figure 5-3*).

5.3.2. Definition of confidence interval

A very useful characteristic of the M3C2 algorithm is the estimation of the local distance measurement accuracy, which allows to assess whether a detected change is statistically significant or not. The confidence interval or level of detection is defined at a prescribed confidence level of 95% and it is called $LOD_{95\%}$. This parameter is associated with each measurement so it is spatially variable and it allows to locally combine the different sources of uncertainties:

- position uncertainty of point clouds: this causes some noise in the point cloud and it depends on many factors as the technology adopted for the survey (Aerial Laser Scanner, Lidar, aerial photogrammetry), the distance and incidence angle of data acquisition and in some cases surface characteristics;
- registration uncertainty between the points clouds: the quality of the georeferencing process leads to systematic errors in the estimation of the coordinate systems of the two point clouds and it can be anisotropic and not spatially uniform;
- errors related to surface roughness: the occlusion of some portion of the model, frequently happening in complex terrains, the position uncertainties related to the technology adopted and the different position of the scanner/camera between the survey cause always different sampling of the same scene; this will lead to a systematically estimation of a small measurement, which should be addressed as non-statistically significant.

So, $LOD_{95\%}$ is analytically define as:

$$LOD_{95\%}(d) = \pm 1.96 \left(\sqrt{\frac{\sigma_1(d)^2}{n_1} + \frac{\sigma_2(d)^2}{n_2} + reg} \right) \quad (5.1)$$

where:

- n_1, n_2 : number of points of the two point clouds intercepted by the projection cylinder, for natural data this equation is valid as long as these parameters are >4 ;
- σ_1, σ_2 : standard deviations computed on the distance distribution along the normal direction of each core point;
- reg : registration error assumed isotropic and spatially uniform.

It must be notice that the confidence level is a function of the projection scale d , so this value it requires particular attention to be defined.

5.3.3. Definition of the normal orientation and the optimal normal scale

In complex rough surfaces, the value of the normal scale D strongly affects the normal orientation and consequently the possibility to detect an overestimated distance between the two point clouds. *Figure 5-4* shows how a normal scale (D_1) similar to the local roughness would detect very different normal directions, leading to an incorrect distance estimation; a larger normal scale (D_2) would be able to compute a more uniform normal orientation, ignoring the effect the surface roughness. Notice that where the roughness is particularly high and a large normal scale is adopted, the standard deviation ($\sigma_1(d)$) increases leading to a larger local confidence interval, meaning a less accurate distance estimation. On the other hand, in order to detect large scale changes in surface orientation and to observe the possible detachment or displacement of medium size blocks, the normal scale should not be too large.

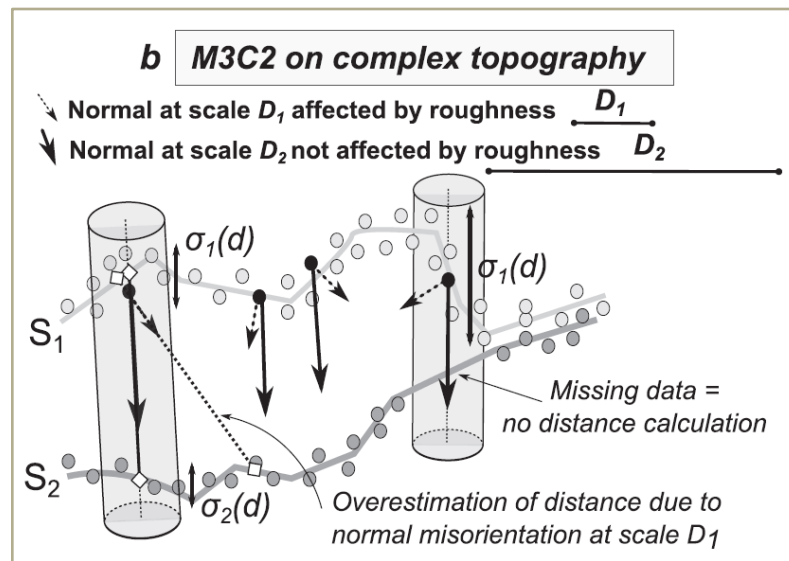


Figure 5-4 – Scheme of a complex topography and consequences of different normal scales in distance computation. (Figure from Lague et al. [17])

Under these circumstances, an optimal value of the normal scale D should be estimated. A simple and empirical solution would be defining a range of scales, for example from 0,5 m to 5 m with a 0,5 m step, and the local value of D would be the one ensuring a minimum of 10 points used in the normal estimation. This method would better adapt to the variety of geometries into the scenes, avoiding the definition of one constant normal scale that may overestimate the distance between the two point cloud or not-detect a significant change in surface orientation.

The only problem comes with a restriction inside the M3C2 plug-in: the normal orientation necessarily requires, in absence of the sensor position for the reference point cloud, the definition of a preferred orientation among a restricted list of options: $\pm X$, $\pm Y$, $\pm Z$, \pm Barycenter, $\pm (0,0,0)$. Since none of these options gave valid estimation normal orientation, the normals were computed by using the tools inside CloudCompare. The most useful feature was the possibility to adjust the orientation of the normals according to a Minimum Spanning Tree method, which required the definition of a maximum number of neighbors: greater values of kNN would have led to a more accurate normal orientation but it would require more memory and more time to process. For this reason, in most cases the default value of 6 was considered valid; where the results were not satisfactory, kNN was increased up to 50.

An explanatory comparison between the normals computed by the M3C2 algorithm, according to the preferred orientation +Z, and the ones computed by the CloudCompare tool and oriented with the Minimum Spanning method is showed in *Figure 5-5*.

However, this approach has its own limit: it allows to set only one value of the normal scale D . The best solution revealed to be testing different values, from 0,5m to 15 m, in order

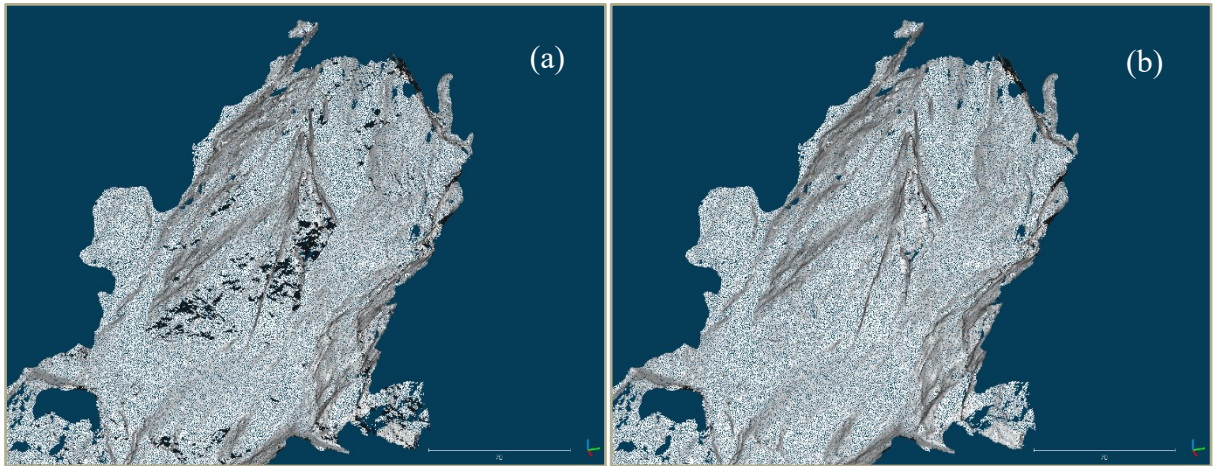


Figure 5-6 - Explanatory comparison between the normals computed by the M3C2 algorithm, according to the preferred orientation +Z (a), and the ones computed by the CloudCompare tool and oriented with the Minimum Spanning method (b), given a normal scale $D=1$ m.

to assess the proper surface roughness reconstruction. Greater values of the normal scale would have led to a smoother surface, lower values would have detected small details of the surface asperities. At the end, the best value in terms of processing time and proper surface roughness restitution was 1 m. An explanatory comparison with other values is showed in *Figure 5-6*.

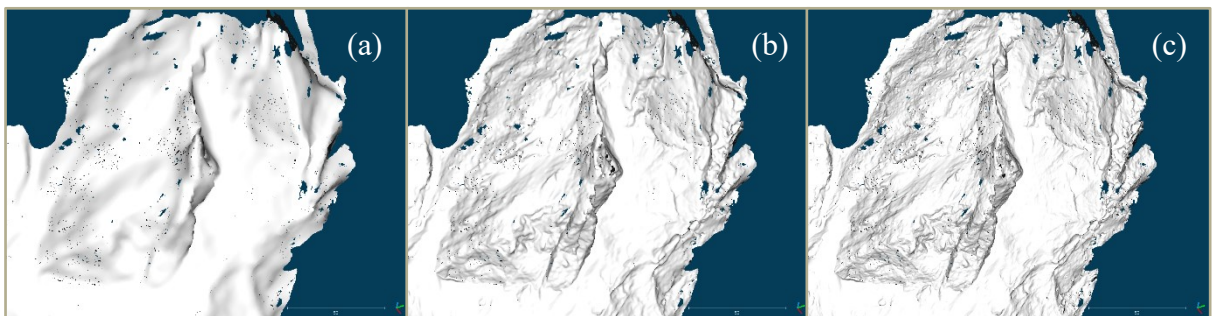


Figure 5-5 – Explanatory comparison between the normals computation with different scales: (a) $D=0,5$ m, (b) $D=1$ m, (c) $D=5$ m; the point cloud comes from D7 data set.

5.3.4. Definition of the optimal projection scale

The projection scale d is defined for each core points as the diameter of the cylinder which axis is collinear with the normal orientation and its length is defined with the purpose of intersecting both the reference and compared point cloud and to reduce the processing time. The value of d strongly affects both the spatial resolution of distance computation and the confidence interval: for greater values of the projection scale the spatial resolution of measurements decreases while the capacity of detecting statistically significant change increases. It follows that an optimal value of the projection scale must be found in order to properly detect the changes between the point clouds without losing any significant information.

The same authors of the M3C2 algorithm, Lague et al. [17], studied this question by observing the relationship between d and $LOD_{95\%}$ accordingly to different surface roughness (flat cliff, cobbles, debris) and different point density (subsampled versions at 1, 4, 5 and

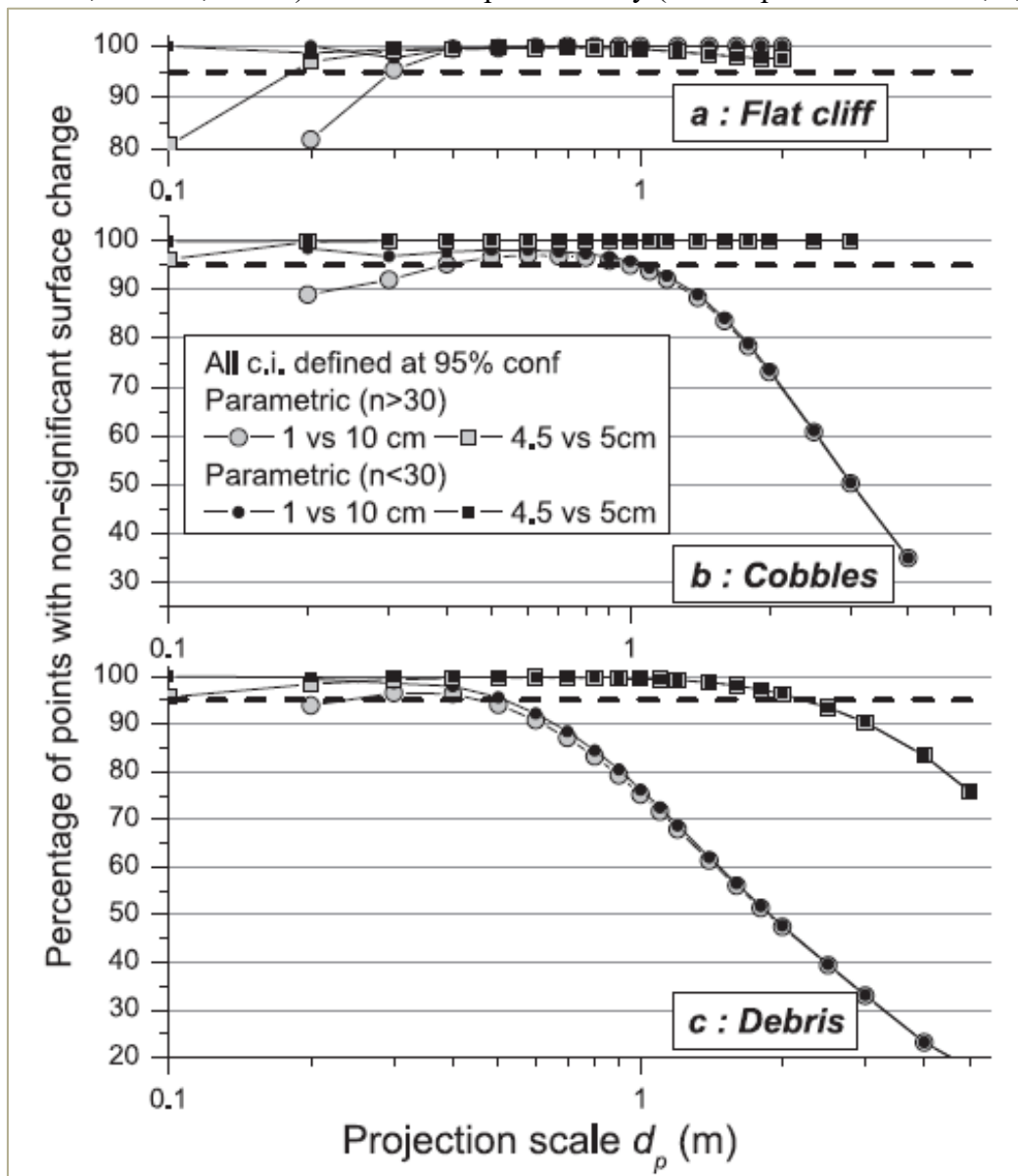


Figure 5-7 – Relationship between $LOD_{95\%}$ and d in different kind of terrain. (Figure from Lague et al [17])

10 cm). The proper estimation of level of detection, calculated with the equation (5.1) according to the conditions better defined in the cited article [13], has been tested by paring identical point clouds and results are shown in *Figure 5-7*.

This shows that for low values of d , 0,1-0,2 m, the estimated confidence interval in flat surfaces is too short and it leads to the detection of changes that should not be statistically significant. This happens for compared point clouds with both similar and different point density. In case of rough surfaces, as cobbles and debris, increasing d over the value of 1 m strongly increase the percentage of point detecting significant surface change. For point clouds with different point density, this happens with values greater than 0,5 m.

The point clouds object of this study presents the following features: their point cloud density is very similar since they all have been subsampled at 5 cm; they all present both flat and rough surfaces at different scales. In conclusion, the optimal projection scale must be found in a range that goes from 0,3 m and 2 m; three values, 0,5, 1 and 2 m, were tested and visually compared (*Figure 5-8*).

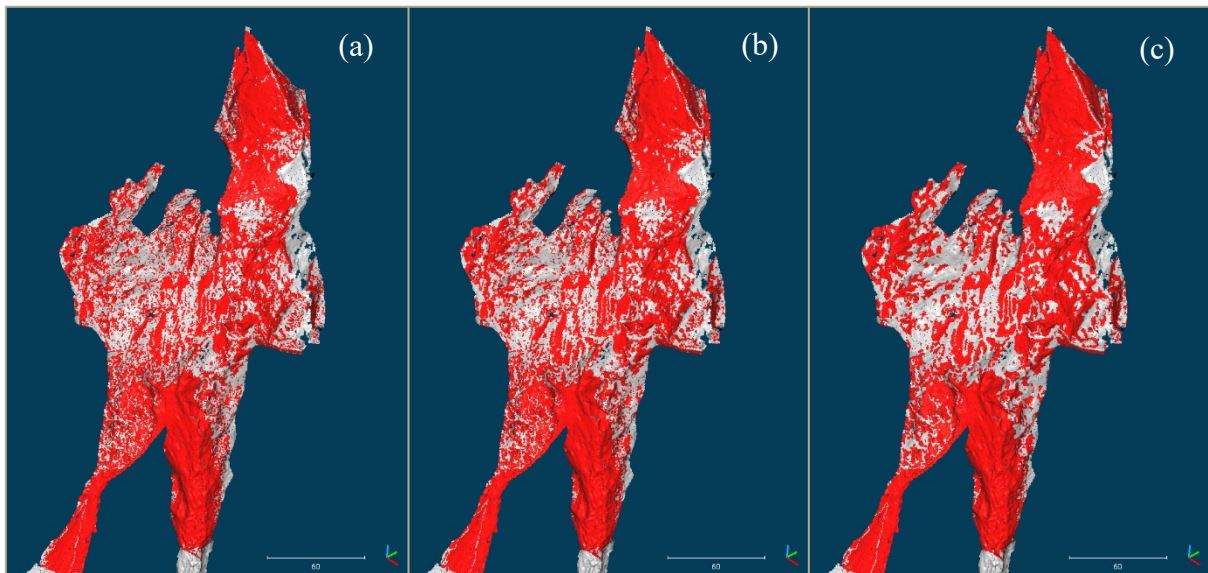


Figure 5-8 – Explanatory visual comparison between significant change detection according different values of projection scale: (a) $d=0,5$ m, (b) $d=1$ m, (c) $d=2$ m.

Increasing the parameter d would have detected more homogenous and wider areas with points detecting a significant change, but since the rock instability can be a small scale phenomenon rather than occur on large scales and considering the effort done so fare to not lose information about the surface roughness, the medium value of 1 m was chosen as the final solution.

5.3.5. Results of M3C2 distance estimation

The results of the comparison are shown in the following figures. They are associated to the reference point cloud, which is the most recent between the two. The first model D1 has been compared to the LiDAR data (*Figure 5-9*) coming from the Slovenian Environment Agency, *Agencija Republike Slovenije Za Okolje (ARSO)* [12]. Positive values of distance are indicated with warm colors (from yellow to red), negative values are indicated with cold colors (from green to blue). The shown distance uncertainty is the level of confidence in detecting the distance between the two point clouds.

The computed distances allow to observe how most of the loss of material occurs on rock mass and it deposits over the debris in the middle and the bottom of the slope, reaching also the riverbed along the valley.

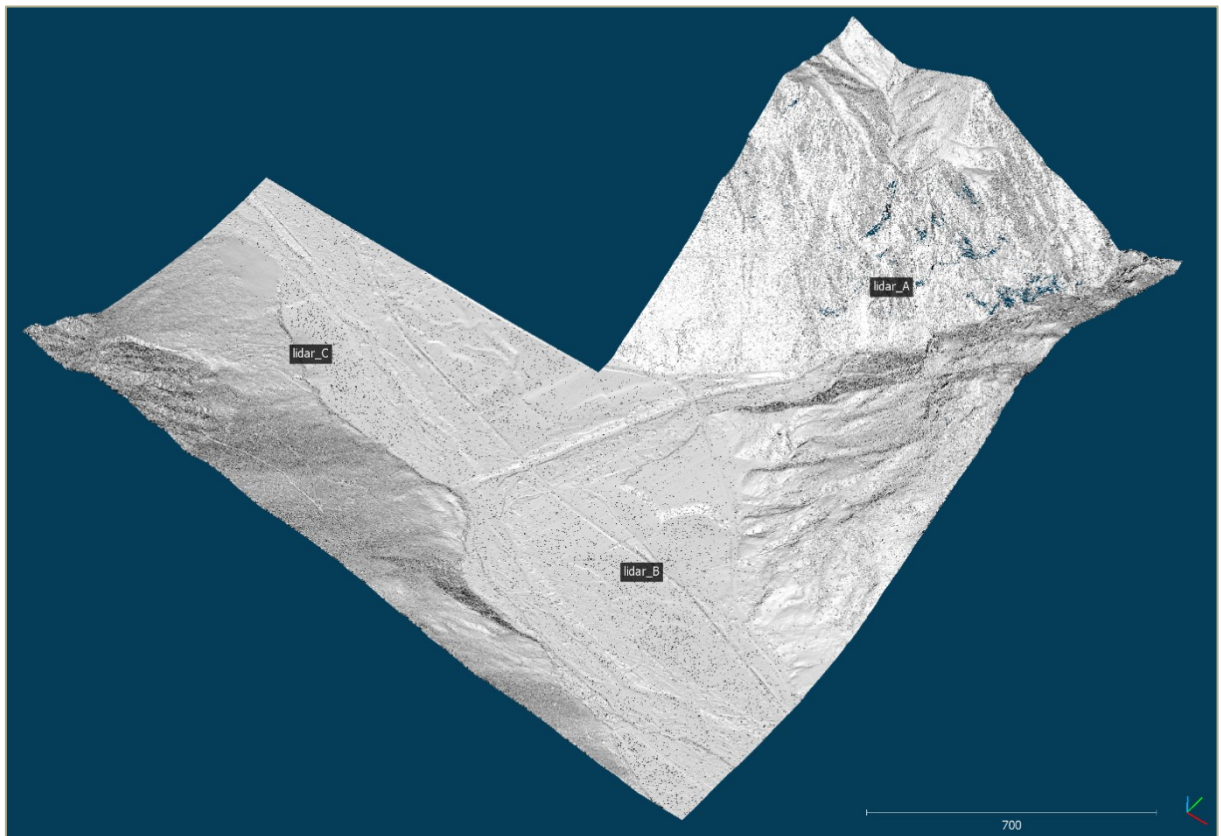


Figure 5-9 – LiDAR data from Slovenian geodatabase acquired in 2004; spatial resolution of 1 m.

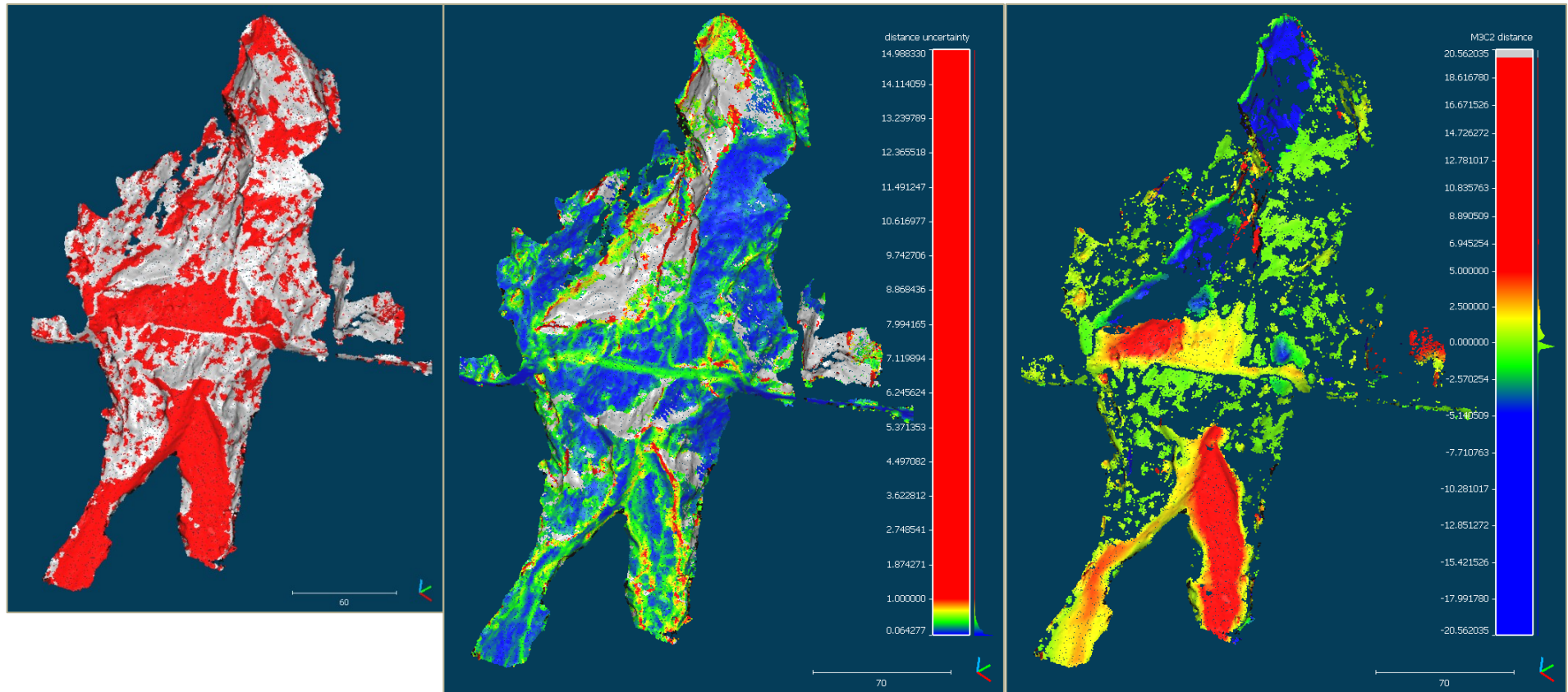


Figure 5-10 – Comparison of D1 with LiDAR data: (a) significant change, (b) distance uncertainty and (c) estimated distance.

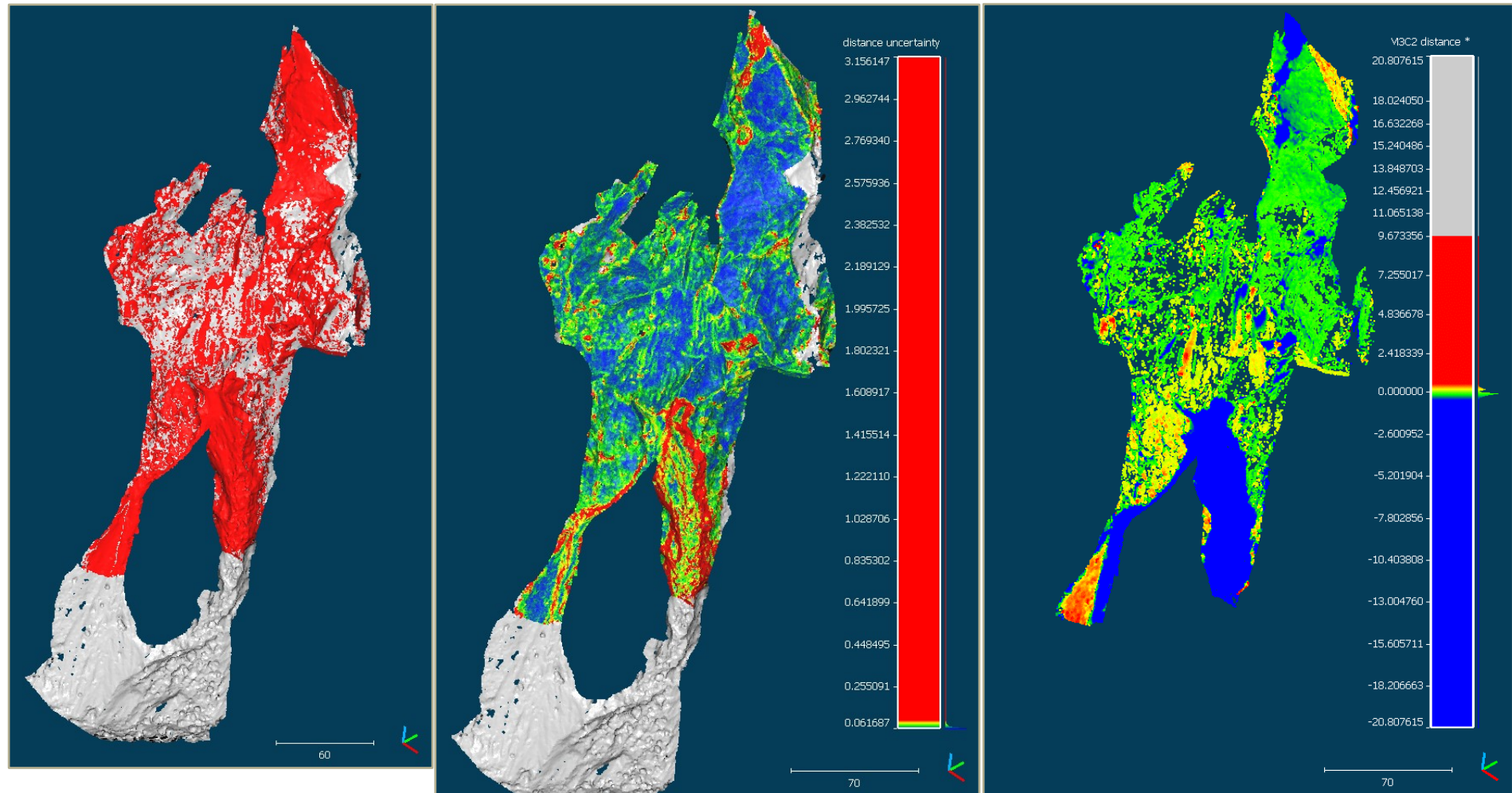


Figure 5-11 - Comparison of D2 with D1 data: (a) significant change, (b) distance uncertainty and (c) estimated distance.

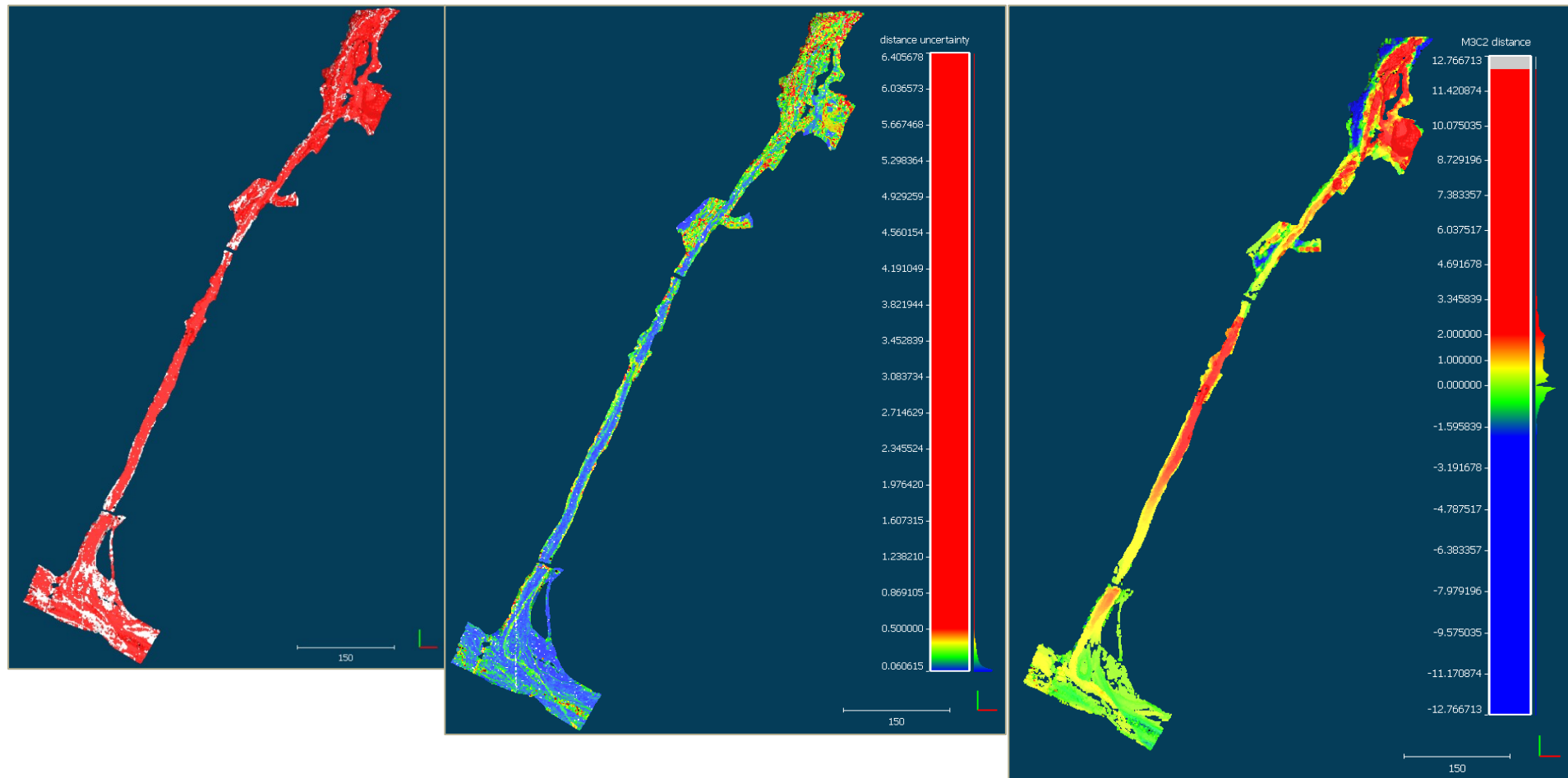


Figure 5-12 - Comparison of D2 with LiDAR data: (a) significant change, (b) distance uncertainty and (c) estimated distance.

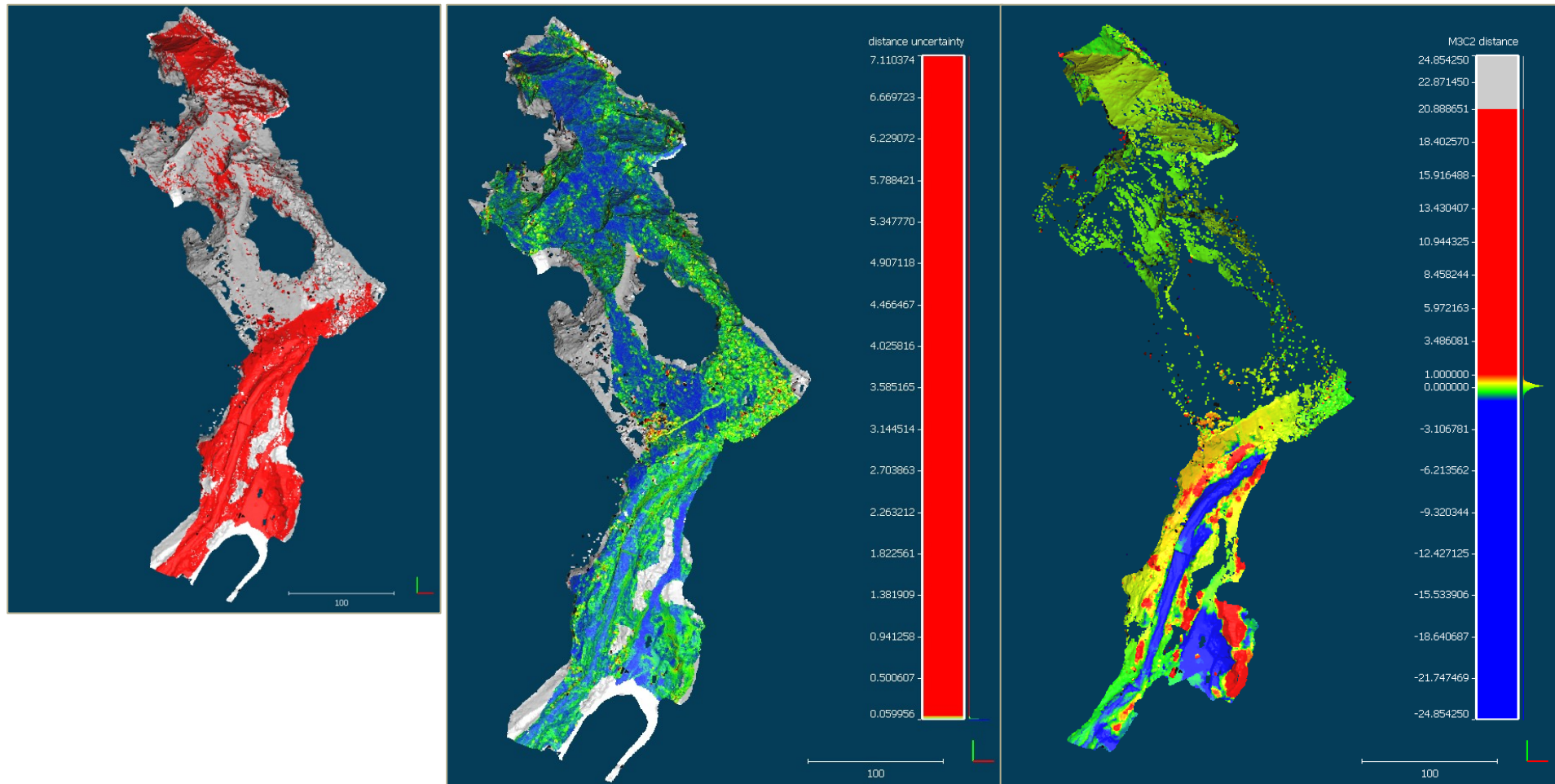


Figure 5-13 - Comparison of D3 with D2 data: (a) significant change, (b) distance uncertainty and (c) estimated distance.

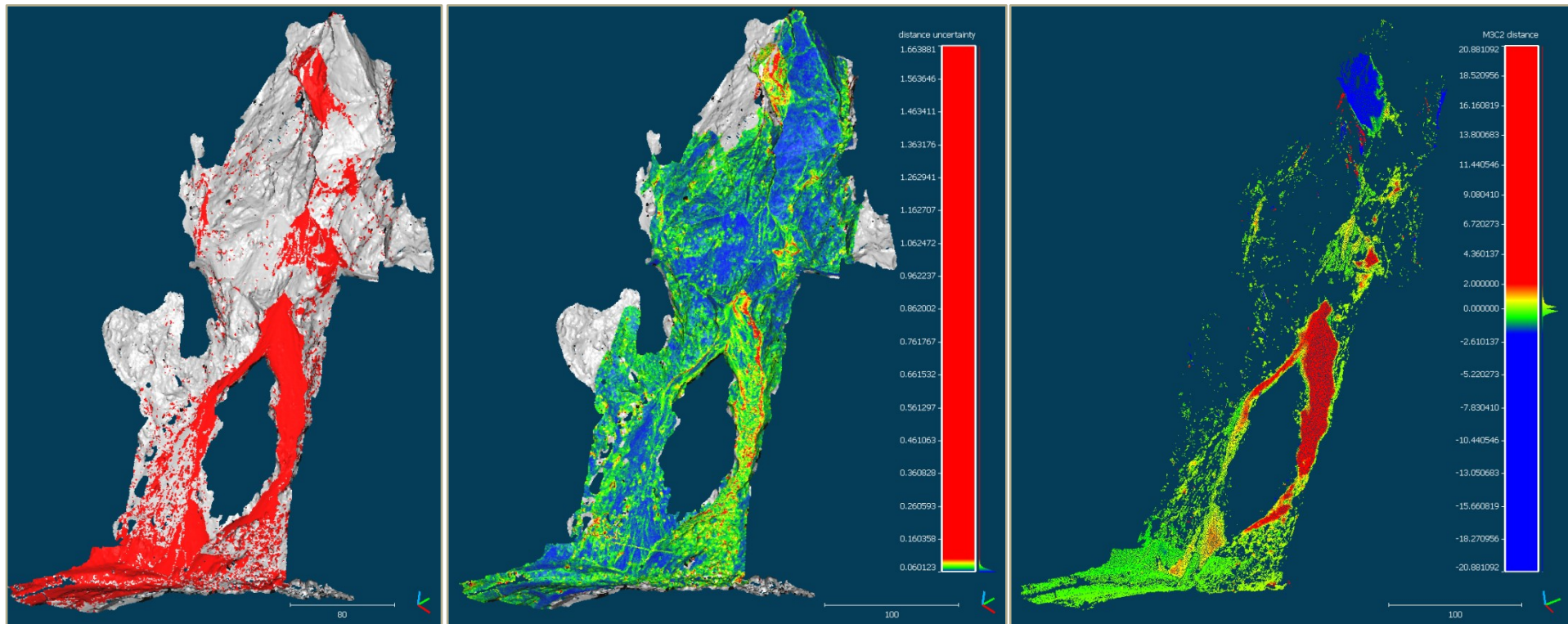


Figure 5-14 - Comparison of D4 with D3 data: (a) significant change, (b) distance uncertainty and (c) estimated distance.

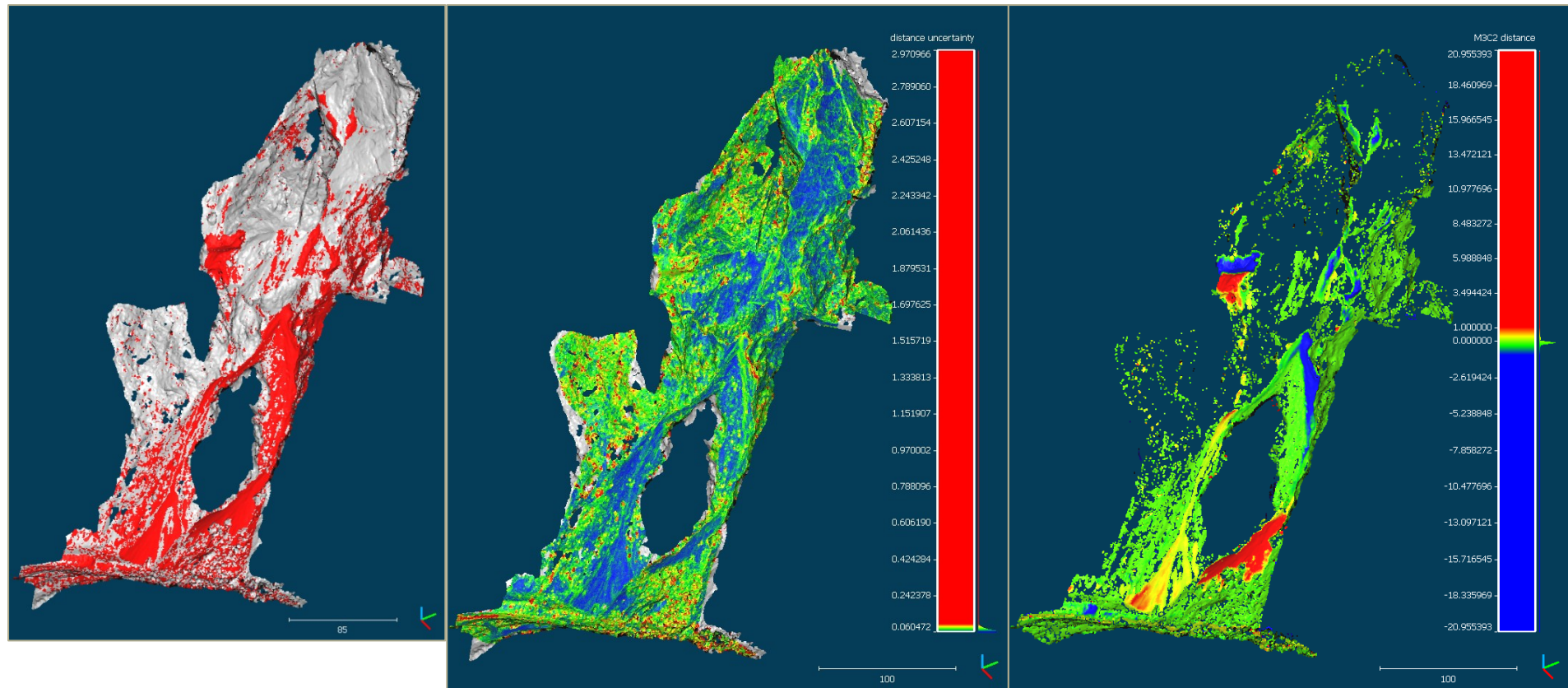


Figure 5-15 - Comparison of D5 with D4 data: (a) significant change, (b) distance uncertainty and (c) estimated distance.

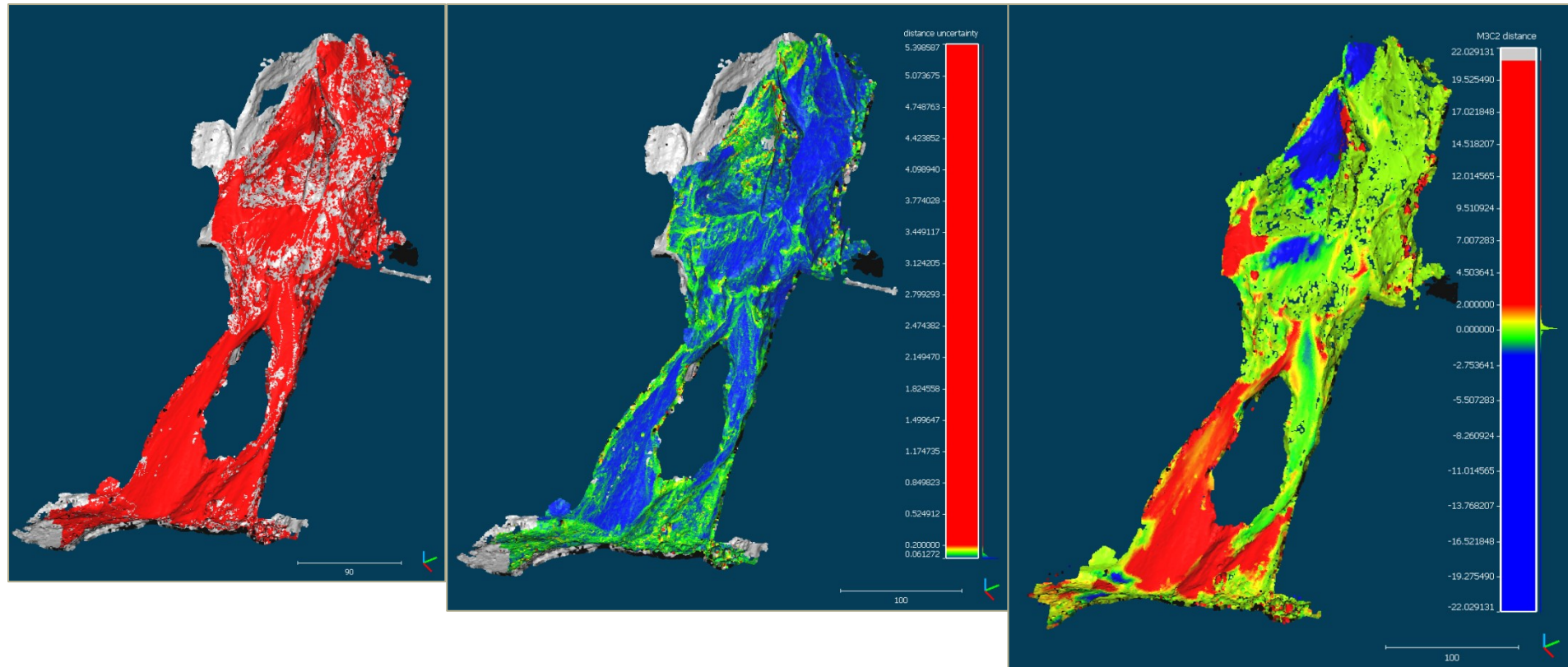


Figure 5-16 - Comparison of D6 with D5 data: (a) significant change, (b) distance uncertainty and (c) estimated distance.

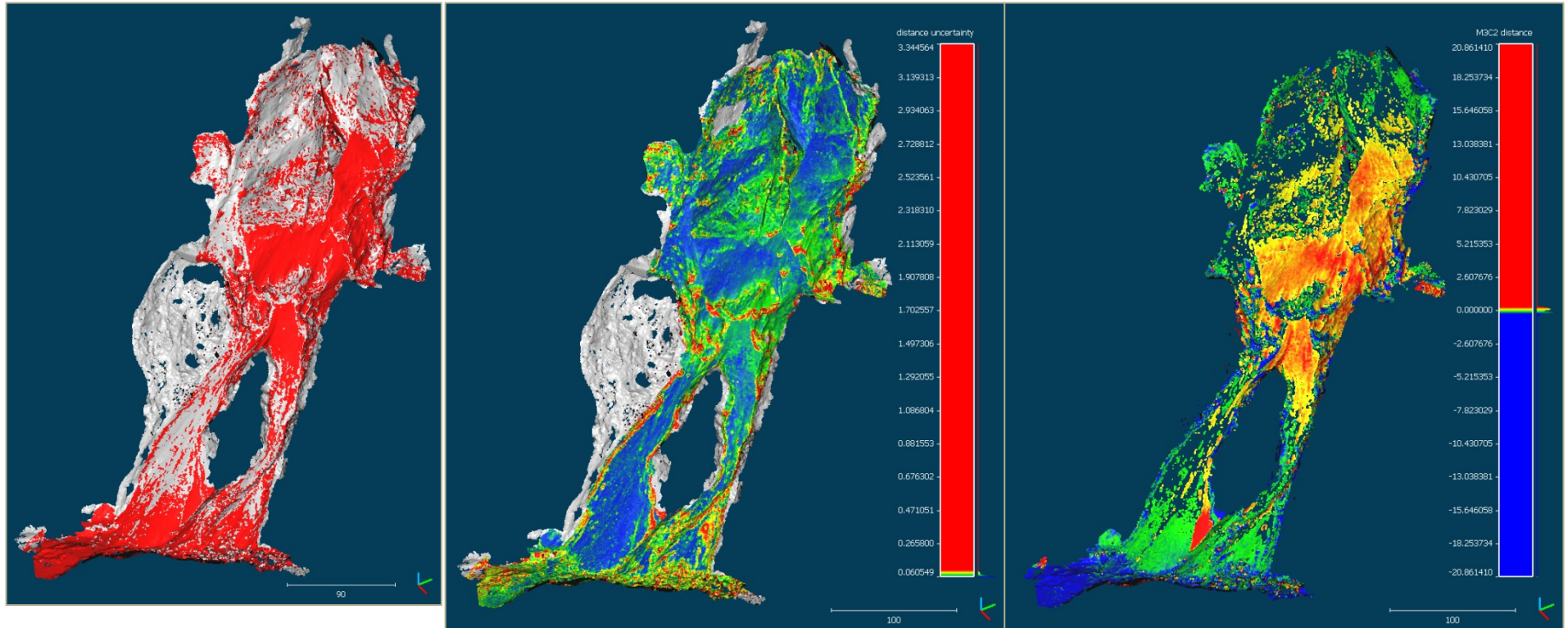


Figure 5-17 - Comparison of D7 with D6 data: (a) significant change, (b) distance uncertainty and (c) estimated distance.

5.4. Calculation of volume changes

In literature different approaches to detect topographic volume changes by comparison of two point cloud representing natural geomorphologies are adopted:

- Wheaton et al. [34] and William [35] applied the Difference of DEMs (DoD) method performed by comparing two horizontal grids in order to detect a vertical surface variation, a typical application of this method is the study of erosion and sedimentation in fluvial environments as riverbeds.
- Guinau et al. [15] estimated a difference between two point clouds which points were associated with a value of distance estimated thanks to the M3C2 algorithm. A triangular mesh was then constructed and for each triangle the area was computed and a height, according to the computed distances associated with the vertices, was assigned. By multiplying these parameters they obtained a volume for face of the triangular mesh. This particular method was adopted to observe volume changes in a natural rockslide and an artificially triggered rockfall.
- Stumpf et al. [30] combined the M3C2 distance computation with a grid comparison: the method is based on the application of a plane fitting algorithm among the points of defined clusters of the point cloud, allowing to adapt the orientation of the raster grid locally to the surface. An interpolation process is then performed to assign a distance measurement to each grid cell. The final volume is the sum of the volume associated to each cell, given by the area of the cell multiplied for the associated distance.

Unfortunately, none of these solutions were possible to apply. The DOD would have led to a great loss of information in a complex terrain where many vertical surfaces with different orientation are present, as also discussed by Lague et al. [17]. The last two methods could have been adopted, but both the step by step instructions and the software adopted were not given.

Finally, a research in other field of study revealed a simplified methodology based on the distance estimation by the M3C2 algorithm. Griffith and Thompson [14] studied the application of laser scanning in quantifying the abrasion level on water-submerged human bones and they proposed a simple analytical approach to apply on the raw data of the point cloud. Two different cases are distinguished, according to the projection scale and point density adopted in the distance estimation:

- a) when inside the projection cylinder there is only one point of the reference point cloud ($n_1=1$), the volume equation is

$$Vol = \sum_{i=1}^k [(A \cdot L_{M3C2,i}) \cdot N_{pts,i}] \quad (5.2)$$

where

- A is the base area of the cylinder;
- $L_{M3C2,i}$ is the median displacement value, defined for a range i of computed distances;

- $N_{pts, i}$ is the number of core points that display a L_{M3C2} inside the range i ;

So a volume is defined for every range of distances, and the final volume is obtained by summing the volume of all the k ranges.

- b) when inside the projection cylinder there are many points of the reference point cloud ($n1 > 1$), the volume equation is

$$Vol = \sum_{i=1}^k \left[(A \cdot L_{M3C2,i}) \cdot \frac{N_{pts,i}}{n1} \right] \quad (5.3)$$

Dividing for $n1$ the actual recurrence of a cylinder with a distinct volume is assessed.

A schematic illustration is proposed in *Figure 5-18*.

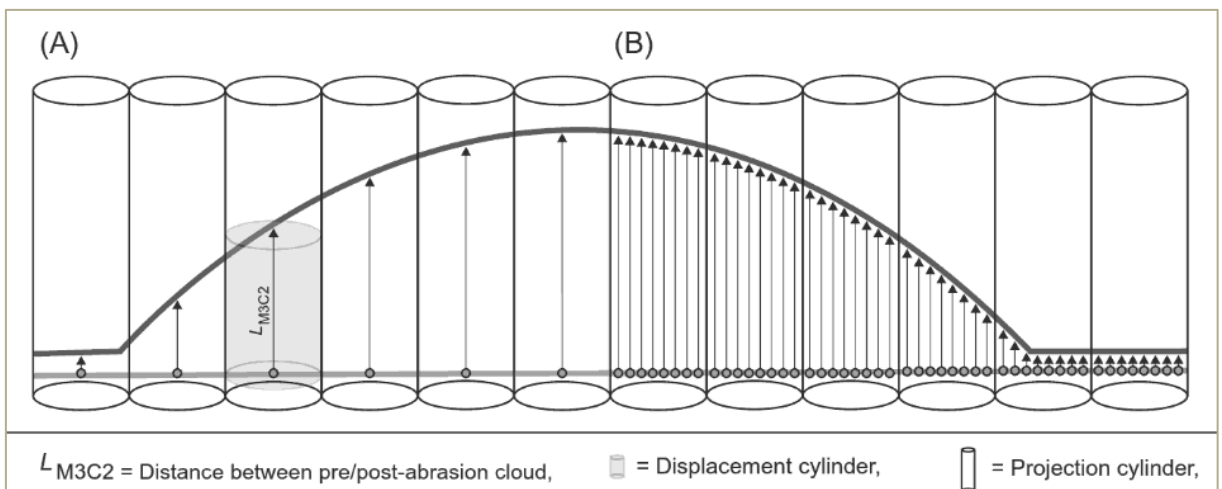


Figure 5-18 – Scheme of the principle behind the methodology adopted to estimate volume changes starting from M3C2 distances. (Figure from Griffith et al. [14])

An important condition of this method is that the cylinders must never cross each other; it follows that:

- I. given a point cloud made of only by the core point that display a L_{M3C2} , the cylinder base must be define by a diameter equal to the spacing between the points;
- II. considering the projection cylinder, so $A=f(d)$, the distance between the core points should be equal to d , forcing the resolution of the computation to adapt to the roughness of the surface and vice versa.

In both cases, the intersection between the cylinders is not totally avoided: these simplified methodology does not consider the surface roughness at any scale and the distances are computed along different directions accordingly to the previously computed normals. Another limit of this approach is not considering a planar distribution of points into the proposed scheme and thus in the final solution: considering a grid of equidistant points, tracing a circle around every point would not allow to cover the entire area leading finally to an underestimation of the actual volume change. It follows the final volume estimation comes with an unknown level of uncertainty.

Taking into account all the considerations made so far, a modified simplified approach has been adopted. Since the roughness of the surface and distance orientation have been already considered while running the M3C2 algorithm, it has been imagined taking all the core points with a significant change detection and giving them a planar distribution in order to have a grid of equidistant points. The value of d_p , point-to-point distance, is set as the maximum distance defined for subsampling the core points from the reference point cloud (50 cm) in order to reduce the incorrect estimation of the actual scene extension. To each point a volume, given by multiplying the area of a grid cell (given by the square of d_p) for the associated L_{M3C2} , has been assigned.

$$V_i = d_p^2 \cdot L_{M3C2,i} \quad (5.4)$$

The cumulative results (*Table 5-1*), for both positive and negative values, representing respectively an accumulation and a loss of volume, were then computed by running a script in Matlab (*Appendix C*) since an ASCII file of the point cloud was possible to export from CloudCompare.

	VOLUME (m ³)	
	Positive	Negative
D1	20'393	13'218
D2 SLOPE	522	19'746
D2 RIVER	27'570	7'162
D3	6'401	10'425
D4	12'338	13'953
D5	2'977	5'138
D6	30'524	19'554
D7	2'702	5'310

Table 5-1 – Cumulative results for volume change estimation from each comparison.

6. Results and discussion

UAV photogrammetry, combined with a Structure-from-Motion software as Agisoft Metashape, revealed to be a powerful tool to obtain a good 3D reconstruction of the scene. Multiple flights during the same photogrammetric survey, performed with different flying altitude and different camera's angle, allowed to reconstruct the complex geomorphology of the slope. The occlusion of some portions, due to the abundant presence of high vegetation or the abrupt variation of rock mass surface orientation was partially avoided. It has been also possible to accurately build the geomorphology of the rock mass in the upper part of the slope, avoiding occlusion of some portions that may occur using Aerial Laser Scanning (ALS) or Terrestrial Laser Scanning (TLS). The quality of the model reconstruction increased from survey to another: the complexity of the topography and the many natural limits of the site did not allow to design immediately the best methodology for the survey. Learning from previous experiences made possible to achieve better results each time.

In particular a workflow was designed in order to process the different available data sets.. The images have been aligned using SfM, obtaining a first sparse point cloud registered in a coordinates system based on the data acquired from the drones' internal GPS sensor. In order to perform reliable measurements, some ground control Points were introduced. The accessibility of the site and the instability of the overall slope had consequences on the amount and spatial distribution of GCPs into to scene. From 8 to 20 GCPs were used in different surveys; most of them were placed along the perimeter of the interested area, manly along the road that used to cross the middle portion of the slope and others into the forest among tree 2-3 meters long. Few were the cases in which some GCPs were inside the perimeter of the rock-mass or the debris deposit. Their purpose was performing a georeferencing independently from the position data coming with the drones, since they usually are affected by interferences or the absence of a good GPS signal. It follows that some of them were adopted as Ground Control Points (GCPs) to proper adjust the scale and the orientation of the models into the same datum, in particular the Slovenia Geodetic Datum 1996 (EPSG:3794), a necessary step to run a reliable comparison between consecutive point clouds. Few GCPs, from none to 5 in some cases, where removed due to errors in the position estimation, absence in the images or poor amount of good projection between the images. The georeferencing process is then assessed by defining the accuracy of the positioning measurements of each target: the survey methodology adopted by BF is unknown but an accuracy level of 1,5-3 cm was assigned to the data; FGG performed at first a RTK GNSS survey with an achieved accuracy of 4 cm in the horizontal direction and 8 cm in the vertical one and later a combination of tacheometry and GNSS was adopted achieving better results with an accuracy level of 2 cm in the horizontal direction and 4 cm in the vertical one. These values, verified with a simple comparison between GCP and CP (Check Points), have been assigned to each measurement since the data came with no explicit accuracy value.

Then, a cleaning of the sparse point cloud to increase the quality of the model reprojection and to optimize the cameras orientation, has been assessed and performed for each of the seven data set available. The maximum reprojection error in pixel has been reduced of the 80-90%, while the RMSE reprojection error has been reduced of the 30-40%.

The final results, adopting all the valid points as GCP, in terms of horizontal, vertical and

Count	X error (cm)	Y error (cm)	Z error (cm)	XY error (cm)	Total (cm)
7	1.76104	1.479	1.484	2.29972	2.73696
D1 Table 3. Control points RMSE. X - Easting, Y - Northing, Z - Altitude.					
Count	X error (cm)	Y error (cm)	Z error (cm)	XY error (cm)	Total (cm)
10	1.31771	1.43242	1.4393	1.94632	2.42069
D2 - River Table 3. Control points RMSE. X - Easting, Y - Northing, Z - Altitude.					
Count	X error (cm)	Y error (cm)	Z error (cm)	XY error (cm)	Total (cm)
9	0.948595	1.41099	1.47657	1.70022	2.25189
D4 Table 5. Control points RMSE. X - Easting, Y - Northing, Z - Altitude.					
Count	X error (cm)	Y error (cm)	Z error (cm)	XY error (cm)	Total (cm)
15	1.53087	1.96898	1.66486	2.49408	2.9987
D6 Table 3. Control points RMSE. X - Easting, Y - Northing, Z - Altitude.					
Count	X error (cm)	Y error (cm)	Z error (cm)	XY error (cm)	Total (cm)
4	1.0768	1.01503	2.05871	1.47979	2.53537
D2 - Slope Table 2. Control points RMSE. X - Easting, Y - Northing, Z - Altitude.					
Count	X error (cm)	Y error (cm)	Z error (cm)	XY error (cm)	Total (cm)
14	1.26785	0.761833	1.35621	1.47913	2.00677
D3 Table 2. Control points RMSE. X - Easting, Y - Northing, Z - Altitude.					
Count	X error (cm)	Y error (cm)	Z error (cm)	XY error (cm)	Total (cm)
9	2.10524	1.76008	2.81959	2.74407	3.93446
D5 Table 4. Control points RMSE. X - Easting, Y - Northing, Z - Altitude.					
Count	X error (cm)	Y error (cm)	Z error (cm)	XY error (cm)	Total (cm)
8	1.65387	2.52725	2.0677	3.02031	3.66028
D7 Table 4. Control points RMSE. X - Easting, Y - Northing, Z - Altitude.					

Figure 6-1 – Horizontal, vertical and total RMS reprojection error averaged over all the GCPs.

total error are shown in *Figure 6-1*: the achieved accuracy of the reprojection is between 2 and 4 cm.

At this stage, the building of the dense point cloud was possible and a combination of automatic and manual classification of point clouds were carried out to obtain the point cloud consisting only of points classified as ground points for each survey. Each point cloud was then imported into CloudCompare: a noise filtering has been performed by removing the double points closer than 1 cm, subsampling the point cloud with a maximum distance of 5 cm and adopting the S.O.R. filter with a value of 100 for kNN and 1 of nSigma. In order to obtain reliable comparisons, the point clouds have been registered by applying in some occasions a rigid vertical translation of a distance depicted by a manual point-to-point distance inspection; in some other cases the automatic reprojection of the points in the CloudCompare environment was good enough to guarantee a good overlap of the models.

The 3D distance between the compared point clouds has been estimated by running the M3C2 algorithm, which required in this case a previous estimation of the normals orientation by setting a diameter for the calculation of the best fitting plane of 1 m and adopting the Minimum Spanning Tree method to adjust the orientation. Calculating the distances, the projection scale d was set equal to 1 m and the registration error was set equal to 3 cm. The results allow to emphasize the niches where the detachment occurred, mainly along the vertical wall the rock mass in the left upper part of the slope (as shown in *Figure 5-10* and *5-16* by comparing D1 with LiDAR and D6 with D5), with particular occurrence at the top (as shown in *Figure 5-11* and *5-14* by comparing D2 with D1 and D4 with D3). The loss of material occurs even on the debris deposit, as shown in *Figure 5-15* and *5-16* by comparing D5 with D4 and D6 with D5: this is not unusual since instabilities,

triggered by the impact of a block or rainfall, can occur inside debris deposit causing a debris flow towards the valley. It is possible also to recognize the areas where the material accumulated causing an increase of volume in the debris deposits, both across the middle portion of the slope (as shown in *Figure 5-10, 5-15 and 5-17* by comparing D1 with LiDAR, D5 with D4 and D7 with D6) and along the bottom part, affecting mainly the right side (as shown in *Figure 5-10, 5-11, and 5-14* by comparing D1 with LiDAR, D2 with D1 and D4 with D3). Many changes are also observed along the riverbed and on the riverbanks, where mining activities cause the removal and stocking of natural material. The presence of relatively small distances, lower than 1 m, between two point clouds coming from consecutive surveys detects a smaller scale evolution well distributed all over the entire slope.

Such estimations come with a level of detection, which in most cases is globally lower than 10 cm. In the portions of the slope where the surface orientation is more consistent, a confidence interval close to the registration error occurs. Greater values of LOD95% are mainly caused by a poor reconstruction of the reference and/or compared point cloud or can be the consequence of a local increase of the surface roughness.

Finally, a simplified method is assessed and adopted to estimate volume changes. Positive values indicate an accumulation of material, negative values indicate a loss of volume mainly due to the detachment that describe the evolution of the rock mass. In most cases, the results are very different. The most frequent scenario is a negative volume bigger than the positive one: this can be justified considering the possibility that most of the detached material could have felt out of the scene captured during the survey, accumulating among the vegetated areas in left bottom portion of the slope or even reaching farther points of the riverbed. A falling block could also be divided into smaller debris due to the impacts with the surface, so that the material could spread in different directions reducing the actual surface change that can be confidently detected. Finally, the presence of a mining activity in the valley and secondary instability phenomena triggered by natural events cannot be ignored: the final balance can be affected by both human activities and natural causes. Others scenarios, where the positive volume is bigger than the negative one can be justified more likely in the same way: the detachment occurred in a portion out of the scene or where the model was not reconstructed due to the presence of vegetation or small and distributed erosion of the rock mass, lower than the level of detection, led to the accumulation of material in the bottom debris deposit. Combining the results of both the slope and river model in case of the second data set D2, a relatively small difference (about 1'000 m³) between the accumulated and the detached material is shown: this indicates that a portion of the material reached the valley and some of this have been transported by the Belca torrent towards the main Sava river.

7. Conclusion

A general Structure-from-Motion based workflow has been defined to assess a good 3D reconstruction of the scene considering all the challenges: different surveying methods adopted from a data set to another, the abundant presence of high vegetation and the reduced amount and non-uniform distribution of targets in the scene to use as GCP and/or CP. A methodology for surface and volume detection by meaning point cloud comparison has been defined without requiring any interpolation by gridding or mesh triangulation. In particular a Multiscale Model to Model Cloud Comparison (M3C2) was performed and the optimal values for the main parameters for each point cloud were assessed; the distance computation comes also with a spatial variable and local level of uncertainty, accounting for errors in the registration and uncertainties related to the surface roughness. Also, a rough but simple volume detection methodology has been performed.

The final results show a qualitative and quantitative evolution of the slope: the main areas where the detachment and accumulation of rock blocks occurs are detected, and an evolution of the material in the riverbed, especially in the upper part, is reported.

This experience highlights the fact that even if the photogrammetric elaboration could have a high level of automatization, the judgment of the user is required when reconstructing a complex geomorphology. SfM software are very useful since they provide a user-friendly low cost technique when a scene or even an object need to be reconstructed in a 3D virtual environment, starting simply from multiple overlapping images taken from different points of view. This kind of raw data can be easily acquired nowadays with common instruments as smartphones and tablets. Vast areas can be investigated by UAV, nowadays accessible to everybody in terms of economic expense, portability and level of automatization during the flight. The data processing become more challenging when an indirect georeferencing using GCPs is required and the final reprojection error must be minimized: the experience and the knowledge of the user area the key elements to obtain the best result possible, because in most cases an inspection of the images is needed to assess the projection of the markers and their right positioning into the images could require an iterative process. Also the ground point classification may need a manual intervention: considering the limited results returned from many different algorithms, they are able to classify the points relying only on the geometry of the point cloud. There are even algorithms as CANUPO¹ that can be trained by manually assigning some portion of the scene to a defined class, but even in this case the experience of the user is the key element to better train the classifier and reach a good result in obtaining the needed ground point cloud.

In natural hazard estimation, the photogrammetric process can be a powerful source for geometric considerations and stability analysis. Indirect geomechanical surveys can be carried out on the rock mass in order to assess the spatial distribution of the joint sets and potentially estimate the size of the block more likely to collapse. A closer investigation of the

¹ Brodu n., Lague D. *3D Terrestrial lidar data classification of complex natural scenes using a multiscale dimensionality criterion: applications in geomorphology*, ISPRS Journal of Photogrammetry and Remote Sensing, Elsevier, 2012, 68, pp.121-134.

debris deposit could allow the estimation of the sediment granulometry to evaluate the internal stability.

The comparison with other kind of data it could also help in the reconstruction of the entire natural phenomenon. Here the areas most susceptible to detachment and accumulation, observed in a short period of time, almost 1 year if excluding the LiDAR data coming from the 2014, are shown but more can be done: a correlation with external factors as rainfalls or mining activities could eventually highlight possible triggering factors of instability.

In the end, many things can be accomplished by combining UAV photogrammetry and SfM software. They provide a low-cost, rapid and flexible alternative to other methodologies for accurate geomorphological mapping.

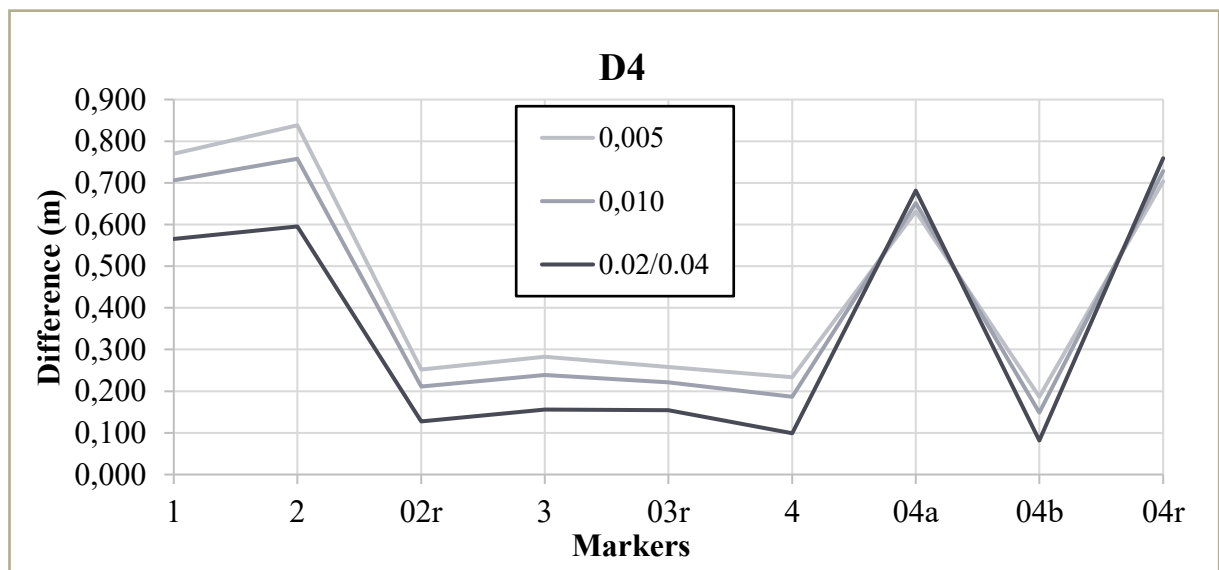
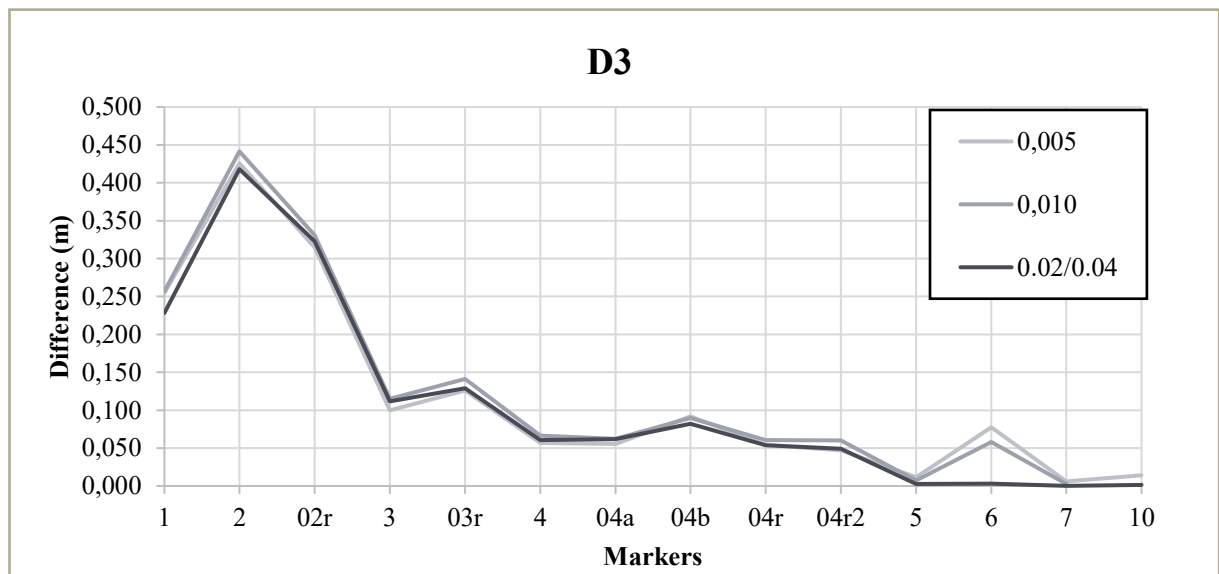
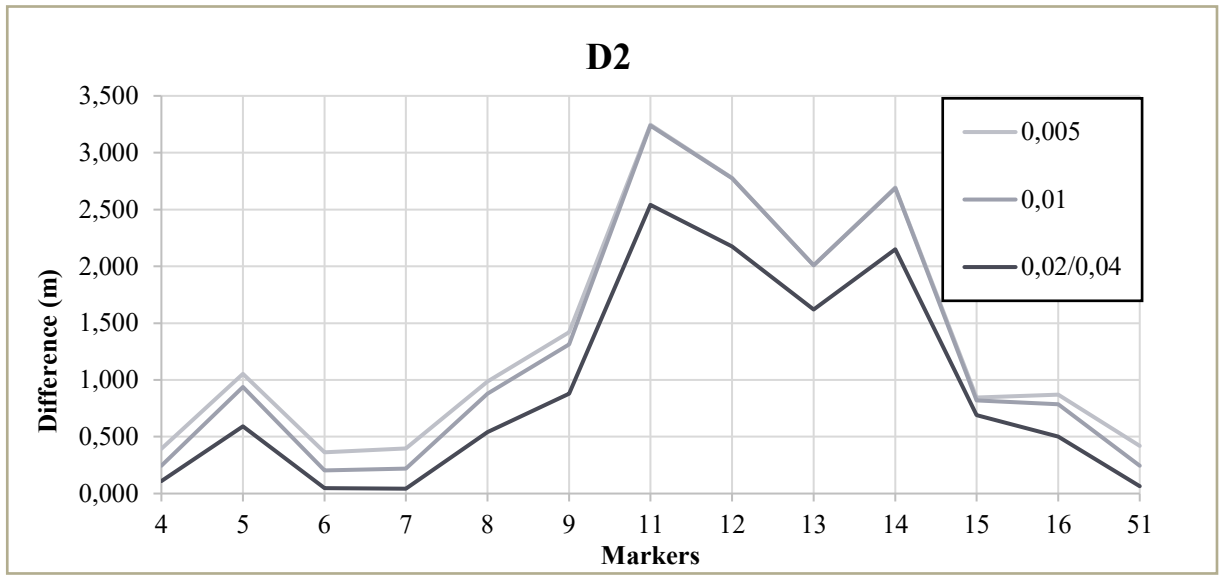
Reference List

- [1] Agisoft Forum, Topic: Investigating Alignment Parameters (<https://www.agisoft.com/forum/index.php?topic=8074.msg38949#msg38949>)
- [2] Agisoft Metashape User Manual Professional Edition, Version 1.5
- [3] Bemis S.P., Micklerwaite S., Turner D., James M.R., Akeiz S., Thiele S.T., Bangash H.A., *Ground-based and UAV-based photogrammetry: a multi scale, high resolution mapping tool for structural geology and paleoseismology*. J. Struct. Geol. 69 (A), 163-178
- [4] Benassi, F.; Dall'Asta, E.; Diotri, F.; Forlani, G.; Morra di Cella, U.; Roncella, R.; Santise, M. Testing Accuracy and Repeatability of UAV Blocks Oriented with GNSS-Supported Aerial Triangulation. Remote Sensing 2017, 9, 172, doi: 10.3390/rs9020172.
- [5] Bitelli G., Dubbini M., Zanutta A. *Terrestrial laser scanning and digital photogrammetry techniques to monitor landslide bodies*. Int. Arch. Photogramm. Remote Sens. Spat. Inf. Sci. 2004, 35, 246–251.
- [6] Boccardo P., *Introduzione*, Corso di Telerilevamento, Politecnico di Torino
- [7] Boccardo P., *Telerilevamento*, GEOMATICA. Le frontiere della Ricerca, AUTECS, Pavia 2004
- [8] Cannarozzo R., Cucchiari L., Meschieri W., *Misure, rilievo, progetto per Costruzioni, ambiente e territorio - Volumi 1, 2, 3*; Quinta edizione – 2017
- [9] CloudCompare version 2.6.1 – User manual
- [10] Corradeghini P., *Pulire una nuvola di punti da rumore, sporco e punti doppi*, October 26th, 2019 (<https://3dmetrica.it/pulizia-nuvola-di-punti/>)
- [11] Egle B., *Produzione di cartografia tecnica in ambito comunale mediante l'utilizzo di droni. Il caso del Comune di Mappano*. Politecnico di Torino, 2019
- [12] Geodatabase of Slovenian Environment Agency (http://gis.arso.gov.si/evode/profile.aspx?id=atlas_voda_Lidar@Arso)
- [13] GIS Resources (www.gisresources.com), *Introduction to Photogrammetry*
- [14] Griffith S.J., Thompson C.E.L., *The Use of Laser Scanning for Visualization and Quantification of Abrasion on Water-Submerged Bone*, University of Southampton, United Kingdom (Chapter 8 of Erickson D., Thompson T., *Human Remains: Another Dimension – The Application of Imaging to the Study of Human Remains*, Academic Press: An imprint of Elsevier, 2017)
- [15] Guinau M., Tapia M., Pérez-Guillén C., Suriñach E., Roig P., Khazaradze G., Torné M., Jesús Royán M., Echeverría A., *Remote sensing and seismic data integration for the characterization of a rock slide and an artificially triggered rock fall*, Eng. Geol., 257 (2019), Article 105113, 10.1016/j.enggeo.2019.04.010

- [16] Johnson, K.; Nissen, E.; Saripalli, S.; Arrowsmith, J.R.; McGarey, P.; Scharer, K.; Williams, P.; Blisniuk, K. *Rapid mapping of ultrafine fault zone topography with structure from motion*. *Geosphere* 2014, 10, 969–986
- [17] Lague D., Brodu N., Leroux J., *Accurate 3D comparison of complex topography with terrestrial laser scanner: Application to the Rangitikei canyon (N-Z)*, *ISPRS Journal of Photogrammetry and Remote Sensing*, 2012
- [18] Lazar A., Begus T., Vulic M., *Monitoring of the Belca rockfall* *Acta Geotechnica Slovenica*, 2018/2 p. 2-15
- [19] Lipman A., *5 Industrial Photogrammetry Applications*, August 21th, 2018 (<https://industrytoday.com/5-industrial-photogrammetry-applications/>)
- [20] Mallison H., *Photogrammetry tutorial 11: How to handle a project in Agisoft Photoscan*, October 11th, 2015 (<https://dinosaurpalaeo.wordpress.com/2015/10/11/photogrammetry-tutorial-11-how-to-handle-a-project-in-agisoft-photoscan/>)
- [21] Meza J., Marrugo A., Ospina G., Guerrero M. and Romero L., *A Structure-from-Motion Pipeline for Generating Digital Elevation Models for Surface-Runoff Analysis*, *Journal of Physics: Conference Series*, Volume 1247, 6th National Conference on Engineering Physics and the 1st International Conference on Applied Physics Engineering & Innovation 22–26 October 2018, Bucaramanga, Colombia
- [22] Micheletti N., Chandler J.H., Lane S.N., (2015) Section 2.2. *Structure from Motion (SfM) photogrammetry*. In: Cook, SJ, Clarke, LE, Nield, JM (eds) *Geomorphological Techniques* (Online Edition). London, UK: British Society for Geomorphology. ISSN: 2047-0371
- [23] Niethammer U., James M., Rothmund S., Travelletti J., Joswig M., *Uav-based remote sensing of the super-sauze landslide: Evaluation and results*, *Eng. Geol.* 128 (2012) 2–11.
- [24] Nissen E., Arrowsmith J.R., Crosby C., *Introduction to Structure-from-Motion*, Geological Society of America, 2017
- [25] Nourbakhshbeidokhti S., Kinoshita A.M., Chin A., Florsheim J.L., *A Workflow to Estimate Topographic and Volumetric Changes and Errors in Channel Sedimentation after Disturbance*. *Remote Sens.* 2019, 11, 586.
- [26] Oppikofer T., Jaboyedoff M., Blikra L, Derron M.H., Metzger R., 2009. *Characterization and monitoring of the Åknes rockslide using terrestrial laser scanning*. *Natural Hazards and Earth Systems Science*, 9: 1003-1019. DOI: 10.5194/nhess-9-1003-2009
- [27] Piras M., Taddia G., Forno M.G., Gattiglio M., Aicardi I., Dabove P., Lo Russo S., Lingua A., (2017) *Detailed geological mapping in mountain areas using an unmanned aerial vehicle: application to the Rodoretto Valley, NW Italian Alps*, *Geomatics, Natural Hazards and Risk*, 8:1, 137-149, DOI: 10.1080/19475705.2016.1225228

- [28] Shenk T., *Introduction to photogrammetry*, Department of Civil and Environmental Engineering and Geodetic Science, The Ohio State University, 2005
- [29] Sithole G., Vosselman G., 2004. *Experimental comparison of filter algorithm for bare-Earth extraction from airborne laser scanning point clouds*. ISPRS J. Photogramm. 59, 85-101
- [30] Stumpf A., Malet J.P., Allemand P., Pierrot-Deseilligny M., Skupinski G. *Ground-based multi-view photogrammetry for the monitoring of landslide deformation and erosion*, Geomorphology, 2014
- [31] Tarolli P. (2014) *High-resolution topography for understanding Earth surface processes: opportunities and challenges*. Geomorphology 216:295–312
- [32] *Unmanned Aircraft Systems Data Post-Processing*, USGS National UAS Project Office – March 2016
- [33] Westoby M.J., Brasington J., Glasser N.F., Hambrey M.J., Reynolds J.M., 2012. *'Structure-from-Motion' photogrammetry: a low-cost, effective tool for geoscience applications*. Geomorphology 179, 300–314
- [34] Wheaton J.M., Brasington J., Darby S.E., Sear D.A., 2010. *Accounting for uncertainty in DEMs from repeat topographic surveys: improved sediment budgets*. Earth Surf. Process. Landf. 35 (2), 136–156.
- [35] Williams R.D. (2012). *DEMs of difference* In: L. E. Clarke, & J. M. Nield (Eds.), *Geomorphological Techniques* (Online Edition). London, UK: British Society for Geomorphology
- [36] Zhang W., Qi J., Wan P., Wang H., Xie D., Wang X., Yan G., 2016. *An Easy-to-Use Airborne LiDAR Data Filtering Method Based on Cloth Simulation*, MDPI Remote Sensing Journal 2016, 8, 501

APPENDIX A



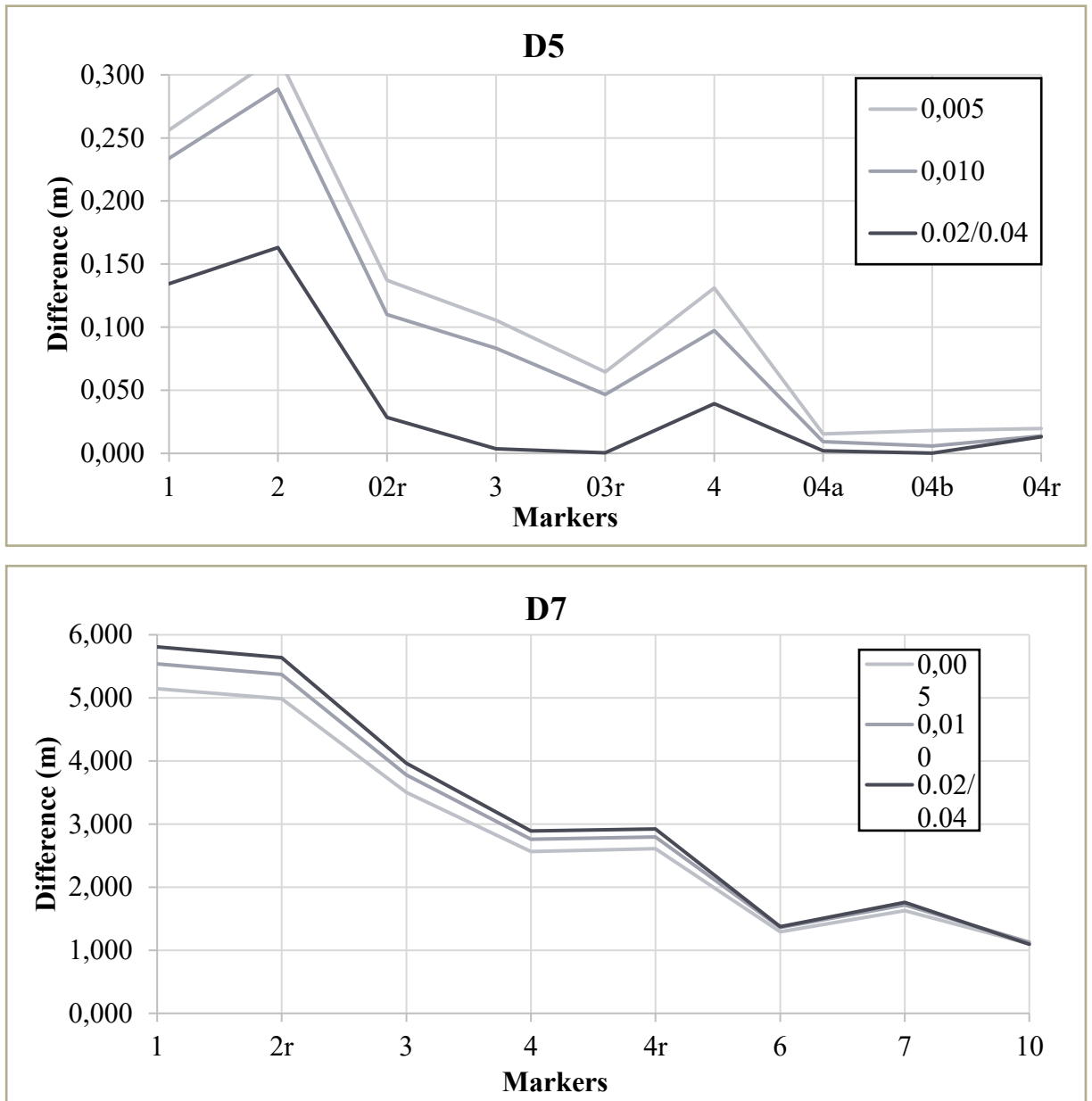


Figure A.1 - Distribution of the difference between the reprojection error of each marker considered as GCP and then as CP, after optimizing the camera parameters.

APPENDIX B

Label	X error (cm)	Y error (cm)	Z error (cm)	Total (cm)	Image (pix)
01	-2.44836	-0.933431	0.684505	2.70819	0.680 (18)
02	-0.395192	-0.0201638	-3.02983	3.05556	0.417 (10)
03	0.41839	-3.54149	-1.48597	3.86333	0.558 (6)
04	1.7069	-0.295886	0.0683021	1.73371	0.579 (6)
07	3.01794	1.14776	-1.20716	3.44711	0.572 (15)
09	-1.53325	0.117185	1.06068	1.86806	0.376 (2)
10	-1.00541	0.692526	0.986055	1.56931	0.571 (14)
Total	1.76104	1.479	1.484	2.73696	0.578

Table 4. Control points.
X - Easting, Y - Northing, Z - Altitude.

Label	X error (cm)	Y error (cm)	Z error (cm)	Total (cm)	Image (pix)
06	-0.0611197	1.52656	-0.758588	1.70575	0.210 (3)
05	-0.19595	-2.63586	0.915454	2.79718	0.189 (8)
08	-1.69301	0.703668	3.07044	3.57617	0.227 (8)
09	2.37077	-1.08366	-1.89396	3.2221	0.315 (12)
16	-1.14056	1.83297	-1.29549	2.51773	0.261 (6)
15	0.839619	-1.05988	-0.488711	1.43776	0.222 (8)
13	0.954765	1.21967	0.335185	1.58478	0.388 (8)
12	-1.28747	-1.65205	-1.28624	2.4579	0.470 (12)
11	1.56197	0.899116	1.60123	2.41083	0.310 (9)
14	-1.34901	0.249468	-0.199309	1.38628	0.210 (5)
Total	1.31771	1.43242	1.4393	2.42069	0.313

Table 4. Control points.
X - Easting, Y - Northing, Z - Altitude.

Label	X error (cm)	Y error (cm)	Z error (cm)	Total (cm)	Image (pix)
01	-0.323341	1.61107	0.196184	1.65486	0.260 (10)
02r	0.0944381	-1.23455	0.542942	1.35197	0.101 (24)
04	-1.01806	-0.737171	-1.33923	1.83668	0.508 (13)
04a	0.354106	-0.553044	-0.746431	0.994187	0.435 (64)
04b2	-1.06843	-2.02336	1.4203	2.6931	0.151 (11)
04r	2.29632	1.89269	-2.59271	3.94683	0.471 (14)
06a	-0.600748	1.87552	-1.1187	2.26494	0.092 (71)
06z	0.211452	0.424076	2.22571	2.2756	0.125 (25)
10	0.0542551	-1.25521	1.41197	1.89001	0.249 (14)
Total	0.948595	1.41099	1.47657	2.25189	0.296

Table 6. Control points.
X - Easting, Y - Northing, Z - Altitude.

Label	X error (cm)	Y error (cm)	Z error (cm)	Total (cm)	Image (pix)
04	0.492041	-0.106357	-1.36245	1.45247	0.026 (2)
07	-0.376124	0.184291	0.755608	0.86393	0.257 (16)
51	1.39937	1.38807	2.98129	3.57394	0.257 (17)
06	-1.5153	-1.466	-2.37442	3.1754	0.263 (12)
Total	1.0768	1.01503	2.05871	2.53537	0.253

Table 3. Control points.
X - Easting, Y - Northing, Z - Altitude.

Label	X error (cm)	Y error (cm)	Z error (cm)	Total (cm)	Image (pix)
01	-0.36012	0.817342	1.11019	1.42487	0.042 (3)
02	1.10935	0.535759	1.5138	1.95174	0.160 (6)
02r	0.0997377	-0.520118	-0.447691	0.693468	0.461 (11)
03	-0.547515	1.13792	1.08292	1.66353	0.312 (35)
03r	-0.96974	-1.88375	-0.41675	2.15931	0.481 (27)
04	-1.3304	0.089318	-1.02155	1.67974	0.608 (11)
04a	-0.289118	-0.144802	0.426856	0.535503	0.379 (10)
04b	-0.814942	-0.806624	-0.855479	1.4306	0.152 (10)
04r	4.08897	0.651869	-2.099	4.64224	0.311 (7)
04r2	-0.796385	-0.437421	-2.1674	2.35015	0.255 (31)
05	0.0143436	-0.140723	-0.0413182	0.147363	0.462 (16)
06	0.069343	0.752973	3.09918	3.19009	0.278 (19)
07	0.0851196	-0.215921	-0.052502	0.237958	0.364 (4)
10	-0.099464	0.356644	0.0938157	0.381955	0.476 (10)
Total	1.26785	0.761833	1.35621	2.00677	0.376

Table 3. Control points.
X - Easting, Y - Northing, Z - Altitude.

Label	X error (cm)	Y error (cm)	Z error (cm)	Total (cm)	Image (pix)
1	-1.16095	1.31935	2.03034	2.68529	0.128 (5)
2r	0.829685	1.16275	-3.87916	4.13379	0.287 (7)
3a	0.465433	-3.83657	0.699766	3.92754	0.252 (45)
3b	-1.90446	-0.640528	4.09834	4.56438	0.088 (59)
4	-2.11318	-1.12971	1.66749	2.9193	0.364 (13)
4r	4.55867	1.53774	-4.77104	6.77561	0.287 (7)
6	-2.25179	1.03509	2.34027	3.40864	0.225 (45)
7	1.89463	1.82523	-0.17586	2.63667	0.294 (32)
10	-0.31842	-1.27086	-2.01082	2.39998	0.236 (7)
Total	2.10524	1.76008	2.81959	3.93446	0.231

Table 5. Control points.
X - Easting, Y - Northing, Z - Altitude.

Label	X error (cm)	Y error (cm)	Z error (cm)	Total (cm)	Image (pix)
1	-1.14273	-0.21229	-0.236792	1.18616	0.691 (20)
2	0.385482	1.02241	0.0800112	1.09559	0.707 (22)
2r	1.03934	2.81634	1.94247	3.57564	0.879 (31)
4	0.826404	0.779279	-0.0906356	1.13949	0.608 (10)
5	2.13417	-5.5881	1.14531	6.09042	0.645 (8)
6	-0.966426	-1.43121	0.610243	1.8316	0.629 (43)
7	-0.620498	0.995983	-2.58808	2.84168	0.627 (19)
8	-0.966736	-0.351161	0.209766	1.04971	0.400 (7)
9	-1.8091	0.894922	-0.325873	2.04449	0.649 (11)
10	4.51025	-0.212681	-0.417344	4.53451	0.407 (12)
11	0.10188	-1.70862	2.02184	2.64908	0.393 (6)
16	-0.287359	3.15647	2.08241	3.7924	0.445 (13)
17	-0.87523	-0.108063	1.48893	1.7305	0.544 (26)
15	-0.637423	-0.143356	-3.86132	3.9162	0.477 (19)
20	0.497294	-0.610081	1.86406	2.02341	0.573 (19)
Total	1.53087	1.96898	1.66486	2.9987	0.630

Table 4. Control points.
X - Easting, Y - Northing, Z - Altitude.

Label	X error (cm)	Y error (cm)	Z error (cm)	Total (cm)	Image (pix)
1	-0.95331	0.659583	-1.0853	1.588	0.370 (24)
2r	0.0164722	-0.454758	1.16266	1.24854	0.246 (11)
3	-0.620034	0.952437	1.52058	1.89835	0.323 (18)
4	0.0574136	-1.29623	-2.53349	2.84641	0.259 (28)
4r	3.53876	-2.29604	-2.74443	5.03255	0.248 (4)
6	-2.10277	5.35927	3.4206	6.69656	0.140 (16)
7	-1.31774	0.730844	-1.22539	1.9422	0.406 (18)
10	1.38008	-3.65227	1.4862	4.17761	0.253 (8)
Total	1.65387	2.52725	2.0677	3.66028	0.304

Table 5. Control points.
X - Easting, Y - Northing, Z - Altitude.

Figure B-1 – Reprojection error in meters in the three directions of all the GCPs.

Label	X error (cm)	Y error (cm)	Z error (cm)	Total (cm)	Image (pix)
02	-1.63416	-0.329571	-2.57244	3.06538	0.415 (10)
03	-0.943373	-3.81337	-1.03038	4.06121	0.559 (6)
04	0.390997	-0.591606	0.308179	0.773208	0.579 (6)
07	1.80102	1.06957	-0.604072	2.18004	0.569 (15)
10	-1.93085	0.426136	1.81005	2.68068	0.570 (14)
Total	1.46186	1.80698	1.51098	2.77224	0.543

Table 5. Control points.
X - Easting, Y - Northing, Z - Altitude.

Label	X error (cm)	Y error (cm)	Z error (cm)	Total (cm)	Image (pix)
04	0.45827	-0.116501	-1.28286	1.36723	0.026 (2)
07	0.510007	0.944314	2.64084	2.85059	0.257 (16)
06	-0.968289	-0.827812	-1.35795	1.86196	0.263 (12)
Total	0.685007	0.728142	1.8676	2.11834	0.251

Table 4. Control points.
X - Easting, Y - Northing, Z - Altitude.

Label	X error (cm)	Y error (cm)	Z error (cm)	Total (cm)	Image (pix)
01	-3.97132	-1.43887	1.48425	4.47713	0.678 (18)
09	-3.95189	0.261356	1.67754	4.30114	0.277 (2)
Total	3.96161	1.03408	1.58384	4.39002	0.649

Table 6. Check points.
X - Easting, Y - Northing, Z - Altitude.

Label	X error (cm)	Y error (cm)	Z error (cm)	Total (cm)	Image (pix)
51	2.23496	2.18245	4.6272	5.58293	0.257 (17)
Total	2.23496	2.18245	4.6272	5.58293	0.257

Table 5. Check points.
X - Easting, Y - Northing, Z - Altitude.

Label	X error (cm)	Y error (cm)	Z error (cm)	Total (cm)	Image (pix)
06	0.148049	1.49156	-0.501372	1.58052	0.209 (3)
05	0.421123	-2.77858	0.0546821	2.81085	0.189 (8)
08	-0.97879	0.401141	2.39313	2.61649	0.226 (8)
16	-0.397296	1.25505	-1.9599	2.36098	0.261 (6)
15	1.15634	-0.884603	-0.637601	1.58939	0.223 (8)
12	-0.162421	-0.576543	-0.441129	0.743893	0.470 (12)
14	-0.187003	1.09198	1.09219	1.55572	0.210 (5)
Total	0.622622	1.41364	1.28823	2.01136	0.300

Table 5. Control points.
X - Easting, Y - Northing, Z - Altitude.

Label	X error (cm)	Y error (cm)	Z error (cm)	Total (cm)	Image (pix)
01	0.0717436	0.301879	-0.249866	0.398386	0.034 (2)
02	0.99538	0.573776	1.34298	1.76737	0.193 (6)
03	-0.863823	-0.428276	1.09025	1.45542	0.380 (7)
04	-0.369888	-0.103826	-0.783659	0.872765	0.323 (7)
04a	0.349124	0.364834	-0.180011	0.536093	0.267 (10)
04b	0.236624	-0.595263	-1.24854	1.40328	0.145 (10)
04r2	-0.71628	-0.763038	-1.87975	2.15145	0.245 (31)
05	0	0	0	0	0.450 (14)
06	0.297105	0.649909	1.90861	2.038	0.123 (26)
10	0	0	0	0	0.465 (10)
Total	0.515572	0.458977	1.11518	1.31153	0.287

Table 4. Control points.
X - Easting, Y - Northing, Z - Altitude.

Label	X error (cm)	Y error (cm)	Z error (cm)	Total (cm)	Image (pix)
09	3.24603	-1.37812	-3.73366	5.13577	0.315 (12)
13	2.06341	2.18518	0.333954	3.02394	0.388 (8)
11	2.78493	1.86881	3.96684	5.19462	0.309 (9)
Total	2.74166	1.84089	3.15106	4.56451	0.335

Table 6. Check points.
X - Easting, Y - Northing, Z - Altitude.

Label	X error (cm)	Y error (cm)	Z error (cm)	Total (cm)	Image (pix)
02r	0.109237	-0.349071	-0.822065	0.899763	0.428 (15)
03r	-0.915368	-2.45174	0.0751753	2.61813	0.488 (17)
04r	2.52301	0.983158	-2.11492	3.43585	0.175 (4)
07	0.12698	-1.20557	0.45032	1.29317	0.359 (4)
Total	1.34457	1.46226	1.15727	2.29899	0.431

Table 5. Check points.
X - Easting, Y - Northing, Z - Altitude.

Label	X error (cm)	Y error (cm)	Z error (cm)	Total (cm)	Image (pix)
01	-0.225992	1.21437	-0.363816	1.28768	0.259 (10)
02r	0.550885	-0.939045	0.299612	1.12918	0.100 (24)
04a	0.313554	0.567184	-2.25782	2.34899	0.435 (64)
04b2	-0.827934	-1.71706	0.804345	2.069	0.133 (11)
06z	0.397641	0.545995	1.78738	1.91075	0.126 (25)
10	-0.208157	0.328565	-0.269674	0.473295	0.247 (14)
Total	0.472544	1.00271	1.24059	1.66366	0.312

Table 7. Control points.
X - Easting, Y - Northing, Z - Altitude.

Label	X error (cm)	Y error (cm)	Z error (cm)	Total (cm)	Image (pix)
04	-0.975773	0.17653	-3.30472	3.45028	0.516 (13)
04r	2.36916	2.83618	-4.6132	5.91087	0.461 (14)
06a	-1.25147	5.40401	-0.525505	5.57186	0.092 (71)
Total	1.64633	3.52507	3.29033	5.09537	0.268

Table 8. Check points.
X - Easting, Y - Northing, Z - Altitude.

Label	X error (cm)	Y error (cm)	Z error (cm)	Total (cm)	Image (pix)
1	-0.433524	1.04082	1.40773	1.80359	0.126 (5)
2r	0.474855	0.97161	-3.92209	4.06846	0.286 (7)
3a	0.39695	-3.62247	1.288	3.86507	0.251 (45)
4	-0.829806	-0.107724	2.12122	2.2803	0.374 (13)
7	1.32104	2.36267	0.365849	2.73152	0.294 (32)
10	-0.929506	-0.644895	-1.2607	1.69388	0.237 (7)
Total	0.802984	1.87791	2.05127	2.89466	0.279

Table 6. Control points.
X - Easting, Y - Northing, Z - Altitude.

Label	X error (cm)	Y error (cm)	Z error (cm)	Total (cm)	Image (pix)
3b	-1.99624	-0.430392	4.74261	5.16358	0.089 (59)
4r	4.87943	2.45542	-4.34543	6.98002	0.179 (7)
6	-2.43033	1.90206	3.23329	4.46973	0.225 (45)
Total	3.35163	1.81036	4.15649	5.63802	0.163

Table 7. Check points.
X - Easting, Y - Northing, Z - Altitude.

Label	X error (cm)	Y error (cm)	Z error (cm)	Total (cm)	Image (pix)
2	0.0844216	0.671578	0.0547288	0.679072	0.707 (22)
2r	0.500716	2.46082	2.03583	3.23279	0.879 (31)
5	1.89805	-5.73411	1.27561	6.17331	0.648 (8)
7	-0.934962	0.835924	-2.34427	2.65867	0.625 (19)
9	-2.08768	0.743251	-0.192657	2.2244	0.650 (11)
10	4.0237	-0.509817	-0.0184275	4.05591	0.414 (12)
16	-0.452745	2.8701	1.64944	3.34113	0.445 (13)
17	-0.978547	-0.401613	1.10945	1.53288	0.543 (26)
20	0.630051	-0.932918	1.62317	1.97534	0.573 (19)
Total	1.727	2.36095	1.41004	3.24728	0.654

Table 5. Control points.
X - Easting, Y - Northing, Z - Altitude.

Label	X error (cm)	Y error (cm)	Z error (cm)	Total (cm)	Image (pix)
1	-1.72897	-0.588366	-0.38003	1.86546	0.689 (20)
4	1.25525	1.02907	1.24274	2.04427	0.600 (10)
6	-1.27009	-1.66204	0.933256	2.29051	0.629 (43)
8	-1.42355	-0.520644	0.222795	1.53206	0.398 (7)
11	0.121594	-2.34604	3.71363	4.39429	0.361 (6)
15	-0.777399	-0.452553	-4.56096	4.64882	0.476 (19)
Total	1.21269	1.30047	2.49008	3.05979	0.588

Table 6. Check points.
X - Easting, Y - Northing, Z - Altitude.

Label	X error (cm)	Y error (cm)	Z error (cm)	Total (cm)	Image (pix)
1	-0.17892	-0.561907	-1.50921	1.62033	0.372 (24)
3	-0.211468	0.811967	3.09907	3.21064	0.319 (18)
4	1.22438	-0.0804221	-2.91953	3.1669	0.251 (28)
7	0.68142	2.14809	0.882939	2.42037	0.407 (18)
10	-1.51543	-2.31772	0.446796	2.80499	0.234 (8)
Total	0.93131	1.48105	2.06808	2.70884	0.328

Table 6. Control points.
X - Easting, Y - Northing, Z - Altitude.

Label	X error (cm)	Y error (cm)	Z error (cm)	Total (cm)	Image (pix)
2r	1.41001	-1.17029	1.80803	2.57424	0.246 (11)
4r	5.30882	-1.94095	-2.25707	6.08648	0.183 (6)
6	-3.67745	13.3321	5.68741	14.9538	0.297 (14)
Total	3.81643	7.80772	3.68375	9.43905	0.260

Table 7. Check points.
X - Easting, Y - Northing, Z - Altitude.

Figure B-2 - Reprojection error in meters in the three directions of all the GCPs and CPs.

APPENDIX C

```
clear all

P=readmatrix('d1');
v_m3=P(:,9);
l=P(:,8);

v_plus=0;
v_minus=0;
N=size(v_m3,1);
l_up=0;
l_down=0;

%separation of positive and negative values
for i=1:N
    if v_m3(i) > 0
        v_plus=v_plus+v_m3(i);
    else v_minus=v_minus+v_m3(i);
    end
end
```